Constitutive modeling and characterization of C/C-SiC CMC material

MSc Thesis
Material Science and Engineering
2022|23

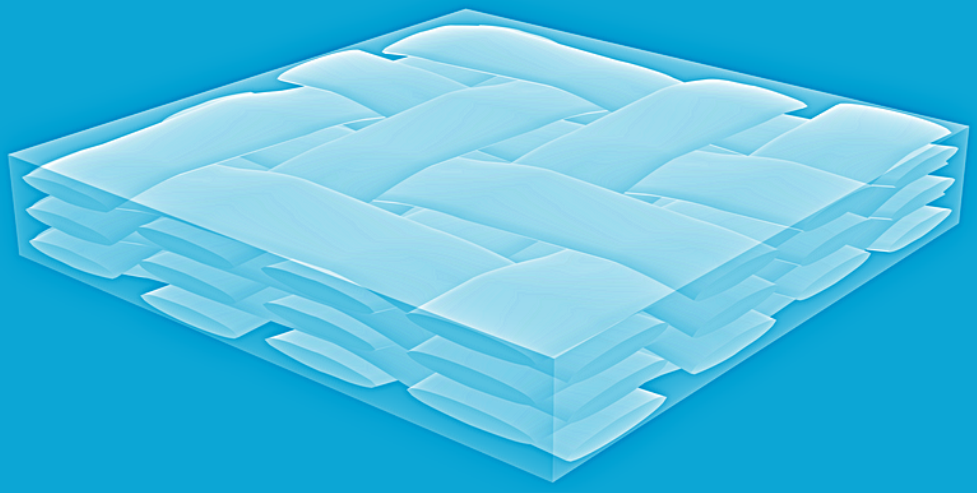

Efthymios Koutsounanos

TU Delft

Constitutive modeling and characterization of C/C-SiC CMC material.

by

Efthymios Koutsounanos

to obtain the degree of Master of Science
at Delft University of Technology,
to be defended publicly on Wednesday February 22, 2023 at 11:00 AM

Student number:	5384893	
Project duration:	March 6, 2022 – February 22, 2023	
Thesis committee:	Dr. M.H.F. Sluiter,	TU Delft
	Dr. S. (Sid) Kumar,	TU Delft, supervisor
	Rahul Sharma,	Arceon B.V., co-supervisor

An electronic version of this thesis is available at http://repository.tudelft.nl/.

Abstract

Ceramic matrix composites (CMCs) are advanced materials that consist of a ceramic matrix reinforced with a high-strength, high-stiffness material, such as carbon fibers. They offer excellent thermal and chemical stability while exhibiting low weight and exceptional mechanical properties. A novel CMC material is the C/C-SiC produced with 2/2 twill weave fabric. It consists of a carbon fiber-reinforced carbon (C) and silicon carbide (SiC) matrix. In this study, a macroscopic non-linear constitutive model accounting for the damage-induced plasticity is proposed for the 2/2 twill weave C/C-SiC composite.

In the context of this thesis, a computational model is developed, based on the framework of continuum damage mechanics and general plasticity theory. A potential function inspired by the Tsai-Wu criterion combined with a damage model is used to predict the strain and damage evolution. An exponential damage evolution law is introduced while the coupling of different damage modes is also considered. Moreover, an experimental investigation on the macroscopic mechanical behavior and damage mechanisms of C/C-SiC under in-plane on- and off-axis loading conditions is performed. Specimens with 0^o, 30^o and 45^o on- and off-axis angles were manufactured and tested under monotonic and cyclic tensile and compression loads. Furthermore, the microstructure of the pristine material and the fracture surfaces of the tested specimens are studied through scanning electron microscopy (SEM). A Bayesian optimization algorithm is finally used to optimize simultaneously the different material parameters based on the experimental test data.

The predicted stress-strain curves are in good agreement with the experimental curves, especially in the case of monotonic tensile loading. Both damage initiation and evolution are predicted accurately by the chosen laws and coupling functions. Moreover, the combination of the Tsai-Wu criterion with a damage evolution law is proven to predict the ultimate strength well. Fiber pull-out is observed in tension, while interlaminar and translaminar cracks in compression. This study thus provides an accurate constitutive model, a complete mechanical characterization of the in-plane behavior and a better understanding of the fracture mechanisms of C/C-SiC.

Acknowledgements

This thesis marks the end of a significant chapter in my life and the beginning of another one. The last ten months were challenging and full of new knowledge and unique experiences. There are certain people that were part of this journey and I would like to express my immense gratitude to them.

Firstly, I would like to thank my supervisor Dr. Sid Kumar for his support and guidance. His knowledge and feedback were crucial for the progress of this work. I am grateful for giving me the opportunity to be part of the mech-mat group among all these bright scientists and engineers.

Secondly, I would like to thank my co-supervisor from Arceon B.V., Rahul Sharma. I am deeply grateful to him and Rahul Shirke for giving me the opportunity to work as part of the company for one and a half years and for trusting me with the external research and graduation topic. Moreover, I would like to thank Bernhard Heidenreich for sharing his great knowledge of CMCs and lab experience with me. Finally, I would like to thank my colleagues at Arceon Yestin and Ebrar for making this journey more pleasant.

I would like to acknowledge the support of the technicians of the mechanical lab of 3mE, Sean, Kevork and Ton. Their support and assistance during the experiments were crucial.

Furthermore, would also like to extend my sincerest thanks to my friends in Greece and in the Netherlands who provided a listening ear both in person and remotely.

To my parents and family, I am forever thankful for your support, especially during these two and a half years. Last but not least, I want to thank Sofia for her support, encouragement and patience all this time.

Efthymios Koutsounanos
Delft, February 2023

Contents

List of Figures

List of Tables

Nomenclature

Abbreviations

C/C Carbon-carbon composite material

C/C-SiC Carbon-carbon silicon carbide

CFRP Carbon Fiber Reinforced Polymer

CLT Classical Laminate Theory

CMC Ceramic Matrix Composite

LSI Liquid Silicon Infiltration

WHIPOX™ Wound Highly Porous Oxide Ceramic

WIC Weak Interface Composite

WMC Weak Matrix Composite

Symbols

ϵ_{11} Strain in the longitudinal to the direction of the fibers (local coordinate system)

ϵ_{12} Strain in the transverse to the direction of the fibers (local coordinate system)

γ_{12} Strain in the 1-2 plane (local coordinate system)

$\mathbb{C}$ Stiffness matrix of the material

$\mathbb{Q}$ Reduced stiffness matrix of the material

$\mathbb{S}$ Compliance matrix of the material

ν_{12} Poisson ratio (local coordinate system)

$\boldsymbol{D}$ Damage tensor of the material

σ_{11} Stress in the 1-principal direction (longitudinal to the direction of the fibers) in the local coordinate system

σ_{12} Shear stress in the local coordinate system

σ_{22} Stress in the 2-principal direction (transverse to the direction of the fibers) in the local coordinate system

σ_{xx} Stress in the x-direction in the global coordinate system

σ_{xx}^{t} Ultimate stress in the x-direction in the global coordinate system

$\sigma_{xx}^{t,0}$ Proportionality limit in the x-direction in the global coordinate system

σ_{xy} Shear stress in the global coordinate system

σ_{yy} Stress in the y-direction in the global coordinate system

E_{11} Young modulus of composite in the longitudinal to the direction of fibers (local coordinate system)

E_{22} Young modulus of composite in the transverse to the direction of fibers (local coordinate system)

E_{xx} Young modulus of composite in the x-direction (global coordinate system)

E_{yy} Young modulus of composite in the y-direction (global coordinate system)

F_{1c} Compressive strength in the longitudinal to the direction of the fibers (warp direction)

F_{1c}^{o} Compressive strength in the longitudinal to the direction of the fibers (warp direction) for damage initiation

F_{1t} Tensile strength in the longitudinal to the direction of the fibers (warp direction)

F_{1t}^{o} Tensile strength in the longitudinal to the direction of the fibers (warp direction) for damage initiation

F_{2c} Compressive strength in the transverse to the direction of the fibers (weft direction)

F_{2c}^{o} Compressive strength in the transverse to the direction of the fibers (weft direction) for damage initiation

F_{2t} Tensile strength in the transverse to the direction of the fibers (weft direction)

F_{2t}^{o} Tensile strength in the transverse to the direction of the fibers (weft direction) for damage initiation

F_{6} Shear strength in the 1-2 plane

F_{6}^{o} Shear strength in the 1-2 plane for damage initiation

V_f Fiber volume fraction

1

Introduction

Ceramic matrix composites (CMCs) are a class of advanced materials that have gained significant attention in recent years due to their excellent mechanical and thermal properties. These materials consist of a ceramic matrix, typically made of silicon carbide or alumina, reinforced with a strong, stiff material such as carbon fibers or silicon carbide fibers. The combination of the ceramic matrix and the reinforcing material results in a material that is strong, stiff, and withstands high temperatures and harsh environments. CMCs are commonly used in the aerospace industry, where they are used to make lightweight structural components, engine parts, and other critical components. They offer higher stiffness and strength-to-weight ratios than metals, which means that they can support larger loads with less material. In addition to their mechanical properties, CMCs also have excellent thermal stability and corrosion resistance, which makes them well-suited for high-temperature applications. They can withstand temperatures up to 1500°C in a non-oxidizing environment, which is much higher than the melting point of most metals. They are also being explored for use in a wide range of other applications, including energy production, automotive, and biomedical devices.

One of the challenges in the design of CMC structures is the prediction of mechanical behavior under different loading conditions. To address this challenge, computational models that predict the behavior of these materials need to be developed. This study is focused on developing a computational model for predicting the mechanical behavior of the 2/2 twill weave Carbon fiber reinforced Carbon and Silicon Carbide (C/C-SiC) composite material. A computational model for this material with this particular reinforcement is not available in the literature. In order to construct such a model, experimental data for the material are needed therefore characterizing the material through testing is also achieved in the current study. A series of mechanical tests are performed and Scanning Electron Microscopy (SEM) images are obtained for this reason. The experimental data are used to obtain certain material parameters, directly or indirectly through optimization methods, such as Bayesian optimization.

The report is structured as follows, a review of the available literature is presented in Chapter 2. Details about the damage evolution and plasticity models used together with the numerical implementation are discussed in Chapter 3. The characterization of the material through mechanical tests and the SEM technique is presented in Chapter 4. Next, the identification of the material parameters with the use of optimization methods, the final results and the comparison with the experimental data are presented in Chapter 5. Finally, conclusions and future work recommendations are discussed in Chapter 6.

2

Literature review

The most important characteristics of C/C-SiC material manufactured via Liquid Silicon Infiltration (LSI) and the current literature on the computational approaches developed for CMCs, are presented in this chapter. An introduction to woven fabric and CMC materials is presented in Section 2.1 and 2.2. The manufacturing process, microstructure and mechanical behavior of C/C-SiC, is presented in Section 2.3. Failure theories of woven fabric composite materials are discussed in Section 2.4. Finally, the state of the art in the modeling of the mechanical behavior, damage evolution and failure of CMC materials is provided in Section 2.5.

2.1. Woven fabric composite materials

There are three fundamental types of textile weaves in textile technology, the plain weave, the twill weave and the satin weave. By interlacing warp (0^o) and weft (90^o) fibers, the corresponding weaving pattern is produced. Fibers are grouped in bundles and each fiber bundle contains a certain number of fibers. In this work, the studied CMC materials are produced with 3K 2/2 twill weave fabric. The 3K corresponds to the number of filaments in the fiber bundle, in this case, 3000 filaments, and the 2/2 to a weave type where warp fiber bundles are alternatively weaved over and under two weft fiber bundles repeatedly (Figure 2.1). Since the weaving pattern is symmetric, the warp and weft directions are interchangeable and thus when the fiber direction is mentioned later in this study, this can refer to either warp or weft without the loss of generality.

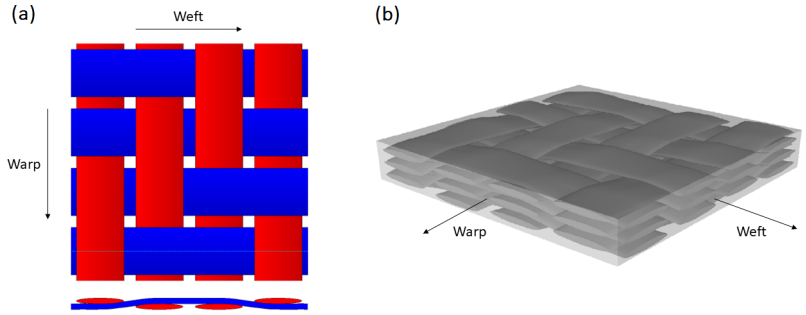

Figure 2.1: Schematic of the 2/2 twill weave fabric. (a) The 2D projection and a cross-section and (b) a stack of three layers of the fabric[1].

[1]TexGen was used to create these images

2.2. Ceramic matrix composite materials

2.2.1. Weak matrix and weak interface composites

There are two main categories of CMC materials, the Weak Matrix Composites (WMC) and the Weak Interface Composites (WIC)[2] [31]. Weak Interface composites exhibit weak fiber-matrix interface, allowing debonding between fibers and matrix. When a unidirectional (UD) WIC CMC material is loaded, matrix cracks start to develop and propagate in the matrix since fibers are the stiffer constituent and exhibit higher strain to failure. The matrix cracks propagate until they reach the fibers where they are being bridged between them. The fibers remain intact as the interfacial energy at the fiber/matrix interface is small enough to induce debonding and the cracks propagate in between the fibers. It is reported that the ratio between fracture energies of the interface and the fibers should be $\Gamma_I/\Gamma_f \leq 0.25$, for non-brittle failure to occur when the constituents have similar moduli [31]. Figure 2.2 presents the boundary curve that separates brittle from non-brittle failure, with respect to the relative fracture energy and relative Young modulus.

On the other hand, weak matrix composite materials are susceptible to multiple matrix cracks that propagate in the matrix and are deflected by the fibers. Even though the matrix fails early at low-stress values, the whole composite can be further loaded as long as the load is transferred to the fibers. The final failure of the material occurs when a large volume of fibers has failed. The mechanical behavior of the composite is mostly affected by the properties of the fibers and is strongly dependent on the fiber orientation. Overall, the fibers should remain intact and effectively carry the load when the material is loaded and cracks start to propagate, in order to achieve high damage tolerance. For this reason, the crack resistance of the matrix, the fiber-matrix interfacial energy and the strength of fibers should be chosen carefully when developing these materials. The behavior of the CMC is more complicated when the material is comprised of woven fabric plies, as in the case of the investigated material. The damage mechanisms are more complicated due to the complex reinforced geometry. Therefore, the investigated material lies between these two categories.

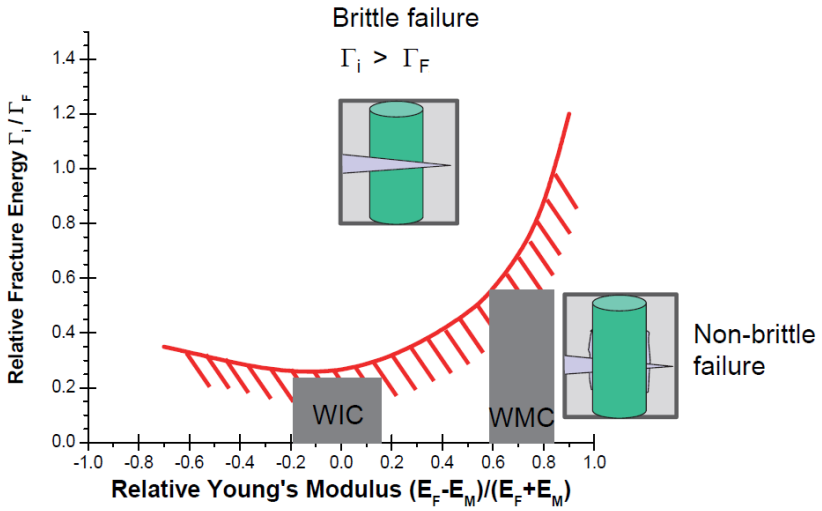

Figure 2.2: Boundary curve that separates brittle from non-brittle failure according to He and Hutchinson [24]

[2]This categorization was initially developed for unidirectional laminates.

2.2.2. Damage mechanisms in woven fabric composites

In contrast to UD composites, the different damage mechanisms in woven[3] or braided reinforced composites is difficult to be separated, if not impossible. Moreover, these mechanisms, *e.g.*, matrix cracking or microcracking, interface failure and crack propagation, can act and occur simultaneously and are called diffuse damage mechanisms. Damage accumulation occurs due to these mechanisms, and catastrophic failure occurs shortly after. This phenomenon characterizes the woven fabric composites [5]. Furthermore, the damage mechanisms that are quantifiable, *e.g.*, crack density, delamination lengths, are called discrete damage mechanisms.

Woven fabrics are preferred over unidirectional fabrics because they exhibit better out-of-plane and impact resistance properties compared to UD fabrics and offer the possibility of manufacturing complex surfaces with low manufacturing costs. Therefore, C/C-SiC manufactured with woven fabrics seems to have promising potential, especially due to the complex loading that the CMC structures are subjected to.

2.3. C/C-SiC

In this section, the most essential characteristics of C/C-SiC material are presented. It is important to examine how the manufacturing process affects the microstructure which is closely related to the mechanical properties. The investigated laminate comprises of several 3K $(0^o/90^o)$ 2/2 twill weave fabric plies stacked upon each other. For the manufacturing of the Carbon Fiber Reinforced Polymer (CFRP) plates, a phenolic resin is used as a precursor, that is rich in carbon ($\sim$ 60 % mass) and produces a structure that is stable, in terms of structural integrity and dimensions, even after the pyrolitic process [54]. The LSI method is preferred due to the low cost and short manufacturing time. LSI-manufactured C/C-SiC has improved oxidation resistance properties due to the formation of SiC/C zones. Moreover, it exhibits a low coefficient of thermal expansion, intermediate Young's modulus, high thermal conductivity and great thermal shock resistance [26]. The material lies somewhere between the WIC and WMC categories but is closer to the WIC side of the spectrum [31].

The mechanical properties of CMCs are strongly dependent on the microstructure, the bonding between fiber and matrix and the operating temperature. Specifically, the mechanical properties of C/C-SiC are higher at elevated temperatures and at a non-oxidizing atmosphere compared to the properties at room temperature. It is reported though that after 2000 ^oC in vacuum condition, there is a slight decrease in the tensile strength [17]. The maximum temperature range for C/C-SiC under stationary conditions is 1500-1700 ^oC [45]. Also, these CMCs can be used for temperatures up to 3000 ^oC when the life expectancy of the structure is restricted to a few minutes.

The restriction of this material to short-term applications is mostly due to the oxidation of carbon fibers, over 450 ^oC. The oxygen in the atmosphere penetrates the material from matrix cracks on the surfaces and also reacts with the open ends of fibers. These cracks are created during the manufacturing procedure but also during the application of tensile loads. The application of surface coating improves slightly the lifetime of the material, but still, their application is restricted to short-lifetime applications. Table 2.1 summarizes the most important mechanical properties of C/C-SiC developed via the LSI process and the corresponding values, based on the available literature [25] [45].

[3]Woven fabric composites are the plain weave, twill, harness satin, bi-axial weave composites, etc.

Property	Units	Values
Density	g/cm^3	$1.9 - 2.0$
Porosity	%	$2 - 5$
Tensile Strength	MPa	$80 - 190$
Failure Strain	%	$0.15 - 0.35$
Shear strength	MPa	$55 - 60$
Young's Modulus	GPa	$50 - 70$
Compression Strength	MPa	$210 - 320$
Flexural Strength	MPa	$160 - 300$
Fiber Content	%	$55 - 65$
Coefficient of Thermal Expansion (CTE) $\parallel$	10^{-6} K^{-1}	$-1.1 - 4.4$
Coefficient of Thermal Expansion (CTE) $\perp$	10^{-6} K^{-1}	$2.1 - 7.0$
Thermal Conductivity $\parallel$	W/mK	$17.0 - 22.6$
Thermal Conductivity $\perp$	W/mK	$7.5 - 10.3$
Specific Heat	J/kgK	$690 - 1550$

Table 2.1: Mechanical properties of C/C-SiC manufactured via-LSI process [25] [45].

2.3.1. Manufacturing process

There are different manufacturing techniques and sequences that can be followed to produce CMC materials. To manufacture the C/C-SiC material, a procedure that consists of three stages is followed, 1) manufacturing of a CFRP part with dimensions close to the desired dimensions, 2) conversion of the polymeric matrix of the CFRP part, into a porous C/C preform via pyrolysis ($\sim$ 1100 ^oC in a N_2 atmosphere) and finally 3) infiltration of Si into the porous preform via liquid silicon infiltration and conversion of the C/C preform into C/C-SiC. A schematic representation of the different stages is shown in Figure 2.3.

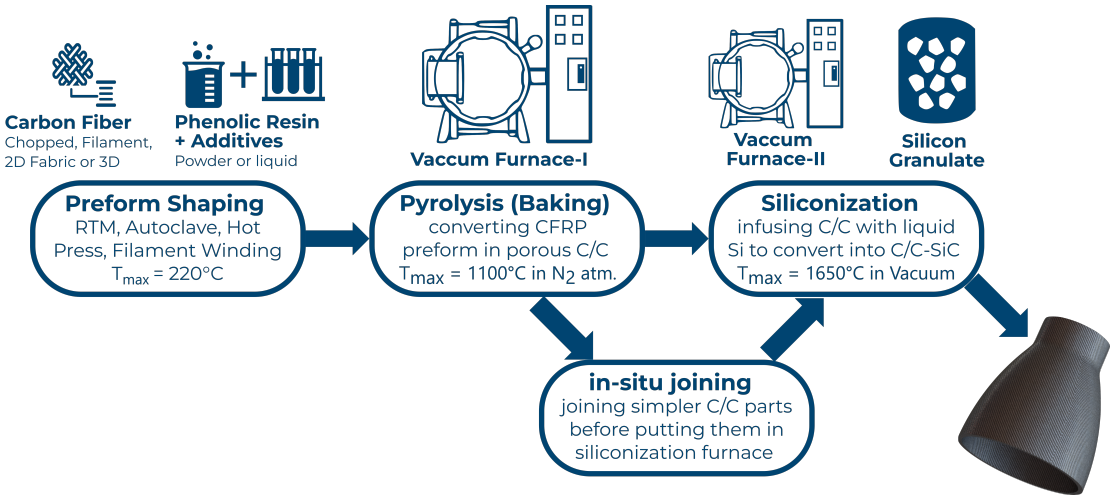

Figure 2.3: Manufacturing steps for the production of C/C-SiC.

Choosing a manufacturing technique for producing the CFRP part depends on the desired quality (open porosity) of the CFRP part, the type of reinforcement used, the shape of the final component, and time and cost. The open porosity, density and quality of the CFRP affect the final CMC material. Specifically, controlling the open porosity and density of the CFRP part, the microstructure and morphology of the CMC can be controlled as well. Different techniques are

available, *e.g.*, Resin Transfer Molding (RTM), autoclave, filament winding, and press-forming, therefore, choosing the right process at this stage is essential. Finally, once the CFRP part is manufactured, intermediate machining may take place if required.

During the pyrolysis step, the polymeric matrix of the CFRP part is converted into carbon and a porous C/C preform is created. The procedure is taking place in a N_2 atmosphere and at a temperature, of 1100 ^oC (mostly between 1100-1600 ^oC) [4]. The presence of fibers restricts the contraction of the part and therefore, tensile stresses are developed in the matrix. This leads to the formation of micro-cracks and a trans-laminar channel system of interconnected porosity [17]. The porosity after pyrolysis strongly depends on the fiber volume fraction [32]. If necessary, graphite molds may be used in this step, to restrict the shrinkage and support the CFRP part in sections where accuracy in dimensions is important. Moreover, various C/C preforms can be joined together after the pyrolysis stage and before siliconization.

Next, the C/C porous preform is subjected to LSI. During this stage, the preform is fed with silicon granules and placed in the siliconization furnace. By increasing the temperature inside the furnace to $\sim 1650\ ^oC$ and under pressure, the silicon melts. The molten Si is diffused into the C/C preform's channels via capillary forces. Silicon reacts with the carbon matrix and fibers, but only locally at the channel's walls. Therefore, the resulting microstructure consists of C/C segments which are separated by SiC and Si matrix. The reaction of Si with C is described by [17].

$$Si_{\text{liquid}} + C_{\text{solid}} \rightarrow SiC_{\text{solid}} \left[\Delta H = -68 \quad \text{kJmol}^{-1}\right] \tag{2.1}$$

It is apparent that the manufacturing process and microstructure are closely related and the latter affects highly the mechanical behaviour of C/C-SiC.

2.3.2. Microstructure

To understand the resulting microstructure of the final CMC material, it is important to examine the microstructure after every stage of the manufacturing process. Scanning electron microscopy (SEM) pictures after every stage are presented in Figure 2.4. In sub-figure (a) the microstructure of the CFRP part is presented, where the different stacked woven plies and fiber bundles can be seen. With a closer inspection, fine porosity and some microcracks inside the fiber bundles are also visible, as a result of the manufacturing step. In sub-figure (b) the microstructure after pyrolysis is presented. It consists of C fibers and C matrix, after the carbon yield of the precursor is approximately 60 *wt* $\%$. The resin is shrunk about 10 - 20 $\%$ in the thickness direction, though the shrinkage in the fiber direction is restricted by the stiffer fibers [50]. A large number of cracks are visible as a consequence of the shrinkage. Therefore, the crack formation is dependent on the type of fibers, weaving modes and fiber-matrix bonding forces. In sub-figure (c) the microstructure after the siliconization stage is presented. The dark regions correspond to C/C segments, surrounded by dark grey regions of SiC and some light grey areas that correspond to unreacted Si [45] [50]. Carbon in the amorphous state is surrounding the carbon fiber bundles (C_f/C). The dark black regions are residual pores and cracks that contribute to the measured open porosity [19]. It is also reported that there are two types of SiC in the microstructure, a fine-grained SiC and a coarse-grained SiC [50]. The fine-grained SiC can be found at the C/SiC interface, while the coarse-grained can be found further away from the interface. Sub-figure (d) provides a closer look at the microstructure after the LSI process.

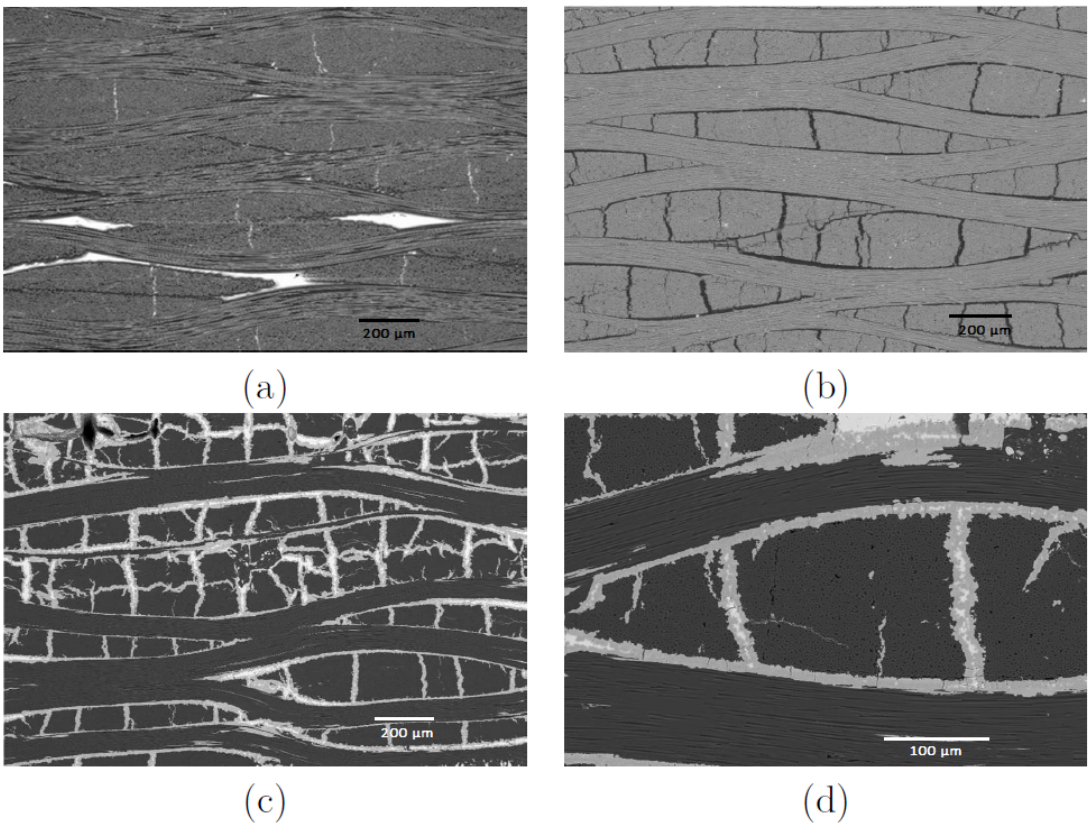

Figure 2.4: SEM images of the material during the manufacturing steps. (a) CFRP part with woven fabric, (b) C/C preform after the pyrolysis step, c) the final C/C-SiC part after the LSI step (x100 magnification) and (d) the C/C-SiC with x300 magnification. [17]

Each fiber bundle is divided by vertical cracks, called segmentation cracks, in sub-bundles or segments. These cracks are a result of the shrinkage that the body is subjected to during the manufacturing steps [22], especially during the pyrolysis step. These cavities of the crack pattern are later filled with liquid silicon that reacts with the carbon and produces SiC. It is found experimentally that each bundle is divided on average by five cracks per bundle [19]. All these characteristics of the microstructure directly affect the mechanical behavior of the material.

2.3.3. Mechanical behaviour

To study the mechanical behavior of the investigated material, uniaxial tensile tests at various orientations relative to the $(0^o/90^o)$ reinforcement need to be conducted. All the available literature regarding the mechanical tests of C/C-SiC is presented in this section. The material response to uniaxial tensile, 3-point bending and shear loads is presented in Figures 2.5 and 2.6. When the load is applied at an angle of 0^o relative to the fibers, the behavior is slightly non-linear and this non-linearity is more apparent as the angle between the load and fibers is increased. Moreover, the stiffness and ultimate strength are decreased as the loading angle increases. On the contrary, the strain (both elastic and plastic) is increased with increasing angle [65]. Furthermore, the ultimate tensile strength is almost 100 MPa less than the corresponding bending strength in every distinct angle. The overall stress-strain behavior is also dependent on the properties of the constituents and the type of reinforcement. Depending on the elastic and fracture properties of the constituents, it can be either linear or non-linear [33].

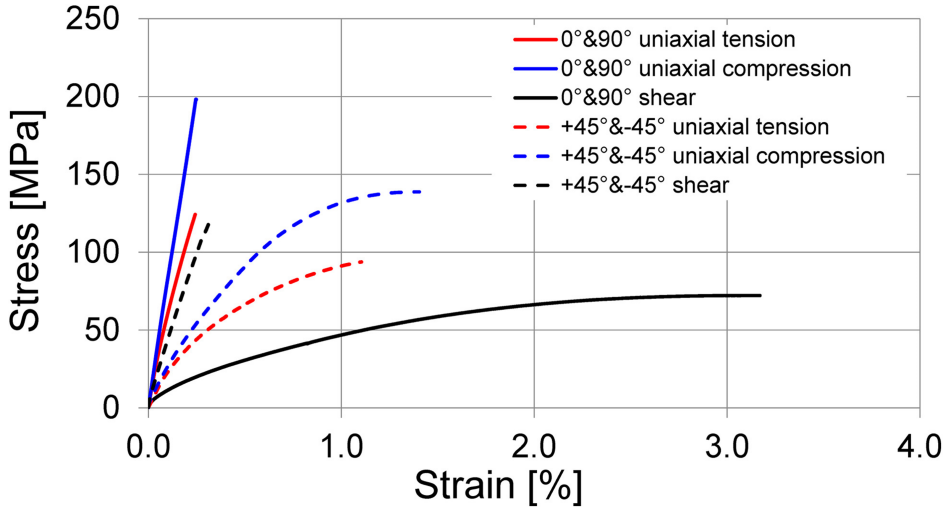

Figure 2.5: Stress-strain behavior of C/C-SiC 2/2 twill weave fabric ($0^o/90^o$) under uniaxial tensile, compression and pure shear loading with $V_f = 57$ [%], open porosity $= 2.0$ [%] and density $= 2.0$ [g/cm^3] [55].

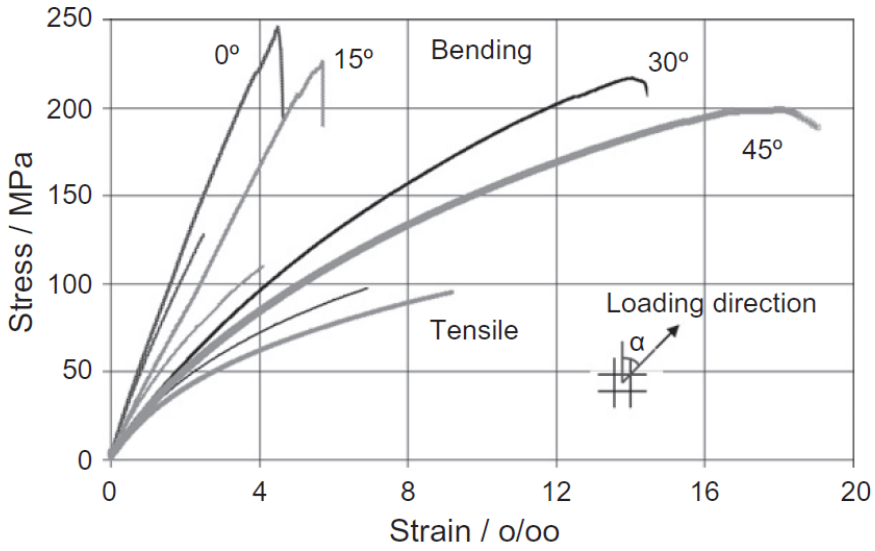

Figure 2.6: Stress-strain curves of C/C-SiC 2/2 twill weave fabric ($0^o/90^o$) from uniaxial tensile and 3-point bending tests with $V_f = 56.8$ [%], open porosity $= 0.92$ [%] and density $= 1.86$ [g/cm^3] [28] [27].

2.3.4. Damage and failure

The shape of the stress-strain curves can give an indication of the damage and failure mechanisms of the material. The steep load drop after the ultimate failure load is reached, indicates that the final failure of C/C-SiC is brittle [27] or quasi-brittle [19]. Fracture is produced by a combination of normal and shear stresses. Figure 2.7 (a) presents the microscopic damage state and the resulting macroscopic strain of SiC/SiC material [48] which present similar damage mechanisms to the investigated C/C-SiC material.

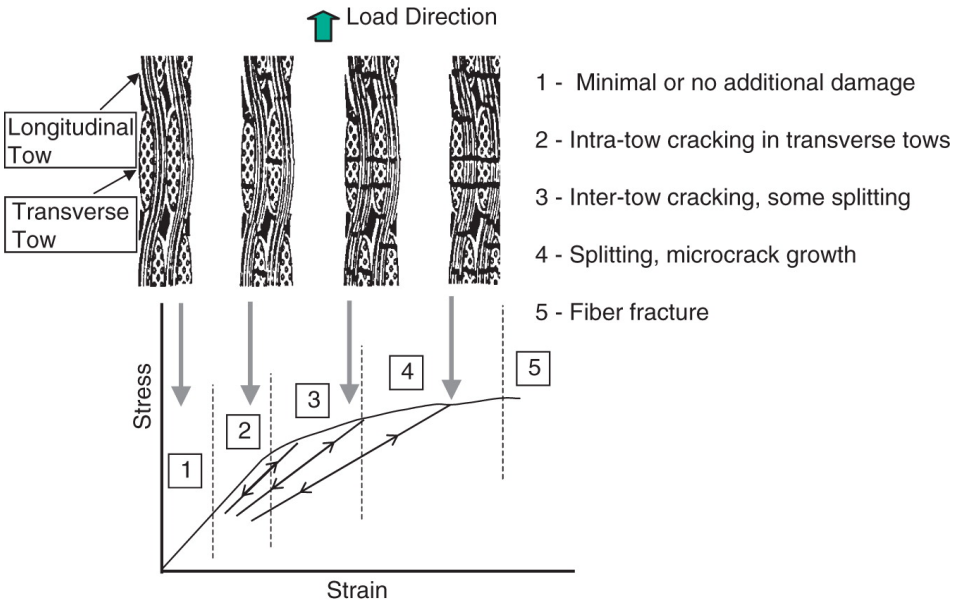

Figure 2.7: (a) Stress-strain curve of SiC/SiC CMC under uniaxial tension. [48].

At small stresses, the material response is linear followed by a gradually decreasing slope and material hardening. The size of each of these regions is varied with the material system. The presence of manufacturing defects (microcracks, porosity) affects the shape of the curve and in some cases, the curve is completely nonlinear. The initial slope and proportionality limit are affected by the existence of manufacturing defects.

The end of region 1 is described by the proportionality limit[4]. Recent reports suggest that, due to low fracture strain in the brittle CMC, matrix microcracking occurs below the proportional limit stress [36]. At small stresses, transverse microcracks start to appear, mostly within the transverse tows. These microcracks can be pre-existing defects like ”gaps” within fiber bundles due to insufficient matrix infiltration and these gaps open up at low loads. Residual stresses from the manufacturing stage affect the onset of microcracking.

As the load increases, the microcracks propagate (enlarge) and the formation of new microcracks continues. This is described as progressive matrix cracking and propagation. Splits start to form when the microcracks have propagated enough and reach other fiber bundles. With further increase of the load, these splits are enlarged and grow in the transverse direction (parallel to the loading direction). At this stage, fiber/matrix interface debonding takes place as well. Finally, in stage 4 the load is carried mostly by the longitudinal fiber bundles which eventually fracture, at stage 5, in a rapid manner and composite rupture occurs [48]. The loading and unloading cycles (hysteresis loops) can provide more information on the state of damage at different stress values.

All these damage mechanisms result in the gradual decrease of Young’s modulus. When the load is small enough and the material is still in the elastic regime, the Young modulus is constant. After the proportionality limit is reached and exceeded significant damage occurs and the degradation of the stiffness is increased until the point where catastrophic failure occurs. During the stiffness degradation, a permanent plastic strain is also observed, due

[4]proportionality limit is the stress value where a deviation from the initial linearity is apparent. It can be considered as the equivalent yielding point in metals.

to incomplete crack closure during unloading [54]. The fiber bundle was described by Hahn, Ansorge, and Bruckner-Foit [22] as the origin of final failure for C/C-SiC, therefore it can be assumed as a representative feature that triggers the ultimate composite failure [19]

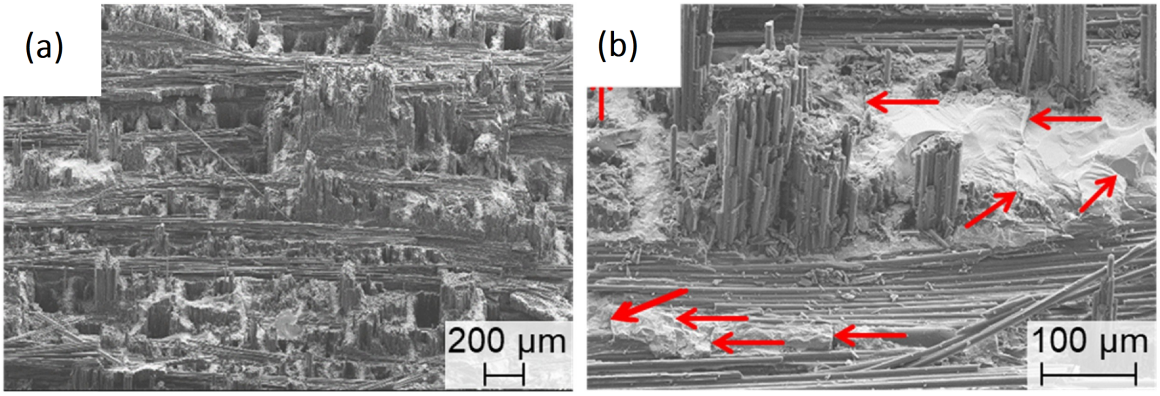

Figure 2.8: Fractured surfaces of 2/2 twill weave C/C-SiC material tested at room temperature with 0^o angle between loading and fiber direction [54]. The red arrows show the fiber bundles that have experienced pull-out and cracks in the matrix regions.

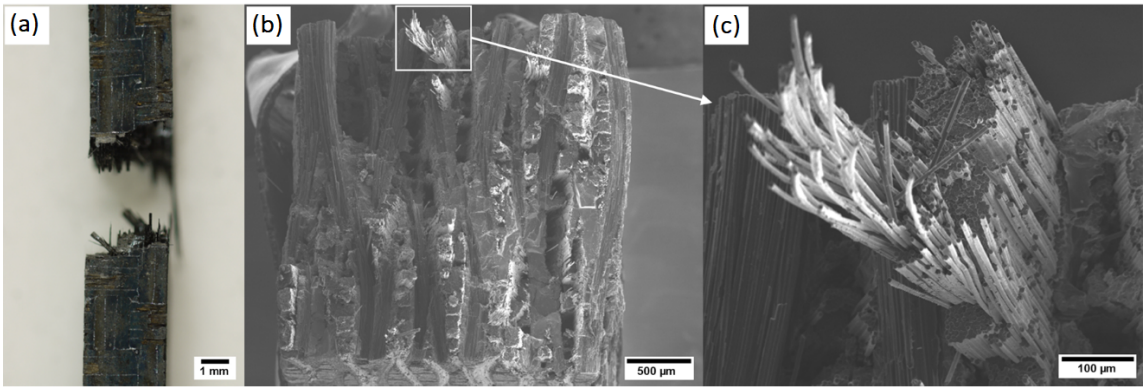

Figure 2.9: Fractured, plane weave ($0^o/90^o$) C/C-SiC, specimens after uniaxial tensile loads. a) The macroscopic failure of the specimen, b) the fractured surface obtained through SEM micrographs. The fractured surface can be seen as well as the fiber pull-out effect [19].

Figures 2.8 and 2.9 show the fracture surfaces of 2/2 twill and plain weave C/C-SiC loaded at 0^o relative to fibers. Both images show a significant amount of fiber bundle pull-out (C/C blocks embedded in SiC), together with cracks in the matrix areas (red arrows in Figure 2.8 (b) and (c)) [30].

Two-dimensional woven SiC-based CMCs were studied by Lamon [33] and it is reported that the damage of material initiates between the fiber bundles. As the loading continues the cracks propagate between the bundles and they are being deflected by them. It is again reported that the ultimate failure of CMC materials occurs when the load is completely carried by the fibers which happens after saturation of matrix cracking. The ultimate failure of the fibers, in SiC-based CMCs, takes place after $12 - 17\%$ of the fibers in a bundle have failed [7] [39]. Moreover, when the failed fiber bundles reach a critical number (≥ 1), the final failure occurs [33]. In general, the strength data of ceramic materials exhibit statistical distributions since they are highly affected by their microstructural defects and the random distribution of

these defects. Therefore, in many studies, statistical distribution theories, like the Weibull distribution, are used to describe the strength of CMCs [33] [40] [66]. The Weibull distribution function is also used widely to model various types of woven composites, to represent the randomness of breaking thresholds [46].

2.4. Failure theories

In order to predict the failure of composites different failure theories can be used based on the mechanical behavior of the material, type of reinforcement, available material data and fidelity regarding the mode of failure[5]. Macromechanical failure theories for composite materials were initially developed based on the well-established failure criteria for homogeneous isotropic materials. Composites exhibit anisotropy in stiffness and strength, therefore the existing and well-developed failure theories were extended to account for this behavior [47] [60] [9]. The variety of theories are based on certain assumptions, homogeneity and linear behavior until failure and most of them include terms that correspond to the strength properties in the principle directions. Some of these theories provide information about the mode of failure but others only indicate if or not failure occurred. The interaction between stress components is also neglected in others. Therefore, there are three main categories for the lamina failure theories:

1. *Limit or non-interactive theories:* where the ultimate stress or strain of each ply is directly compared to the corresponding stress or strain without the consideration of any interaction between stress components. The maximum stress and strain theory is an example of a non-interactive theory.

2. *Interactive theories:* in which an expression includes all the different stress components. The final failure is predicted but no information of the failure mode is given. The Tsai-Hill and Tsai-Wu theories are included in this category.

3. *Partially interactive or failure mode-based theories:* in which the failure mode (fiber, matrix) is predicted based on separate expressions. The Hashin-Rotem and Puck theories are considered failure mode-based theories.

Interactive theories present quasi-elliptical failure envelopes while the non-interactive ones, present rectangular/parallelogram-shaped envelopes [14]. The differences between failure theories are subtle in the first quadrant of the failure envelope, as the comparisons between theoretical and experimental results indicate [58]. The differences become significant when combined compression and shear loads are acting simultaneously. A difference of $100\% - 200\%$ is reported between various theories for the unidirectional lamina [57].

2.4.1. Tsai-Wu theory

A failure criterion that has been used to study orthotropic materials and CMCs specifically is the Tsai-Wu criterion [52] [30]. It is usually combined with a damage model and it is proven to be more accurate than other failure criteria, *e.g.*, Hashin criterion [2].

The anisotropic failure criterion developed by Gol'denblat and Kopnov [20] was later modified by Tsai and Wu [61] in the stress space. The criterion is given as

$$f_i\sigma_i + f_{ij}\sigma_i\sigma_j = 1 \tag{2.2}$$

[5]Fiber, inter-laminar tensile or compressive failure

which includes only the second- and fourth-order tensors and $i, j = 1, 2, ..., 6$. The expanded form of (2.2) is

$$\begin{aligned} &f_1\sigma_1 + f_2\sigma_2 + f_3\sigma_3 + f_4\sigma_4 + f_5\sigma_5 + f_6\sigma_6 + f_{11}\sigma_1^2 + f_{22}\sigma_2^2 + f_{33}\sigma_3^2 + f_{44}\sigma_4^2 \\ &+ f_{55}\sigma_5^2 + f_{66}\sigma_6^2 + 2f_{12}\sigma_1\sigma_2 + 2f_{13}\sigma_1\sigma_3 + 2f_{14}\sigma_1\sigma_4 + 2f_{15}\sigma_1\sigma_5 + 2f_{16}\sigma_1\sigma_6 \\ &+ 2f_{23}\sigma_2\sigma_3 + 2f_{24}\sigma_2\sigma_4 + 2f_{25}\sigma_2\sigma_5 + 2f_{26}\sigma_2\sigma_6 + 2f_{34}\sigma_3\sigma_5 + 2f_{35}\sigma_3\sigma_6 \\ &+ 2f_{36}\sigma_3\sigma_6 + 2f_{45}\sigma_4\sigma_5 + 2f_{46}\sigma_4\sigma_6 + 2f_{56}\sigma_5\sigma_6 = 1. \end{aligned} \tag{2.3}$$

An interaction between normal stresses is taken into account through the f_{12}, f_{23} and f_{13} coefficients. The criterion is simplified further for unidirectional composites where the shear strengths (F_4, F_5, F_6) are independent of the shear stress's sign and all the corresponding terms are zero. Also, by assuming transverse isotropy (UD material) in the 2-3 plane ($f_2 = f_3, f_{22} = f_{33}, f_{55} = f_{66}, f_{12} = f_{13}$) the criterion, for a three-dimensional stress state, is written as

$$\begin{aligned} &f_1\sigma_1 + f_2\left(\sigma_2 + \sigma_3\right) + f_{11}\sigma_1^2 + f_{22}\left(\sigma_2^2 + \sigma_3^2\right) + f_{44}\sigma_4^2 \\ &+ f_{66}\left(\sigma_5^2 + \sigma_6^2\right) + 2f_{12}\left(\sigma_1\sigma_2 + \sigma_1\sigma_3\right) + 2f_{23}\sigma_2\sigma_3 = 1 \end{aligned} \tag{2.4}$$

and for a two-dimensional stress state as

$$f_1\sigma_1 + f_2\sigma_2 + f_{11}\sigma_1^2 + f_{22}\sigma_2^2 + f_{66}\sigma_6^2 + 2f_{12}\sigma_1\sigma_2 = 1. \tag{2.5}$$

All the different coefficients in (2.4) and (2.5) are defined from uniaxial tests. By applying unidirectional tensile and compressive loads in the longitudinal and transverse direction and shear loads, the coefficients are defined by solving the system of equations and finally

$$\begin{aligned} f_1 &= \frac{1}{F_{1t}} - \frac{1}{F_{1c}}, \quad f_{11} = \frac{1}{F_{1t}F_{1c}} \\ f_2 &= \frac{1}{F_{2t}} - \frac{1}{F_{2c}}, \quad f_{22} = \frac{1}{F_{2t}F_{2c}} \\ f_3 &= \frac{1}{F_{3t}} - \frac{1}{F_{3c}}, \quad f_{33} = \frac{1}{F_{3t}F_{3c}} \\ f_{44} &= \frac{1}{F_4^2}, \quad f_{55} = \frac{1}{F_5^2}, \quad f_{66} = \frac{1}{F_6^2} \end{aligned} \tag{2.6}$$

The interaction coefficient f_{12} is calculated from

$$f_{12} = \frac{1}{2}\left[\frac{1}{\sigma_{bi}^2} - \frac{f_1 + f_2}{\sigma_{bi}} - (f_{11} + f_{22})\right] \tag{2.7}$$

where σ_{bi} is the failure load during the bi-axial tensile test. Due to the difficulty in performing bi-axial stress tests, the coefficient is approximated. An empirical estimation that is mostly used is

$$f_{12} \cong -\frac{1}{2}(f_{11}f_{22})^{1/2} \tag{2.8}$$

and the f_{23} coefficient (used in the three-dimensional case) is obtained as

$$f_{23} = f_{22} - \frac{f_{44}}{2}. \tag{2.9}$$

Certain reports suggest different values for the f_{12} coefficient [15] [16] [37] but the value is nearly constant under different stress states [11]. Usually, the interaction coefficient satisfies

$$-1 < f_{12} < 0 \tag{2.10}$$

In general, the Tsai-Wu criterion is selected in many cases due to its simplicity to implement in computational procedures, and as Tsai-Hill, it is expressed in a single equation but the coefficients account for the difference between tensile and compressive strength and the interaction coefficients are functions of them.

A safety factor S_f can be implemented in the Tsai-Wu theory. This safety factor is applied to every stress component and leads to a new critical state. For a two-dimensional stress state $(\sigma_1, \sigma_2, \tau_6)$ the new state becomes $(S_f\sigma_1, S_f\sigma_2, S_f\tau_6)$ and the Tsai-Wu criterion takes the form

$$f_1 S_f\sigma_1 + f_2 S_f\sigma_2 + f_{11} S_f^2\sigma_1^2 + f_{22} S_f^2\sigma_2^2 + f_{66} S_f^2\tau_6^2 + 2f_{12} S_f^2\sigma_1\sigma_2 = 1 \tag{2.11}$$

The Tsai-Wu criterion is reported to successfully predict the strength properties of filament wound C/C-SiC composites. A damage model can be used in combination with the Tsai-Wu criterion to predict the tensile strength and tensile strain of C/C-SiC in different directions [52] [30] (Figure 2.10). Overall, the criterion predicts strength values close to the experimental ones, especially when a damage-based Tsai-Wu criterion is used. A good agreement is achieved for most of the loading directions with a slight underestimation of the strength at 30^o and 45^o where shear damage is most significant [30].

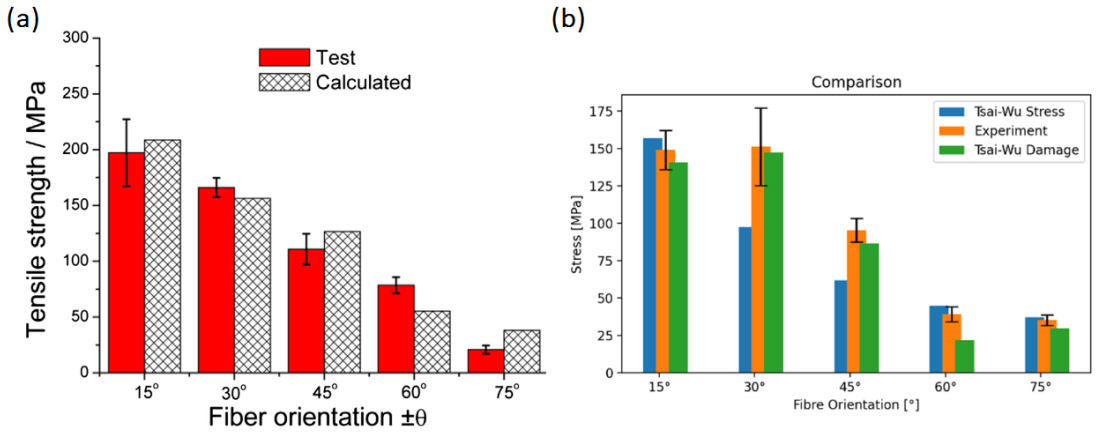

Figure 2.10: (a) The experimental strength of wound C/C-SiC in different loading directions and the calculated strength with the use of a damage model and Tsai-Wu criterion [52] and (b) a comparison of the experimentally determined material strength with the stress-based Tsai-Wu criterion and a damage-based Tsai-Wu criterion [30].

2.5. State of the art

Most of the developed modeling approaches, failure theories, micro- and macromechanical models to predict the mechanical behavior are developed based on unidirectional fabrics. In woven fabric composites, these theories and approaches need to be modified. On the other hand, approaches to model CMC materials are less developed and more complicated compared to those of FRP materials. Therefore, in this section, the most relevant approaches to model woven CMC materials are presented. These state-of-the-art approaches are mostly focused on studying the constitutive material behavior of CMCs under the scope of phenomenological modeling. This approach is the most appropriate in this type of material since more than one damage mechanisms act simultaneously after damage initiation.

2.5.1. Modeling of porous CMC materials

An attempt to model the elasto-plastic response and failure of CMC materials took place in recent years. A computational model to simulate the response of CMCs with porous matrices (p-CMCs) based on continuum damage mechanics is proposed by Tushtev, Horvath, Koch, and Grathwohl [62]. The construction of the model is based on results from uniaxial monotonic and cyclic tensile tests on a C/C CMC with a 2D woven fabric. The material is loaded in the axial (0^o) and diagonal direction (45^o) relative to the fibers. C/C is linear-elastic in the axial direction and non-linear in the diagonal direction where shear stresses are developed. The nonlinearity is caused due to matrix failure at low strains and the blocking of the matrix cracks from the fibers which causes inelastic strains.

With the assumption of plane stress conditions and small strains, the total strains are a summation of the elastic and plastic contribution $\boldsymbol{\epsilon} = \boldsymbol{\epsilon}^e + \boldsymbol{\epsilon}^p$. The decrease in the material's stiffness is accounted for by a damage vector $\boldsymbol{D}$ which is defined as

$$\boldsymbol{D} = \begin{bmatrix} D_{11} \\ D_{22} \\ D_{66} \end{bmatrix}; \quad D_{11} = 1 - \frac{E_{11}}{E_{11}^0}; \quad D_{22} = 1 - \frac{E_{22}}{E_{22}^0}; \quad D_{66} = 1 - \frac{G_{12}}{G_{12}^o} \tag{2.12}$$

where the superscript (^{o}) denotes the initial material parameters before damage occurs. The elastic strain energy is specified as

$$\Psi(\boldsymbol{\sigma}, \boldsymbol{D}) = \frac{1}{2}\left[\frac{\sigma_{11}^2}{E_{11}^o\left(1-D_{11}\right)} + \frac{\sigma_{22}^2}{E_{22}^o\left(1-D_{22}\right)} - \left(\frac{\nu_{12}^o}{E_{11}^o} + \frac{\nu_{21}^o}{E_{22}^o}\right)\sigma_{11}\sigma_{22} + \frac{\sigma_{12}^2}{G_{12}^o\left(1-D_{66}\right)}\right] \tag{2.13}$$

where ν_{12}^o and ν_{12}^o are the initial Poisson's ratio and the $\nu_{12}/E_{11} = \nu_{12}^o/E_{11}^o$ is assumed to remain constant. The partial derivation of the elastic strain energy with respect to stresses gives the elastic strains, $\epsilon_i = \partial\Psi/\partial\sigma_i$,

$$\begin{bmatrix} \epsilon_{11}^e \\ \epsilon_{22}^e \\ \gamma_{12}^e \end{bmatrix} = \begin{bmatrix} \frac{1}{E_{11}^o\left(1-D_{11}\right)} & -\frac{\nu_{21}^o}{E_{22}^o} & 0 \\ -\frac{\nu_{12}^o}{E_{11}^o} & \frac{1}{E_{22}^o\left(1-D_{22}\right)} & 0 \\ 0 & 0 & \frac{1}{G_{12}^o\left(1-D_{66}\right)} \end{bmatrix} \begin{bmatrix} \sigma_{11} \\ \sigma_{22} \\ \sigma_{12} \end{bmatrix}. \tag{2.14}$$

The thermodynamic forces which are related to the damage variables are defined as,

$$\boldsymbol{Y} = \frac{\partial\Psi}{\partial\boldsymbol{D}}; \quad Y_{11} = \frac{\sigma_{11}^2}{2E_{11}^0\left(1-D_{11}\right)^2}; \quad Y_{22} = \frac{\sigma_{22}^2}{2E_{22}^0\left(1-D_{22}\right)^2} \quad Y_{66} = \frac{\sigma_{12}^2}{2G_{12}^0\left(1-D_{66}\right)^2} \tag{2.15}$$

respectively. Since the material stiffness changes as the applied load increases above the damage initiation load, the damaged stiffness should be calculated. Using the continuum damage mechanics theory, the effective stress, $\boldsymbol{\sigma}_e$, is expressed as a function of the nominal stress as

$$\boldsymbol{\sigma} = \left(\mathbb{I} - \boldsymbol{D}\right)\boldsymbol{\sigma}_e \tag{2.16}$$

where $\mathbb{I}$ is the second order identity tensor. Therefore, the stress and plastic strain components are defined as

$$\sigma_{e11} = \frac{\sigma_{11}}{1-D_{11}}; \quad \sigma_{e22} = \frac{\sigma_{22}}{1-D_{22}}; \quad \sigma_{e12} = \frac{\sigma_{12}}{1-D_{66}}$$
$$\epsilon^p_{e11} = \epsilon^p_{11}\,(1-D_{11})\,; \quad \epsilon^p_{e22} = \epsilon^p_{22}\,(1-D_{22})\,; \quad \gamma^p_{e12} = \gamma^p_{12}\,(1-D_{66})\,. \tag{2.17}$$

The evolution of the damage parameters is governed by a damage potential f^d which is given by

$$f^d = \left(\frac{Y_{11}}{Y_t}\right)^2 + \left(\frac{Y_{22}}{Y_t}\right)^2 + \left(\frac{Y_{66}}{Y_s}\right)^2 - 1 = 0 \tag{2.18}$$

Y_t and Y_s are the threshold values of the tensile and shear mode for the initiation of damage, in the thermodynamic space. The damage variables are calculated once the thermodynamic forces exceed the corresponding threshold values and they are defined as

$$\dot{\boldsymbol{D}} = \dot{\lambda}^d \frac{\partial f^d}{\boldsymbol{Y}} \tag{2.19}$$

where λ^d is a scalar multiplier that is calculated from the consistency conditions. The growth of the damage surface in the thermodynamic space is given by a power-law that follows

$$Y_s(\delta) = Y^o_{12} + A\delta^n \tag{2.20}$$

where $\delta = \int \boldsymbol{Y} d\boldsymbol{D}$ is a scalar parameter and Y^o_{12} is the threshold value of Y_{12} for damage initiation and A and n are coefficients. For the calculation of the plastic strains, a plastic potential is required. The Hill criterion [10] is selected as plastic potential and is defined as

$$f^p(\boldsymbol{\sigma}) = \frac{1}{F^2_{1t}}\left(\sigma^2_{e11} + \sigma^2_{e22} - \sigma_{e11}\sigma_{e22}\right) + \frac{1}{F^2_{12}}{\sigma_{e12}}^2 - 1 = 0. \tag{2.21}$$

The plastic strain is calculated as

$$\dot{\boldsymbol{\epsilon}}_p = \dot{\lambda}\frac{\partial f^p}{\partial \boldsymbol{\sigma}_e} \tag{2.22}$$

where λ is the plastic scalar multiplier which is calculated from the consistency conditions. The yield function is constructed from the plastic function potential with the subtraction of the hardening law and is given as

$$f = f^p(\boldsymbol{\sigma}) - k(\chi) \tag{2.23}$$

where

$$k(\chi) = F^o_{12} + B\chi^m \tag{2.24}$$

is a power-law with χ being the inelastic work, F^o_{12} the shear strength for damage initiation and B and m coefficients. The A, B, n and m parameters are determined by fitting the unloading cycles in the diagonal tests.

The computational model is based on stress discretization and therefore the procedure begins with the initialization of the different parameters and the increase of stress components. Yielding is checked through (2.21). If no yielding occurs, the elastic strains are calculated from (2.14), all quantities are updated and catastrophic failure is checked again from (2.21) but this time the ultimate values for the strength are used. If yielding occurs though, the damage variables and plastic strain are calculated before the calculation of elastic strains. Moreover, if a catastrophic failure occurred the model stops otherwise the stresses are increased further and the above procedure is followed once again.

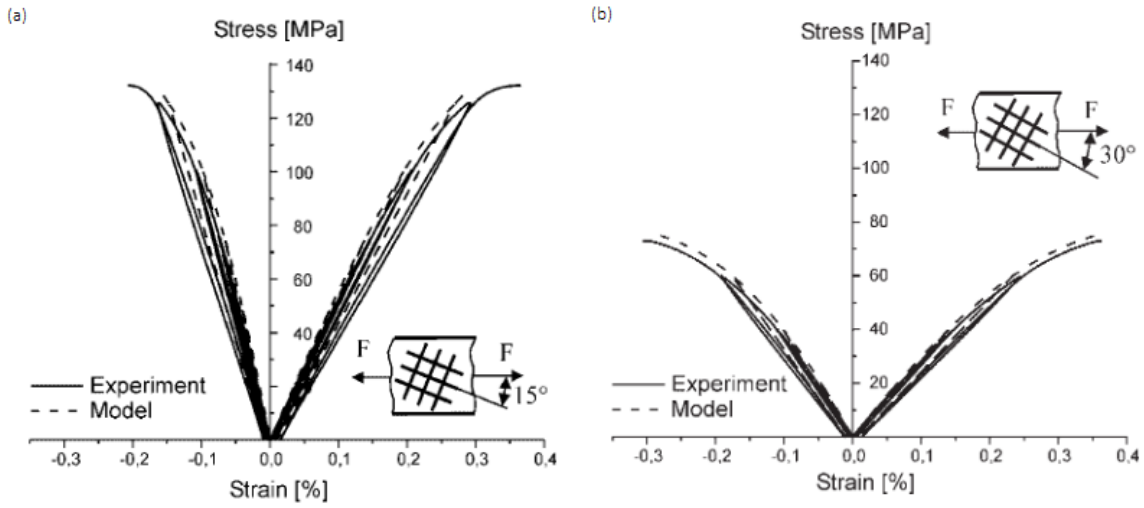

Figure 2.11: Experimental and theoretical stress-strain curves of C/C at (a) $\theta = 15^o$ and (b) $\theta = 30^o$ [62]

Tensile tests at $\theta = 15^o$ and 30^o prove that the experimental and theoretical results are close. Although this approach models the tensile behavior of CMC materials with porous matrices accurately, it has some drawbacks as well. Firstly, the model assumes that shear forces are the main driver for anisotropy in the material. The material is assumed linear elastic when the angle between the loading direction and fibers is 0^o. This might be true for C/C but not all CMCs follow the same behavior, *e.g.*, C/C-SiC behaves slightly non-linear when $\theta = 0^o$. Secondly, the compressive behavior of composite is not studied with the current approach. Thirdly, the model's dependence on experimental data should be mentioned and due to that, its application to other CMC systems is restricted.

2.5.2. Constitutive models for 3D C/C-SiC

A material that is similar to the woven C/C-SiC material, is the 3D needled C/C-SiC, which exhibits anisotropic elastoplastic and nonlinear behavior and similar mechanical properties. Xie et al. [65] studied the mechanical behavior of this material that is manufactured through a combination of Chemical Vapor Infiltration (CVI), Polymer Infiltration and Pyrolysis (PIP) and Liquid Silicon Infiltration (LSI) processes. The plastic deformation is studied through an innovative plastic potential and stiffness degradation through an exponential damage law. The 3D needled C/C-SiC presents randomly distributed defects, *e.g.*, porosity and microcracks [38] and their damage is characterized by matrix cracking, fiber pull-out and fiber rupture [65], same as the investigated woven C/C-SiC. A phenomenological material model and plasticity theory are used to describe the residual strains that result from the damage in the material.

Different tests were performed, *e.g.*, on- and off-axis uniaxial cyclic tensile tests in the 0^o, 15^o, 30^o and 45^o to the fibers direction and cyclic shear tests. For all these tests, the applied global stresses are rotated to the principal material axis by

$$\begin{aligned} \sigma_{11} &= \sigma_{xx} \cos^2 \theta \\ \sigma_{22} &= \sigma_{xx} \sin^2 \theta \\ \sigma_{12} &= -\sigma_{xx} \sin \theta \cos \theta. \end{aligned} \tag{2.25}$$

Plane stress conditions and small strains are assumed. The plastic yield function is expressed as

$$f(\boldsymbol{\sigma}) - k(\bar{\epsilon}^p) = 0. \tag{2.26}$$

It is expressed with respect to the plastic potential, $f(\boldsymbol{\sigma})$, and a hardening function, $k(\bar{\varepsilon}^p)$, which is a function of the effective plastic strain. A power law function [59] described as

$$\kappa(\bar{\epsilon}^p) = A(\bar{\epsilon}^p)^n \tag{2.27}$$

is assumed for the hardening law. The associate flow rule (2.22) is used in this case as well, to calculate the plastic strains. Under the plane stress condition, the proposed plastic potential function is

$$f(\sigma_{11}, \sigma_{22}, \sigma_{12}) = k\sqrt{\alpha_1\sigma_{11}^2 + \alpha_2\sigma_{22}^2 + \sigma_{12}^2} = \overline{\sigma} \tag{2.28}$$

with α_1, α_2 being the parameters that correspond to the anisotropy in the principal axes, k is a hardening rate parameter that corresponds to different hardening rates under different loading conditions and $\overline{\sigma}$ is the equivalent stress. By assuming that α_1, α_2 and k are constants the plastic strains are obtained from the associate flow rule (2.22) as

$$\begin{aligned} \dot{\epsilon}_{11}^p &= \frac{\partial f}{\partial \sigma_{11}}\dot{\lambda} = k^2\frac{\alpha_1\sigma_{11}}{\overline{\sigma}}\dot{\lambda} \\ \dot{\epsilon}_{22}^p &= \frac{\partial f}{\partial \sigma_{22}}\dot{\lambda} = k^2\frac{\alpha_2\sigma_{22}}{\overline{\sigma}}\dot{\lambda} \\ \dot{\gamma}_{12}^p &= \frac{\partial f}{\partial \sigma_{12}}\dot{\lambda} = k^2\frac{\sigma_{12}}{\overline{\sigma}}\dot{\lambda} \end{aligned} \tag{2.29}$$

and

$$\begin{aligned} \frac{\dot{\epsilon}_{11}^p}{\dot{\gamma}_{12}^p} = \frac{\alpha_1\sigma_{11}}{\sigma_{12}} \Leftrightarrow \alpha_1 = \frac{\dot{\epsilon}_{11}^p}{\dot{\gamma}_{12}^p}\frac{\sigma_{12}}{\sigma_{11}} \\ \frac{\dot{\epsilon}_{22}^p}{\dot{\gamma}_{12}^p} = \frac{\alpha_2\sigma_{22}}{\sigma_{12}} \Leftrightarrow \alpha_2 = \frac{\dot{\epsilon}_{22}^p}{\dot{\gamma}_{12}^p}\frac{\sigma_{12}}{\sigma_{22}}. \end{aligned} \tag{2.30}$$

In this work, it is assumed that the plastic strain increments do not change as given in (2.29), but the parameters α_1, α_2 and κ are corrected with the use of experimental data during the loading process. The plastic multiplier is taken as $\Delta\lambda = \dot{\bar{\epsilon}}^p$. Also, the equivalent stress from (2.28) is re-written as

$$\overline{\sigma} = h(\theta)\sigma_{xx} = \left(k\sqrt{\alpha_1\cos^4\theta + \alpha_2\sin^4\theta + \cos^2\theta\sin^2\theta}\right)\sigma_{xx}. \tag{2.31}$$

by using the rotation of stress equations. By equations (2.29), $h(\theta)$ and $\Delta\lambda = \dot{\bar{\epsilon}}^p$ the incremental plastic strain is given by

$$\dot{\epsilon}_{xx}^p = h(\theta)\dot{\bar{\epsilon}}^p \tag{2.32}$$

and the equivalent plastic strain for proportional loading is

$$\bar{\epsilon}^p = \frac{\epsilon_{xx}^p}{h(\theta)}. \tag{2.33}$$

For the case of the in-plane shear test, the hardening rate parameter is set to be $k = 1$ so the equivalent stress and strain becomes

$$\begin{aligned} \overline{\sigma} &= k_s \sigma_{12} = \sigma_{12} \\ \overline{\epsilon}^p &= \frac{\gamma_{12}^p}{k_s} = \gamma_{12}^p \end{aligned} \tag{2.34}$$

where k_s is the hardening parameter in the shear test. Therefore, equations (2.34) show that the relationship between equivalent stress and equivalent plastic strain can be determined through the shear tests. To obtain the parameters of the hardening law function (2.27), a master curve is determined for all the shear tests of 15^o, 30^o and 45^o. By fitting a power-law function to this master curve, the A and n parameters of (2.27) is determined. The rest of the anisotropic parameters, α_1 and α_2, are obtained from the following expressions [65]

$$\begin{aligned} \alpha_1 &= \psi(r_1, \overline{\sigma}) \\ \alpha_2 &= \psi(r_2, \overline{\sigma}) \end{aligned} \tag{2.35}$$

since the α_1 and α_2 parameters are assumed to change continuously as the load changes. The r_1 and r_2 are given by

$$\begin{aligned} r_1 &= \frac{\sigma_{11}}{\sqrt{\sigma_{11}^2 + \sigma_{11}^2}} + \frac{\sigma_{22}}{\sqrt{\sigma_{11}^2 + \sigma_{22}^2 + \sigma_{12}^2}} \\ r_2 &= \frac{\sigma_{22}}{\sqrt{\sigma_{11}^2 + \sigma_{11}^2}} + \frac{\sigma_{11}}{\sqrt{\sigma_{11}^2 + \sigma_{22}^2 + \sigma_{12}^2}} \end{aligned} \tag{2.36}$$

the stress components in (2.36) take positive values. The same expression of ψ can be used for the anisotropic parameters α_1, α_2 since the composite is symmetric in the 1- and 2-principal directions. A power law function is assumed for the ψ

$$\begin{aligned} \alpha_1 &= \psi(r_1, \overline{\sigma}) = A(r_1)(\overline{\sigma})^{B(r_1)} + C(r_1) \\ \alpha_2 &= \psi(r_2, \overline{\sigma}) = A(r_2)(\overline{\sigma})^{B(r_2)} + C(r_2) \end{aligned} \tag{2.37}$$

with $A(r_i), B(r_i)$ and $C(r_i)$ being parameters that need to be determined through fitting. To do that, the curves of α_1 and α_2 versus $\overline{\sigma}$ for the on- and off-axis cases need to be plotted. For that, the equations (2.36) and (2.34) are used. The A, B and C parameters are also expressed as a linear function of the stress ratio r_i [65]

$$\begin{aligned} A(r_i) &= A_0 + A_r r_i \\ B(r_i) &= B_0 + B_r r_i \quad i = 1, 2 \\ C(r_i) &= C_0 + C_r r_i \end{aligned} \tag{2.38}$$

So, by fitting the A, B, C vs r_i linear curves and the α_1 and α_2 versus $\overline{\sigma}$ curves, the A_0, B_0, C_0, A_r, B_r and C_r are obtained. On the other hand, the hardening rate parameter affects the behavior of the material, the higher the k value, the faster the hardening rate. An extra parameter r_{TS} is defined as

$$r_{TS} = \frac{\sigma_{11} + \sigma_{22} + \sigma_{12}}{\sqrt{\sigma_{11}^2 + \sigma_{22}^2 + \sigma_{12}^2}} \tag{2.39}$$

which is a tensile-shear combination parameter. The hardening rate parameter is expressed again as a linear function of r_{TS}

$$k(r_{TS}) = k_0 + k_r r_{TS}. \tag{2.40}$$

To determine the function's coefficients, a linear fitting of the k vs r_{TS} is performed.

Regarding the damage model, the damage variables are defined as in (2.12). The evolution of damage parameters is assumed to be similar to the evolution of plastic strains. Therefore, as (2.29) the damage evolution law is given by

$$\begin{aligned} D_{11} &= k^{*2}\frac{\alpha_1\sigma_{11}}{\overline{\sigma}^*}D(\overline{\sigma}^*) \\ D_{22} &= k^{*2}\frac{\alpha_2\sigma_{22}}{\overline{\sigma}^*}D(\overline{\sigma}^*) \\ D_{66} &= k^{*2}\frac{\sigma_{12}}{\overline{\sigma}^*}D(\overline{\sigma}^*) \end{aligned} \tag{2.41}$$

where

$$\overline{\sigma}^* = k^*\sqrt{\alpha_1\sigma_{11}^2 + \alpha_2\sigma_{22}^2 + \sigma_{12}^2} \tag{2.42}$$

is the damage equivalent stress, $D(\overline{\sigma}^*)$ corresponds to the damage state of the material and k^* is the damage rate parameter. Moreover, the damage rate parameter is expressed as the linear function of the tensile-shear combination parameter as

$$k^*(r_{TS}) = k_0^* + k^* r_{TS}. \tag{2.43}$$

Due to the random distribution of the defects in the CMC, a Weibull distribution is assumed for the ultimate strength of the material [65] [64]. Therefore, the failure probability is given as

$$F(\overline{\sigma^*}) = 1 - \exp\left[-\left(\frac{\overline{\sigma^*}}{\sigma_0}\right)^m\right] \tag{2.44}$$

where σ_0 is a scale parameter and m the Weibull modulus. The probability of failure is considered as the measurement of the damage state of the CMC when subjected to a load $\overline{\sigma^*}$. So, the damage state is expressed as

$$D(\overline{\sigma^*}) = 1 - \exp\left[-\left(\frac{\overline{\sigma^*}}{\sigma_w}\right)^{n_w}\right] \tag{2.45}$$

and the σ_w and n_w are determined through fitting of the $\overline{\sigma^*}$ vs $D(\overline{\sigma^*})$ curves. Once the damage variables are defined, the compliance matrix is determined from (2.14).

After the $\alpha_1, \alpha_2, A_r, A_0, B_r, B_0, C_r, C_0, \sigma_w, n_w, k_r, k_0, k_r^*$ and k_0^* are determined through the fitting of the corresponding curves, the mechanical response of the material is predicted through the proposed material model. The data from uniaxial on- and off-axis tensile tests are compared to the predicted curves in Figure 2.12. The theoretical curves are in good agreement with the experimental ones, especially the ϵ_{11} and ϵ_{xx} strains. For the ϵ_{22} and ϵ_{yy} the model underestimates the response of the material. The reason for this difference is the small values of strains in this direction that make it difficult to measure them accurately, as Xie et al. [65] reported.

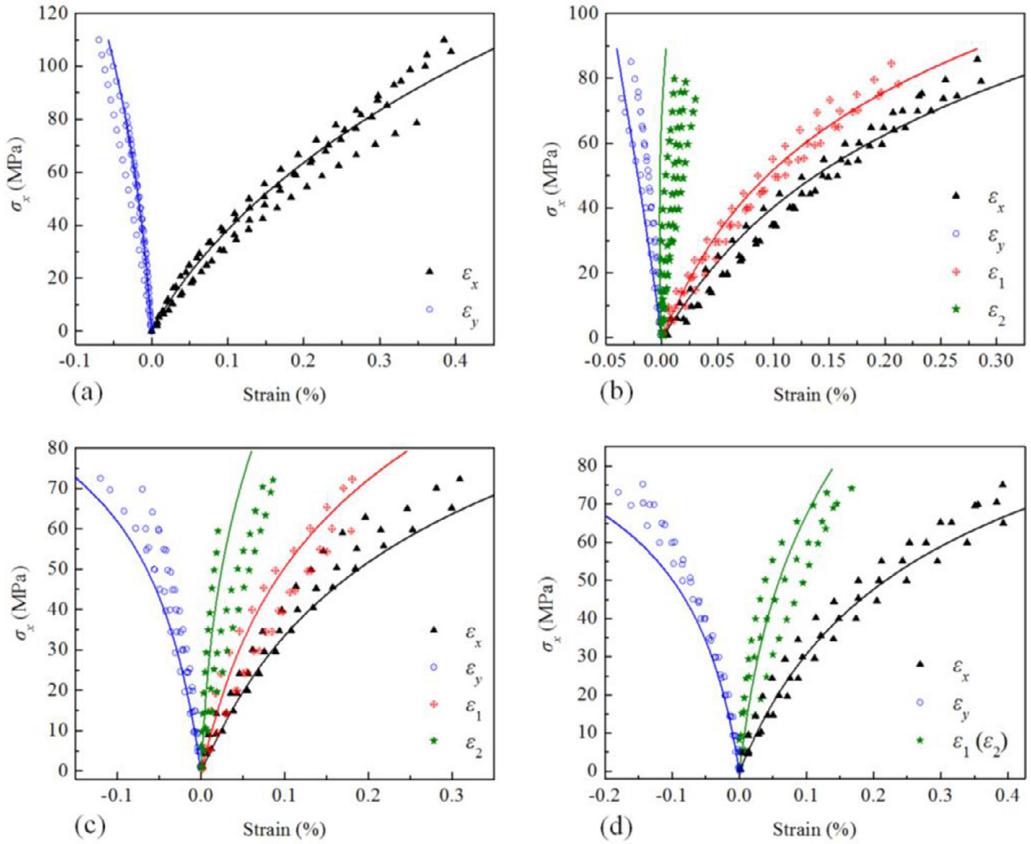

Figure 2.12: Experimental data and predicted curves for the (a) $\theta = 0^o$, (b) $\theta = 15^o$, (c) $\theta = 30^o$ and (d) $\theta = 45^o$ [65].

Overall, the material model is following the phenomenological approach to model the damage and the plasticity in the 3D C/C-SiC material. The proposed plastic potential function includes terms to model the anisotropy in the material, but it is symmetric to the stress axis. Therefore, the material response to compressive loads is assumed similar to the response to tensile loads. Moreover, the mechanical behavior of the material in compression is neglected in this case.

2.5.3. Phenomenological modeling of woven fabric composites

A phenomenological damage model for textile composites is presented by Böhm, Gude, and Hufenbach [5]. The research is based on hybrid glass-polypropylene woven thermoplastic composites. This research is worth mentioning since woven composites present often similar damage mechanisms to woven CMCs due to the same type of reinforcement. Moreover, the phenomenological approach and the structure of the model are relevant to the current work.

The most important features of the model are the damage definition and evolution equations and the criteria for the final failure of the composite. Damage is defined on the basis of continuum damage mechanics as a change in the elastic tensor. A novel failure criterion is used to describe the initiation of damage. The whole composite structure is decomposed into equivalent layers of bidirectional orthotropic layers, called idealized bidirectional layers. For the calculation of the stress-strain behavior of the laminate, the classical laminate theory is used. The plastic deformations are neglected and a non-linear elastic behavior is assumed for each layer. The degradation analysis, for the stiffness and strength, takes place in each individual layer.

Regarding the constitutive equations for each damaged layer, a fourth-order damage tensor $\boldsymbol{D}$ is defined. Effective stress is defined as in (2.16) and the stress-stain relationship for each damaged layer takes the form of

$$\begin{bmatrix} \sigma_{11} \\ \sigma_{22} \\ \sigma_{12} \end{bmatrix} = \begin{bmatrix} Q_{11} & Q_{12} & 0 \\ Q_{21} & Q_{22} & 0 \\ 0 & 0 & Q_{66} \end{bmatrix} \begin{bmatrix} \epsilon_{11} \\ \epsilon_{22} \\ \gamma_{12} \end{bmatrix} \tag{2.46}$$

where Q_{ij} is the reduced stiffness matrix components (see Appendix A). A damage tensor is chosen appropriately to reflect the degradation mechanisms. The model proposed by Audoin and BASTE [3] is used due to the fact that no further assumptions about the crack orientation and stiffness degradation coupling, are needed. Furthermore, it is valid for anisotropic materials and is equivalent even if the material (or layer) symmetry changes during damage. By this definition, the stiffness tensor is given by

$$\mathbb{Q} = \mathbb{Q}^0 - \mathbb{Q}^d \tag{2.47}$$

where $\mathbb{Q}^0$ is the undamaged stiffness tensor and $\mathbb{Q}^d$ is the tensor that corresponds to the loss of stiffness during damage and its components are unknown. The proposed damage tensor coefficients are

$$\begin{aligned} D_{ij} &= 1 - \frac{Q_{ij}}{Q^0_{ij}}, \quad i = 1,2,6; \quad i = j. \\ D_{ij} &= \frac{Q^0_{ij} - Q_{ij}}{Q^0_{ij} + \sqrt{Q^0_{ii}\left(1 - D_{ii}\right) Q^0_{ij}\left(1 - D_{jj}\right)}}, \quad i,j = 1,2; \quad i \neq j. \end{aligned} \tag{2.48}$$

By solving (2.48) for the equivalent stiffness tensor the following relations are obtained

$$Q_{11} = \left(1 - D_{11}\right) \frac{E_{11}}{1 - v_{12}v_{21}} \tag{2.49}$$

$$Q_{22} = \left(1 - D_{22}\right) \frac{E_{22}}{1 - v_{12}v_{21}} \tag{2.50}$$

$$Q_{66} = \left(1 - D_{66}\right) G_{12} \tag{2.51}$$

$$Q_{12} = Q_{21} = \left(1 - D_{12}\right) \frac{v_{21}E_{22}}{1 - v_{12}v_{21}} - D_{12}\sqrt{\left(1 - D_{11}\right)\left(1 - D_{22}\right) \frac{E_{11}E_{22}}{\left(1 - v_{12}v_{21}\right)^2}} \tag{2.52}$$

The E_{11}, E_{22}, G_{12} and ν_{12} and ν_{21} are the elastic properties of the bidirectional orthotropic layer. D_{11}, D_{22}, D_{66} and D_{12} denote the stiffness degradation in the principal, shear directions and Poisson's ratio, respectively.

The criterion used to predict the final failure of the material is based on the ideas of Böhler and Raclin [6] and Cuntze [12]. For a three-dimensional stress state, nine failure modes are defined while for plane stress conditions five of them remain. These are the tensile and compressive strength in the 1-direction and 2-direction and shear strength in the 1-2 plane. The criterion uses a series spring model and an interaction parameter m, that accounts for probabilistic and micromechanical effects, and is defined for every bidirectional orthotropic layer as

$$\left(\frac{\sigma_{11}}{F_{1t}}\right)^m + \left(\frac{-\sigma_{11}}{F_{1c}}\right)^m + \left(\frac{\sigma_{22}}{F_{2t}}\right)^m + \left(\frac{-\sigma_{22}}{F_{2c}}\right)^m + \left(\frac{\sigma_{12}}{F_6}\right)^m = 1. \tag{2.53}$$

The terms in (2.53) are called stress effort terms and correspond to the ultimate failure of the material. A similar criterion is used to predict the damage initiation[6]. The strength values at the onset of damage initiation are defined as $F^o_{1t}, F^o_{1c}, F^o_{2t}, F^o_{2c}$ and F^o_6 for tensile and compressive strength in the 1-direction and 2-direction and shear strength in the 1-2 plane, respectively. A similar interaction coefficient n is defined to account for all the aforementioned effects and the damage initiation criterion takes the form of

$$\left(\frac{\sigma_{11}}{F^o_{1t}}\right)^n + \left(\frac{-\sigma_{11}}{F^o_{1c}}\right)^n + \left(\frac{\sigma_{22}}{F^o_{2t}}\right)^n + \left(\frac{-\sigma_{22}}{F^o_{2c}}\right)^n + \left(\frac{\sigma_{12}}{F^o_6}\right)^n = 1 \tag{2.54}$$

the stress effort terms correspond in this case to the initiation of damage. After damage initiation, the shape of the damage surface changes as the load increases. The surface can be described by the function $H(\boldsymbol{\sigma}, \boldsymbol{D}, s)$. The s parameter indicates the size of the elastic domain and can be considered as the equivalent to the yield stress in the plasticity theory. The threshold value takes five different values for each damage mode. The damage surfaces are described by

$$\begin{aligned} H^t_1 &= \frac{\sigma_{11}\,(1-D_{11})}{F^o_{1t}} - s^t_{11} = 0, \quad H^c_1 = \frac{-\sigma_{11}\,(1-D_{11})}{F^o_{1c}} - s^c_{11} = 0 \\ H^t_2 &= \frac{\sigma_{22}\,(1-D_{22})}{F^o_{2t}} - s^t_{22} = 0, \quad H^c_2 = \frac{-\sigma_{22}\,(1-D_{22})}{F^o_{2c}} - s^c_{22} = 0, \\ H_{12} &= \frac{\sigma_{12}\,(1-D_{66})}{F^o_6} - s_{12} = 0 \end{aligned} \tag{2.55}$$

with $s^t_{11}, s^c_{11}, s^t_{22}, s^c_{22}$ and s_{12} being the threshold variables for the tensile and compressive loading in the 1- and 2-direction and the shear loading in the 1-2 plane, respectively. The damage surface with the n coefficient in the stress space is

$$H = \left[\left(\frac{\sigma_{11}}{F^o_{1t}}\right)^n + \left(\frac{-\sigma_{11}}{F^o_{1c}}\right)^n + \left(\frac{\sigma_{22}}{F^o_{2t}}\right)^n + \left(\frac{-\sigma_{22}}{F^o_{2c}}\right)^n + \left(\frac{\sigma_{12}}{F^o_6}\right)^n\right]^{\frac{1}{n}} = s. \tag{2.56}$$

The final part of this computational approach is the damage evolution law. For the damage parameters, (2.57) is fulfilled,

$$\boldsymbol{D} = \begin{bmatrix} D_{11} & D_{12} & D_{22} & D_{66} \end{bmatrix} = \begin{cases} 0 & \text{for } s < 1 \\ D & \text{for } s \geqslant 1 \end{cases} \tag{2.57}$$

The damage parameters are assumed to depend exclusively on the corresponding stress component. The damage parameters increase individually as well as simultaneously. Therefore, the evolution equations consist of five terms corresponding to a damage mode together with a rounding-off coefficient n.

$$D^n_{ij} = \sum_{k=1t}^{2t} (\phi_k q^{ij}_k)^n + \sum_{l=1c}^{2c} (\phi_l q^{ij}_l)^n + (\phi_{12} q^{ij}_{12})^n \quad i,j = 1,2,6 \tag{2.58}$$

where $\phi_{k,l}$ $(k,l = 1t, 1c, 2t, 2c, 12)$ is a scalar function that describes the individual damage variable D_{ij} in mode ij. The $q^{ij}_{k,l}$ with $(k,l = 1t, 1c, 2t, 2c, 12$ and $i,j = 1,2,12)$ describes the coupled damage growth of D_{ij}. Different damage evolution laws can be used to model nonlinear behavior, similar to the damage evolution of unidirectional plies. The damage evolution law that is used considers two model parameters β_k and α_k with

[6]The damage initiation and diffuse damage initiation terms are used to describe the same phenomenon.

$$\phi_k = \begin{cases} 0 & \text{for } H_k \leqslant 0 \\ \tanh\left[\beta_k \left(s_k - s_{k0}\right)^{\alpha_k}\right] & \text{for } H_k > 0 \end{cases}, \quad k = 1t, 1c, 2t, 2c, 12 \tag{2.59}$$

β_k is the driving damage growth parameter and α_k is a parameter that models the transition from the elastic to the damaged regime. The s_{k0} considers multi-axial stress states and describes the stress effort when $s = 1$ in mode j when it is reached for the first time. For example, for the uniaxial stress state $s_{k0} = 1$ and for the multi-axial $s_{k0} < 1$. Parameters q_{kl}^{ij} are assumed constant.

To determine the different parameters, uniaxial tests in tension and compression, ultrasonic wave speed measurements to determine the degradation of stiffness and SEM images to identify the damage progress, are used. Therefore, the strength values of damage initiation and ultimate failure are determined from tensile and compression tests. Eventually, $m = 3$ and $n = 2.5$ are chosen as the appropriate values for the interaction parameters. The damage evolution parameters (β_k, α_k, $q_{k,l}^{ij}$) are determined from the non-linear part of the uniaxial tensile curves and from ultrasonic degradation measurements [29].

Finally, the model is validated based on off-axis tensile tests at $\theta = 15^o$ and $\theta = 30^o$. The agreement between experimental and predicted results is good and the results are promising (Figure 2.14). Moreover, the damage initiation and ultimate failure of the composite are closely predicted by the proposed criteria. Therefore, the development of a phenomenological damage model to predict the anisotropy in the damage behavior of woven composites is proven to be reasonable. The degradation interactions and different failure modes are important in this case.

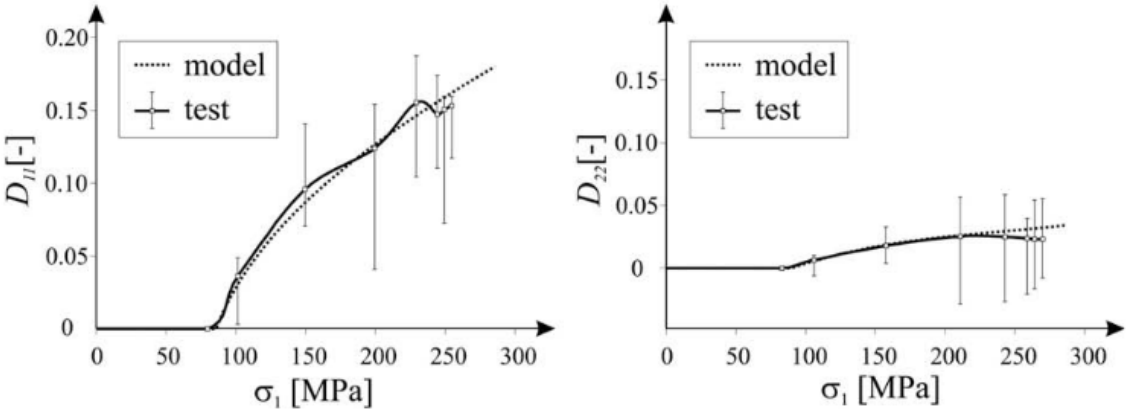

Figure 2.13: Evolution of damage parameters, measured by ultrasonic technique, and the resulted stiffness degradation [5].

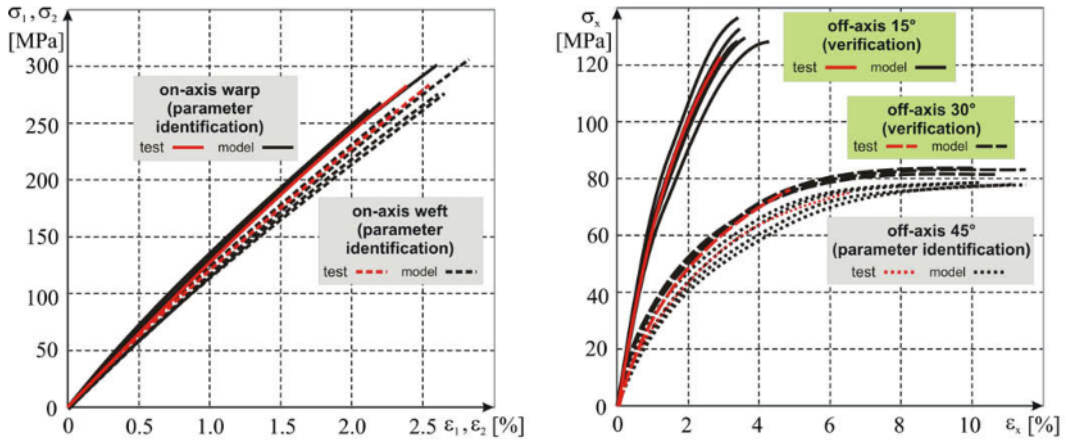

Figure 2.14: Comparison of the experimental and predicted on- and off-axis tensile curves of woven glass-fiber composite [5].

Attempts to model wound C/C-SiC and oxide CMCs are presented by Shi et al. [52] and Shi et al. [51]. The computational models are based on introducing an inelastic deformation factor in the equations of CLT to calculate the stiffness of the laminate. Moreover, a parameter that accounts for the manufacturing defects is introduced. The final failure is predicted via the Tsai-Wu criterion. These reports make an attempt to introduce manufacturing parameters, *e.g.*, V_f, fiber orientation and porosity in the model but they are restricted to simulating the behavior of wound C/C-SiC and ignore plasticity and damage evolution.

After the discussion on the current literature regarding the modeling of CMCs and woven composites, there are certain conclusions that are worth mentioning. Firstly, the mechanical behavior of the 2/2 twill weave C/C-SiC has not been extensively studied so far. There are only a few reports about the tensile and 3-point bending behavior of C/C-SiC and no data about the compressive behavior except for the case of $\theta = 0^o$. Secondly, there is a lack of accurate computational models to predict the elastoplastic behavior of woven C/C-SiC. Also, most of the computational models do not account for the compression, partially due to the lack of experimental data for C/C-SiC and CMCs in general.

2.6. Research objective

The scientific objective of the current work is to develop a constitutive model to predict the in-plane mechanical behavior of C/C-SiC. A phenomenological formulation of the damage-induced plasticity will be used since it results in a computationally efficient approach. Both tensile and compression in-plane material response will be included in this work. Mechanical and optical characterization of the material and its fractured surfaces is required since a sufficient number of experimental data is needed to optimize and evaluate the model. Further research questions are also defined to help achieve the main objective.

1. Can a Tsai-Wu-inspired potential function be used to accurately model the orthotropic nature of C/C-SiC?
2. How accurately can the failure of C/C-SiC in tension and compression be modeled by the Tsai-Wu failure criterion combined with a damage evolution law?
3. How does the damage in the CMC evolves during on- and off-axis loading?
4. Which are the failure mechanisms of C/C-SiC in tension and compression?

3

Constitutive model

3.1. Macromechanics of composite lamina

Composite materials fall under the category of anisotropic materials. Depending on the fiber orientation, layup and type of fiber reinforcement these materials can behave differently. Starting from the general case of an anisotropic material, the stress and strain states are represented by nine components, respectively. The generalized Hook's law is given as

$$\begin{aligned} \boldsymbol{\sigma} &= \mathbb{C}\,\boldsymbol{\epsilon} \\ \sigma_{ij} &= C_{ijkl}\epsilon_{kl} \end{aligned} \tag{3.1}$$

where C_{ijkl} are the stiffness components with $i, j, k, l = 1, 2, 3$. In this general case the stiffness matrix would comprise of 81 elastic constants but due to the symmetry in the stress and strain tensors ($\sigma_{ij} = \sigma_{ji}$ and $\epsilon_{ij} = \epsilon_{ji}$), the number of independent constants reduces to 36. Therefore, the stress-strain relation for an anisotropic material is written as

$$\begin{bmatrix} \sigma_{11} \\ \sigma_{22} \\ \sigma_{33} \\ \sigma_{23} \\ \sigma_{31} \\ \sigma_{12} \end{bmatrix} = \begin{bmatrix} C_{11} & C_{12} & C_{13} & C_{14} & C_{15} & C_{16} \\ C_{21} & C_{22} & C_{23} & C_{24} & C_{25} & C_{26} \\ C_{31} & C_{32} & C_{33} & C_{34} & C_{35} & C_{36} \\ C_{41} & C_{42} & C_{43} & C_{44} & C_{45} & C_{46} \\ C_{51} & C_{52} & C_{53} & C_{54} & C_{55} & C_{56} \\ C_{61} & C_{62} & C_{63} & C_{64} & C_{65} & C_{66} \end{bmatrix} \begin{bmatrix} \epsilon_{11} \\ \epsilon_{22} \\ \epsilon_{33} \\ \gamma_{23} \\ \gamma_{31} \\ \gamma_{12} \end{bmatrix}. \tag{3.2}$$

The stiffness components can be expressed in the form C_{ij} for simplicity. The independent components of the stiffness matrix are reduced to 21 due to the stiffness matrix being symmetric ($C_{ij} = C_{ji}$) [14]. Coming to the case of an orthotropic material, which has three mutually perpendicular planes of symmetry, the independent stiffness components reduce to nine. Moreover, when the reference system is taken along the principal material axis, the stress-strain relation becomes

$$\begin{bmatrix} \sigma_{11} \\ \sigma_{22} \\ \sigma_{33} \\ \sigma_{23} \\ \sigma_{31} \\ \sigma_{12} \end{bmatrix} = \begin{bmatrix} C_{11} & C_{12} & C_{13} & 0 & 0 & 0 \\ C_{21} & C_{22} & C_{23} & 0 & 0 & 0 \\ C_{31} & C_{32} & C_{33} & 0 & 0 & 0 \\ 0 & 0 & 0 & C_{44} & 0 & 0 \\ 0 & 0 & 0 & 0 & C_{55} & 0 \\ 0 & 0 & 0 & 0 & 0 & C_{66} \end{bmatrix} \begin{bmatrix} \epsilon_{11} \\ \epsilon_{22} \\ \epsilon_{33} \\ \gamma_{23} \\ \gamma_{31} \\ \gamma_{12} \end{bmatrix}. \tag{3.3}$$

When an orthotropic material is loaded under the plane stress condition, the out-of-plane stress components are zero and (3.3) becomes

$$\begin{bmatrix} \sigma_{11} \\ \sigma_{22} \\ 0 \\ 0 \\ 0 \\ \sigma_{12} \end{bmatrix} = \begin{bmatrix} C_{11} & C_{12} & C_{13} & 0 & 0 & 0 \\ C_{21} & C_{22} & C_{23} & 0 & 0 & 0 \\ C_{31} & C_{32} & C_{33} & 0 & 0 & 0 \\ 0 & 0 & 0 & C_{44} & 0 & 0 \\ 0 & 0 & 0 & 0 & C_{55} & 0 \\ 0 & 0 & 0 & 0 & 0 & C_{66} \end{bmatrix} \begin{bmatrix} \epsilon_{11} \\ \epsilon_{22} \\ \epsilon_{33} \\ \gamma_{23} \\ \gamma_{31} \\ \gamma_{12} \end{bmatrix} \tag{3.4}$$

and in the expanded form

$$\begin{aligned} \sigma_{11} &= C_{11}\epsilon_{11} + C_{12}\epsilon_{22} + C_{13}\epsilon_{33} \\ \sigma_{22} &= C_{12}\epsilon_{11} + C_{22}\epsilon_{22} + C_{23}\epsilon_{33} \\ 0 &= C_{13}\epsilon_{11} + C_{23}\epsilon_{22} + C_{33}\epsilon_{33} \\ \gamma_{23} &= \gamma_{31} = 0 \\ \sigma_{12} &= C_{66}\gamma_{12} \end{aligned} \tag{3.5}$$

by eliminating ϵ_{33}, the above equations become

$$\begin{aligned} \sigma_{11} &= \left(C_{11} - \frac{C_{13}C_{13}}{C_{33}}\right)\epsilon_{11} + \left(C_{12} - \frac{C_{13}C_{23}}{C_{33}}\right)\epsilon_{22} = Q_{11}\epsilon_{11} + Q_{12}\epsilon_{22} \\ \sigma_{22} &= \left(C_{12} - \frac{C_{23}C_{13}}{C_{33}}\right)\epsilon_{11} + \left(C_{22} - \frac{C_{23}C_{23}}{C_{33}}\right)\epsilon_{22} = Q_{12}\epsilon_{11} + Q_{22}\epsilon_{22} \\ \sigma_{12} &= C_{66}\gamma_{12} = Q_{66}\gamma_{12} \end{aligned} \tag{3.6}$$

The reduced stiffness matrix components are defined as

$$Q_{ij} = C_{ij} - \frac{C_{i3}C_{j3}}{C_{33}} \quad (i,j = 1,2,6) \tag{3.7}$$

so the stress-strain relationship becomes

$$\begin{bmatrix} \sigma_{11} \\ \sigma_{22} \\ \sigma_{12} \end{bmatrix} = \begin{bmatrix} Q_{11} & Q_{12} & 0 \\ Q_{21} & Q_{22} & 0 \\ 0 & 0 & Q_{66} \end{bmatrix} \begin{bmatrix} \epsilon_{11} \\ \epsilon_{22} \\ \epsilon_{12} \end{bmatrix} \tag{3.8}$$

or [14]

$$\begin{bmatrix} \sigma_{11} \\ \sigma_{22} \\ \sigma_{12} \end{bmatrix} = \begin{bmatrix} \frac{E_1}{1-\nu_{12}\nu_{21}} & \frac{\nu_{12}E_2}{1-\nu_{12}\nu_{21}} & 0 \\ \frac{\nu_{12}E_2}{1-\nu_{12}\nu_{21}} & \frac{E_2}{1-\nu_{12}\nu_{21}} & 0 \\ 0 & 0 & G_{12} \end{bmatrix} \begin{bmatrix} \epsilon_{11} \\ \epsilon_{22} \\ \epsilon_{12} \end{bmatrix}. \tag{3.9}$$

The studied material consists of layers of $(0^o/90^o)$[1] 2/2 twill weave fabric, so the lamina is orthotropic with three mutually perpendicular planes of symmetry.

Two coordinate systems are important in this work, the global coordinate system (x-y-z) of the whole laminate and the local coordinate system (1-2-3) of the plies. In composites, these are the two most used coordinate systems because each ply often has a different local coordinate system since the fibers are aligned differently.

[1] The two tows of the fabric are perpendicular to each other

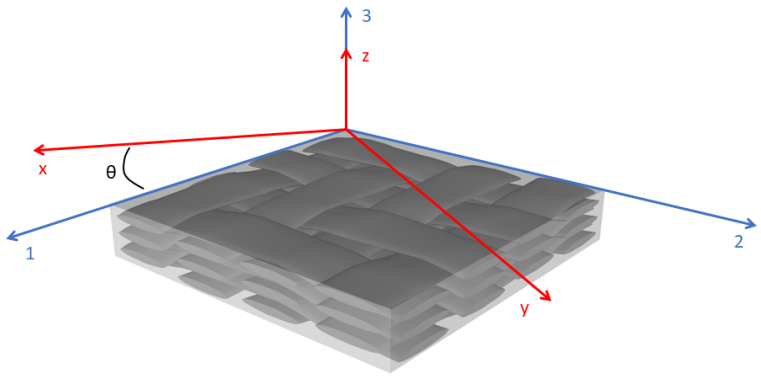

Figure 3.1: The two coordinate systems, global (red) and local (blue) coordinate system.

For a thin lamina, the transformation matrix takes the form

$$\boldsymbol{T} = \begin{bmatrix} c^2 & s^2 & 2cs \\ s^2 & c^2 & -2cs \\ -cs & cs & c^2 - s^2 \end{bmatrix} \tag{3.10}$$

where $c = \cos\theta$ and $s = \sin\theta$. Therefore,

$$\begin{bmatrix} \sigma_{11} \\ \sigma_{22} \\ \sigma_{12} \end{bmatrix} = \boldsymbol{T} \begin{bmatrix} \sigma_{xx} \\ \sigma_{yy} \\ \sigma_{xy} \end{bmatrix}$$
$$\begin{bmatrix} \epsilon_{11} \\ \epsilon_{22} \\ \gamma_{12} \end{bmatrix} = \boldsymbol{L} \cdot \boldsymbol{T} \cdot \boldsymbol{T}^T \begin{bmatrix} \epsilon_{xx} \\ \epsilon_{yy} \\ \gamma_{xy} \end{bmatrix} = \begin{bmatrix} c^2 & s^2 & cs \\ s^2 & c^2 & -cs \\ -2cs & 2cs & c^2 - s^2 \end{bmatrix} \begin{bmatrix} \epsilon_{xx} \\ \epsilon_{yy} \\ \gamma_{xy} \end{bmatrix} \tag{3.11}$$

where

$$\boldsymbol{L} = \begin{bmatrix} 1 & 0 & 0 \\ 0 & 1 & 0 \\ 0 & 0 & 2 \end{bmatrix}. \tag{3.12}$$

For the rotation of the engineering strains the $\boldsymbol{L}$ matrix is used since the rotation is applied to tensorial strain ($2\epsilon_{12} = \gamma_{12}$). Finally, to transform the stress-strain relation from the local system to the global system, (3.13) is followed

$$\begin{bmatrix} \sigma_{11} \\ \sigma_{22} \\ \sigma_{12} \end{bmatrix} = \mathbb{Q} \begin{bmatrix} \epsilon_{11} \\ \epsilon_{22} \\ \gamma_{12} \end{bmatrix} = \begin{bmatrix} \sigma_{xx} \\ \sigma_{yy} \\ \sigma_{xy} \end{bmatrix} = \boldsymbol{T}^T \cdot \mathbb{Q} \cdot \boldsymbol{L} \cdot \boldsymbol{T} \cdot \boldsymbol{L}^T \begin{bmatrix} \epsilon_{xx} \\ \epsilon_{yy} \\ \gamma_{xy} \end{bmatrix} = \bar{\mathbb{Q}} \begin{bmatrix} \epsilon_{xx} \\ \epsilon_{yy} \\ \gamma_{xy} \end{bmatrix} \tag{3.13}$$

where $\bar{\mathbb{Q}}$ is the reduced transformed stiffness matrix.

3.2. Constitutive model

The classical laminate theory and the reduced stiffness matrix that was mentioned in Section 3.1 refer to the linear regime of composites, which is the elastic regime of the laminate. Various composites and CMCs, present nonlinear stress-strain behavior, especially under off-axis loading directions. This nonlinearity is a result of damage-induced plastic strains that are developed as the stress is increased. To model this behavior, plasticity and a damage model based on continuum damage mechanics are used.

Continuum damage mechanics is a branch of mechanics based on the theory of elasticity that deals with the study of the progressive deterioration of materials under the action of external forces. The material is considered to be a continuous medium, and the damage is modeled as a field variable that evolves over time. In this theory, the material is considered to be an elastic solid, which means that it can recover its original shape after the external forces are removed. However, in the case of damage, the material is no longer able to recover its original shape, and the damage accumulates over time. This progressive deterioration of the material is modeled using the concept of a damage variable, which represents the amount of damage that has occurred in the material. Mathematical models are used to describe the evolution of the damage variable over time. These models are based on principles of mechanics and thermodynamics, and they take into account factors such as material properties, loading conditions, and the state of the damage. In this section, the damage evolution laws and the two-dimensional plasticity model are discussed.

3.2.1. Damage evolution

Damage has a significant contribution to the mechanical behavior of fiber-reinforced materials with non-ductile matrices. The irreversible formation and evolution of microcracks, cause primarily stiffness degradation and small permanent deformations. To study this phenomenon, a set of variables, denoted as damage variables, is introduced to characterize the state of anisotropic damage within the homogenized continua theory. These damage variables are treated as phenomenological internal variables since they have no direct relation to the micromechanics of crack and void formation and evolution. Due to the phenomenological introduction of damage, different states of damage are needed for each stress sign. The growth of defects under tension and under compression is different. Therefore, a set of defects has a different influence on the effective elastic properties of the material under different loading directions [41].

It is important to mention the constitutive assumptions that hold in the model:

1. Plane stress condition is assumed.
2. The effective elastic properties on the loading and unloading path, depending on the current state of damage variables.
3. The orthotropic nature of the composite does not change during the damaging process. This means that the defects are treated as disk-like cracks and they are oriented longitudinal and transverse to the fiber direction. So, the material symmetry remains the same for all damage states.
4. Is possible for the damage parameters to take different values for tension and compression.
5. The state of damage is unchanged in the elastic regime. The proportionality limit (damage threshold) determines the size of the elastic regime.
6. The evolution of damage is governed by $\boldsymbol{\sigma}$ and the damage variables. The damage variables increase monotonically with stress since no damage recovery is assumed.

In continuum damage mechanics, only the undamaged area of the cross-section carries the load. Therefore, the effective stresses $\boldsymbol{\sigma}_e$, are defined and refer to the net cross-section area of the damaged medium. The failure criteria hold in terms of the effective stresses $\boldsymbol{\sigma}_e$,

rather than the nominal stresses $\boldsymbol{\sigma}$. The nominal stress can be expressed as a function of the effective stress as

$$\boldsymbol{\sigma} = (\mathbb{I} - \boldsymbol{D})\, \boldsymbol{\sigma}_e \tag{3.14}$$

where $\boldsymbol{D}$ is the damage tensor and $\mathbb{I}$ is the identity tensor. Three non-negative damage parameters are defined for the two-dimensional plane stress condition, D_{11}, D_{22} and D_{66}[2]. These damage parameters are components of the damage tensor. Therefore, (3.14) can be expressed in the extended form as

$$\begin{bmatrix} \sigma_{11} \\ \sigma_{22} \\ \sigma_{33} \\ \sigma_{23} \\ \sigma_{31} \\ \sigma_{12} \end{bmatrix} = \begin{bmatrix} 1-D_{11} & 0 & 0 & 0 & 0 & 0 \\ 0 & 1-D_{22} & 0 & 0 & 0 & 0 \\ 0 & 0 & 1-D_{33} & 0 & 0 & 0 \\ 0 & 0 & 0 & 1-D_{44} & 0 & 0 \\ 0 & 0 & 0 & 0 & 1-D_{55} & 0 \\ 0 & 0 & 0 & 0 & 0 & 1-D_{66} \end{bmatrix} \begin{bmatrix} \sigma_{e11} \\ \sigma_{e22} \\ \sigma_{e33} \\ \sigma_{e23} \\ \sigma_{e31} \\ \sigma_{e12} \end{bmatrix} \tag{3.15}$$

or in the plane stress condition,

$$\begin{bmatrix} \sigma_{11} \\ \sigma_{22} \\ \sigma_{12} \end{bmatrix} = \begin{bmatrix} 1-D_{11} & 0 & 0 \\ 0 & 1-D_{22} & 0 \\ 0 & 0 & 1-D_{66} \end{bmatrix} \begin{bmatrix} \sigma_{e11} \\ \sigma_{e22} \\ \sigma_{e12} \end{bmatrix}. \tag{3.16}$$

The two damage parameters D_{11} and D_{22} take different values for tension and compression, D_{1t}, D_{1c} and D_{2t}, D_{2c}, while the shear damage parameter is independent of the sign of shear stress [41].

The constitutive relation is given by

$$\boldsymbol{\sigma} = \mathbb{Q}\, \boldsymbol{\epsilon}^e \tag{3.17}$$

where $\boldsymbol{\epsilon}^e$ is the elastic strain. Moreover, (3.17) can be expressed in terms of total strain and plastic strain as

$$\boldsymbol{\sigma} = \mathbb{Q}\, (\boldsymbol{\epsilon} - \boldsymbol{\epsilon}^p) \tag{3.18}$$

where $\boldsymbol{\epsilon}^p$ is the plastic strain. These relations can be modified to be expressed in terms of effective stresses. From the compliance relationship for plane stress orthotropic elasticity, the elastic strains are given by

$$\begin{bmatrix} \epsilon^e_{11} \\ \epsilon^e_{22} \\ \gamma^e_{12} \end{bmatrix} = \begin{bmatrix} \dfrac{1}{E_{11}(1-D_{11})} & -\dfrac{v_{21}}{E_{22}} & 0 \\ -\dfrac{v_{12}}{E_{11}} & \dfrac{1}{E_{22}(1-D_{22})} & 0 \\ 0 & 0 & \dfrac{1}{G_{12}(1-D_{66})} \end{bmatrix} \begin{bmatrix} \sigma_{11} \\ \sigma_{22} \\ \sigma_{12} \end{bmatrix} \tag{3.19}$$

and the inverse of the compliance matrix exists while $D_{11}, D_{22}, D_{66} < 1$, so the damaged stiffness matrix is given by

[2] Six non-negative damage parameters are defined for the three-dimensional case.

$$\mathbb{Q}^d = \frac{1}{t}\begin{bmatrix} E_{11}\left(1-D_{11}\right) & \nu_{21}E_{11}\left(1-D_{11}\right)\left(1-D_{22}\right) & 0 \\ \nu_{12}E_{22}\left(1-D_{11}\right)\left(1-D_{22}\right) & E_{22}\left(1-D_{22}\right) & 0 \\ 0 & 0 & tG_{12}\left(1-D_{66}\right) \end{bmatrix} \tag{3.20}$$

with $t = 1-\nu_{12}\nu_{21}(1-D_{11})(1-D_{22})$.

At this point, it is important to mention some remarks on the compliance and stiffness matrix of equations (3.19) and (3.20). Firstly, the term $1/E_{11}(1-D_{11})$ depends on the damage parameter in the 1-principal direction and is independent of the damage parameter in the 2-principal direction. The same holds for the $1/E_{22}(1-D_{22})$ parameter, which is independent of the D_{11} parameter. Secondly, the Poisson's ratio ν_{12} is not affected by the evolution of the damage parameters as it is reported by Nuismer [43], Carlsson et al. [8] and Matzenmiller et al. [41]. Moreover, the equality $\nu_{12}/E_{11} = \nu_{21}/E_{22}$ remains valid for both the pristine and damaged material. Thirdly, the elastic response of the material between shear stresses and strains is assumed linear as well.

Regarding the growth functions of the damage variables, they need to be carefully chosen in order to satisfy certain requirements. The growth functions should allow the damage variables to grow independently of each other or an appropriate coupling should exist between them. In continuum damage mechanics the evolution laws need to be consistent with the first and second thermodynamic laws [2]. The elastic strain energy, per volume due to damage evolution is given by

$$\Psi(\boldsymbol{\sigma},\boldsymbol{D}) = \frac{1}{2}\left[\frac{\sigma_{11}^2}{E_{11}\left(1-D_{11}\right)} + \frac{\sigma_{22}^2}{E_{22}\left(1-D_{22}\right)} - \left(\frac{\nu_{12}}{E_{11}} + \frac{\nu_{21}}{E_{22}}\right)\sigma_{11}\sigma_{22} + \frac{\sigma_{12}^2}{G_{12}\left(1-D_{66}\right)}\right]. \tag{3.21}$$

The thermodynamic forces are given by

$$\boldsymbol{Y} = \frac{\partial \Psi}{\partial \boldsymbol{D}} = \frac{1}{2}\,\boldsymbol{\sigma^T}\,\frac{\partial \mathbb{S}^d}{\partial \boldsymbol{D}}\,\boldsymbol{\sigma}; \quad Y_{11} = \frac{\sigma_{11}^2}{2E_{11}\left(1-D_{11}\right)^2}; \quad Y_{22} = \frac{\sigma_{22}^2}{2E_{22}\left(1-D_{22}\right)^2}$$
$$Y_{66} = \frac{\sigma_{12}^2}{2G_{12}\left(1-D_{66}\right)^2}. \tag{3.22}$$

The inelastic contributions to the strain energy are not taken into account, since no evolution of damage is assumed in the stress-free body. This phenomenon can be significant in the case of damage induced by environmental factors.

Some remarks on the energy release rates $\boldsymbol{Y}$, are that all components are positive and each stress component corresponds to one component of the thermodynamic forces. Since the thermodynamic forces are always positive, the damage model is thermodynamically admissible when (3.23) is fulfilled [2] [42]

$$\boldsymbol{Y}\boldsymbol{D} \geq 0. \tag{3.23}$$

Moreover, this condition is satisfied when the damage variables are positive and are always increasing. This remark gives room for a more simplified model for damage evolution.

To determine the evolution functions of the model, the reported damage mechanisms in CMCs are studied. As it is mentioned in Section 2.3.4, the random distribution of defects

in CMCs and ceramic materials and brittle nature results in a statistical distribution of the ultimate strength of the composite [13] [53]. The failure probability can be considered as the measurement of the damage state of the composite under stress [65]. In many studies, an exponential function, similar to the Weibull distribution function, is used to account for this phenomenon [33] [40] [66] [49] [48] as well as the randomness of breaking thresholds [46]. In this study, the proposed damage evolution function is given by [63]

$$D_i = A_i \left(1 - \exp\left[-\left(\frac{R_i^{m_i}}{m_i e}\right)\right]\right) \quad i = 1t, 1c, 2t, 2c \tag{3.24}$$

where A_i, m_i and e are constants that correspond to the maximum degradation value of the current damage mode, the material response and Napier's constant, respectively. The damage state functions R_i are given by

$$R_i = \begin{cases} \left(\frac{\sigma_{11}}{F_{1t}}\right)^2 & \text{for} \quad i = 1t \\ \left(\frac{\sigma_{22}}{F_{2t}}\right)^2 & \text{for} \quad i = 2t \\ \left(\frac{-\sigma_{11}}{F_{1c}}\right)^2 & \text{for} \quad i = 1c \\ \left(\frac{-\sigma_{22}}{F_{2c}}\right)^2 & \text{for} \quad i = 2c \end{cases} \tag{3.25}$$

Four independent damage variables and evolution functions are defined, one for each mode. Coupling between different modes is considered in order to calculate the directional damage variables. As it is reported by Li et al. [35], coupling between damage variables exists and it can be significant, therefore, it needs to be taken into account. For example, the damage in the 1-principal material direction is affected by the value of D_{1t} and D_{66} which are the damage variables of tension along the 1-direction and shear or the D_{1c} and D_{66} for compression. Based on that, the damage variables can be expressed as

$$\begin{aligned} D_{11} &= [1 - (1 - D_{1t})(1 - D_{1c})] + \alpha_{66} D_{66}^{\beta_{66}} \\ D_{22} &= [1 - (1 - D_{2t})(1 - D_{2c})] + \alpha_{66} D_{66}^{\beta_{66}} \\ D_{66} &= 1 - (1 - D_{1t})(1 - D_{2t})(1 - D_{1c})(1 - D_{2c}) \end{aligned} \tag{3.26}$$

where α_{66} and β_{66} are proportional constants. Experimentally, a quantitative analysis can be performed to analyze the damage characteristics of the material [34]. To measure the damage state, the degradation ratio of the damaged modulus to the initial, undamaged elastic modulus is given by

$$D = 1 - \frac{E^d}{E^o} \tag{3.27}$$

and it is measured from the loading and unloading cyclic stress-strain curve. Hysteresis effects are not considered in the current study. The most important characteristics of the cyclic stress-strain curves are presented in Figure 3.2.

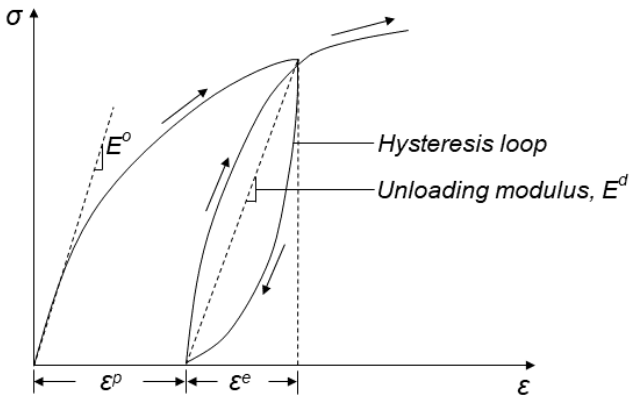

Figure 3.2: Main characteristics of the cyclic stress-strain curve.

3.2.2. Plasticity model

In the current section, the plasticity model used in the model is discussed. Plasticity is expressed through the yield function, which is a function of the plastic potential and the hardening law. Any stress or strain state lies within the linear regime or on the boundary of the yield surface. A yield function is a scalar function that describes the limit of elastic deformation for a material before it begins to yield (i.e., undergo plastic deformation). It is used to predict the onset of plastic deformation in a material under various loading conditions and is often used in conjunction with a potential function[3] to describe the behavior of the material during plastic deformation. It is defined in the stress or strain space. Below two potential functions are presented and compared.

First, a generalized quadratic potential function, g, can be used for orthotropic materials and is defined as [44]

$$\begin{aligned} 2g(\boldsymbol{\sigma}) = {} & \alpha_{11}\sigma_{e11}^2 + \alpha_{22}\sigma_{e22}^2 + \alpha_{33}\sigma_{e33}^2 + \\ & + 2\alpha_{12}\sigma_{e11}\sigma_{e22} + 2\alpha_{13}\sigma_{e11}\sigma_{e33} + 2\alpha_{23}\sigma_{22}\sigma_{33} + \\ & + 2\alpha_{44}\sigma_{23}^2 + 2\alpha_{55}\sigma_{13}^2 + 2\alpha_{66}\sigma_{12}^2 \end{aligned} \tag{3.28}$$

and for the two-dimensional case of plane stress, the equation is simplified to

$$2g(\boldsymbol{\sigma}) = \alpha_{11}\sigma_{e11}^2 + \alpha_{22}\sigma_{e22}^2 + 2\alpha_{12}\sigma_{e11}\sigma_{e22} + 2\alpha_{66}\sigma_{12}^2 \tag{3.29}$$

The yield function, f, can be defined as

$$f = g(\boldsymbol{\sigma}) - k(\bar{\epsilon}^p) \tag{3.30}$$

where $k(\bar{\epsilon}^p)$ is a function that describes the isotropic hardening with the property $k(\bar{\epsilon}^p = 0) = 1$ .The plastic strains are given by the associated flow rule

$$\dot{\boldsymbol{\epsilon}}^p = \frac{\partial f}{\partial \boldsymbol{\sigma}_e}\dot{\lambda} \tag{3.31}$$

The derivatives of the yield function are given by

[3] A potential function is used to describe the internal state of a material during plastic deformation, while a yield function is used to predict the onset of plastic deformation.

$$\begin{aligned}\frac{\partial f}{\partial \sigma_{e11}} &= \alpha_{11}\sigma_{e11} + \alpha_{12}\sigma_{e22} \\ \frac{\partial f}{\partial \sigma_{e22}} &= \alpha_{22}\sigma_{e22} + \alpha_{12}\sigma_{e11} \\ \frac{\partial f}{\partial \sigma_{e12}} &= 2\alpha_{66}\sigma_{e12}\end{aligned} \tag{3.32}$$

Let the equivalent stress be defined as

$$\overline{\sigma} = \sqrt{3g}. \tag{3.33}$$

while the equivalent plastic strain is defined as[4]

$$\dot{\overline{\epsilon}}^p = \frac{2}{3}\overline{\sigma}\dot{\lambda}. \tag{3.34}$$

For the case of 2/2 twill weave fabric, the $\alpha_{11} = \alpha_{22}$ since the anisotropy in the 1- and 2-axis is the same. Therefore, (3.29) becomes

$$2g(\boldsymbol{\sigma}) = \alpha_{11}\sigma_{e11}^2 + \alpha_{11}\sigma_{e22}^2 + 2\alpha_{12}\sigma_{e11}\sigma_{e22} + 2\alpha_{66}\sigma_{12}^2 \tag{3.35}$$

Moreover, the hardening law of the composite is established by the power-law function

$$k(\overline{\epsilon}^p) = \left(\frac{\overline{\epsilon}^p}{A}\right)^{n^{-1}} \tag{3.36}$$

where n is a strain hardening coefficient (no units) and A is a strength coefficient [MPa^{-n}]. Both of these parameters are hardening constants.

A second function that can be used as a potential function is the equation of the Tsai-Wu criterion. The use of a failure criterion as a potential function has been reported before [41]. The function used in the present work is given by

$$g(\boldsymbol{\sigma}) = f_1\sigma_{e11} + f_2\sigma_{e22} + f_{11}\sigma_{e11}^2 + f_{22}\sigma_{e22}^2 + f_{66}\sigma_{e12}^2 + 2f_{12}\sigma_{e11}\sigma_{e22} \tag{3.37}$$

and the coefficients are given by (2.6) and (2.8). The advantage of this equation is that it includes coupling parameters between the stress components and the coefficients are directly related to the strength of the material. Moreover, the Tsai-Wu criterion is proven to describe the behavior and failure of orthotropic materials with reasonable accuracy, therefore, the onset of plasticity is better predicted through this equation.

The complete yielding function is again described by (3.30) and the plastic strains by (3.31). A hardening law that follows a power-law function is established in this case as well given by (3.36). The coefficients in (3.37) are expressed in terms of the proportionality limit values to indicate the onset of plasticity. Therefore, the coefficients become

$$\begin{aligned} f_1^o &= \frac{1}{F_{1t}^o} - \frac{1}{F_{1c}^o}, \quad f_{11}^o = \frac{1}{F_{1t}^o F_{1c}^o} \\ f_2^o &= \frac{1}{F_{2t}^o} - \frac{1}{F_{2c}^o}, \quad f_{22}^o = \frac{1}{F_{2t}^o F_{2c}^o} \\ f_{66}^o &= \frac{1}{{F_6^o}^2}, \quad f_{12}^o \cong -\frac{1}{2}(f_{11}^o f_{22}^o)^{1/2} \end{aligned} \tag{3.38}$$

[4]The analytical explanation is presented in Appendix A.

The ultimate strength values are used to determine the final failure of the material after hardening occurred.

Regarding the plasticity model, some assumptions hold and they are presented below:

- Yield surface growth and translation are assumed.
- Linear elastic behavior is assumed followed by plastic behavior with isotropic and kinematic hardening.
- Small strains and plane stress conditions are assumed.

In order for the yield function to grow and translate, it has to be dependent on the accumulated plastic multiplier and back stress. These are internal history variables that evolve with plastic deformation. Moreover, the strain tensor can be split into an elastic contribution and a plastic contribution, $\boldsymbol{\epsilon} = \boldsymbol{\epsilon}^e + \boldsymbol{\epsilon}^p$ with the plastic strain being an internal (history) variable. The elastic properties of the material are given by the reduced stiffness matrix and the linear elastic behavior is given by (3.17). The plastic properties are described via the yield function $f(\boldsymbol{\sigma}, \lambda, \boldsymbol{D}, \boldsymbol{\sigma}^{back})$. The evolution of plastic strains is governed by the plastic evolution law given by (3.31). The plastic evolution law has to fulfill the Kuhn-Tucker loading and unloading conditions

$$f \leq 0,\ \dot{\lambda} \geq 0,\ f\dot{\lambda} = 0 \tag{3.39}$$

and the consistency equation

$$f = 0,\ \dot{f}\dot{\lambda} = 0 \tag{3.40}$$

Finally, the isotropic hardening equation is given by

$$k(\lambda) = \left(\frac{\lambda}{A}\right)^{n^{-1}} \tag{3.41}$$

and the kinematic hardening [1] by the Armstrong-Frederick kinematic hardening equation, which is defined as

$$\dot{\boldsymbol{\sigma}}^{\text{back}} = H_1 \dot{\boldsymbol{\epsilon}}_p - H_2 \dot{\lambda} \boldsymbol{\sigma}^{\text{back}}. \tag{3.42}$$

H_1 [GPa] and H_2 (dimensionless) are the unknown, non-negative material constants. Finally, the relative principal stresses are given by $\boldsymbol{\sigma}^{\text{rel}} = \boldsymbol{\sigma} - \boldsymbol{\sigma}^{\text{back}}$.

The two potential functions presented above can be used to determine the catastrophic failure of the material. The main difference between them is that the quadratic potential function does not include the anisotropy between tension and compression. The failure envelope is symmetric to both axes. The Tsai-Wu failure envelope accounts for the difference in tensile and compression of the material and therefore, the envelope is asymmetric. A comparison of the two envelopes is presented in Figure 3.3. This asymmetry results in an elongated part of the curve in the third quadrant (compression). In general, the different anisotropic failure criteria used in composites differ mostly in the third quadrant and this should be considered when selecting a criterion. In this study, the Tsai-Wu equation is used as a potential function due to this asymmetry in the material behavior. Another reason for choosing the Tsai-Wu function is that its coefficients are directly related to the strength of the material which can be experimentally obtained.

Isotropic hardening is related to the way the envelope surface or yield surface develops. In the case of isotropic hardening, the yield surface grows in size isotropically in every direction as a response to the material flow. Figure 3.3 shows an example of the isotropic growth of the two surfaces. In kinematic hardening, the yield surface is shifting or translating instead of growing. Kinematic hardening models capture better the behavior of the material when it is subjected to tension-compression loading cycles. When a material is loaded in tension-zero-tension loading cycles (same direction), isotropic hardening is adequate. An indicator of kinematic hardening is the stress-strain behavior after the material is loaded in tension over the yielding point and then loaded in compression over the yielding point in compression. The yielding point in compression in this case will be different than the one in tension. Finally, a mixed hardening model is often used in the literature, with isotropic and kinematic hardening acting at the same time. This type of hardening is used in this study as well.

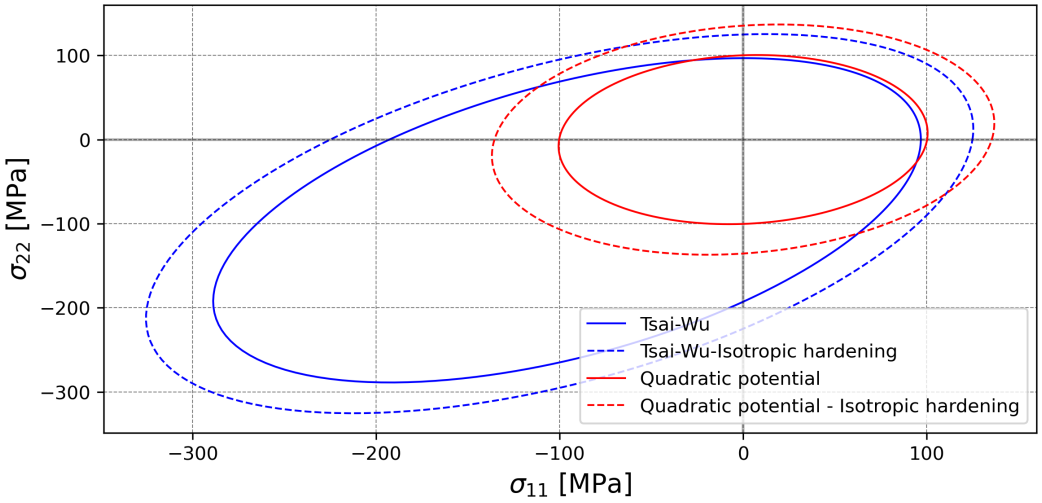

Figure 3.3: Schematic representation of the failure envelopes of the Tsai-Wu and the quadratic potential and the expansion of the corresponding envelopes.

3.3. Implementation in Python

The damage and plasticity models presented in Section 3.2, need to be combined and implemented in a computational procedure. This procedure is developed in Python. The most important part of the plasticity models is their approach to calculating the plastic multiplier or equivalently the plastic strain. Calculating the plastic multiplier through the analytical plasticity equations can be a difficult and inefficient approach. In computational mechanics, plasticity problems are typically solved iteratively. In this study, a numerical method named return mapping algorithm is used to update the internal state of material during plastic deformation [18] [56] [23].

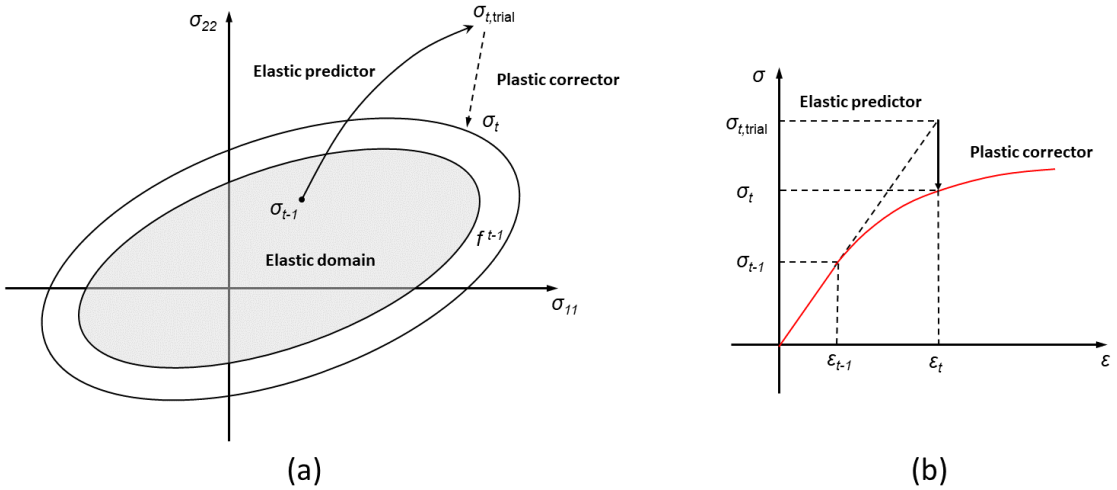

Figure 3.4: Schematic representation of the return mapping algorithm. (a) Representation of the algorithm in the stress space and (b) how the algorithm predicts the stress-strain curve.

The basic idea behind the return mapping algorithm is to determine the amount of plastic strain that has occurred in a material under a given set of loading conditions. This is done by comparing the current stress state to the yield surface via the yield function. If the current stress state is within the yield surface, the material is still in the elastic range and no plastic deformation has occurred. If the current stress state is outside the yield surface, the material has undergone plastic deformation, and the return mapping algorithm is used to determine the amount of plastic strain that has occurred. The algorithm starts by assuming an initial guess for the plastic strain increment and calculates the corresponding stress increment using the material's constitutive equation. If the stress increment is greater than the yield stress, the material has undergone plastic deformation, and the plastic strain increment is adjusted based on the material's yield function. A schematic of the algorithm in the stress state and how the algorithm predicts the stress-strain curve is presented in Figure 3.4.

The overall approach is based on strain incrementation. Firstly, all history variables $\boldsymbol{h} = \{\boldsymbol{\epsilon}^p, \lambda, \boldsymbol{D}, \boldsymbol{\sigma}^{back}\}$ and the reduced stiffness matrix are collected and initiated. Secondly, the strain in the global coordinate system[5], $\boldsymbol{\epsilon}_t$, is increased. A prediction of the stress, $\boldsymbol{\sigma}_{t,\text{trial}}$, is calculated based on the assumption that the material is in the elastic regime and no evolution of damage and plastic strain has occurred. Therefore, the history variables are equal to those of the previous time step. The stress in the global coordinate system is calculated from $\boldsymbol{\sigma}_{t,\text{trial}} = \mathbb{Q}^d(\boldsymbol{\epsilon}_t - \boldsymbol{\epsilon}^p_{t,\text{trial}})$. The equivalent stress in the principal material system is calculated through the rotation matrix (3.11). Based on this stress, the yield function $f(\boldsymbol{\sigma}_{t,\text{trial}}, \boldsymbol{h}_{t,\text{trial}})$ is calculated. If the yield function is less or equal to zero the trial stress is permissible and no evolution or correction of the plastic strain is required. If the yield function is greater than zero the trial stress is not permissible and the evolution of plastic strain occurs. The stress and plastic multiplier take some guess values and the $\boldsymbol{\epsilon}^p_t, \Delta\lambda$ and $\boldsymbol{\sigma}^{\text{back}}$ need to be calculated so that $f = 0$, (3.31), (3.41) and (3.42) are satisfied. These equations are re-written in the following form [18]

$$\begin{aligned} \boldsymbol{\epsilon}^p_t &= \boldsymbol{\epsilon}^p_{t-1} + \Delta\lambda^t \frac{\partial f^t}{\partial \boldsymbol{\sigma}} \\ \left(\boldsymbol{\sigma}^{\text{back}}\right)_t &= \left(\boldsymbol{\sigma}^{\text{back}}\right)_{t-1} + H_1^{\text{kin}}\, \Delta\lambda^t \frac{\partial f^t}{\partial \sigma} - H_2^{\text{kin}}\, \Delta\lambda^t \left(\boldsymbol{\sigma}^{\text{back}}\right)_t \end{aligned} \tag{3.43}$$

[5]The externally applied strain is always in the global (laminate) coordinate system

with $\boldsymbol{\epsilon}_t^p = \boldsymbol{\epsilon}_t - \mathbb{S}_t^{\mathrm{d}}\boldsymbol{\sigma}_t$. This system of non-linear equations can be solved iteratively for $\boldsymbol{\sigma}_t, \Delta\lambda$ and $\Delta\boldsymbol{\sigma}^{\text{back}}$. It should be noted that the system of equations above refers to the local coordinate system, so all the required rotations should be considered. After the corrected stress and plastic strain values are obtained, the damage variables are calculated based on (3.24), (3.25) and (3.26) and the damaged stiffness matrix is updated. The history variables are updated and stored to be used in the next iteration. Finally, the equation of the final failure is calculated and checked and if the value is greater than zero the whole approach is stopped. If no final failure has occurred the procedure is followed again until failure occurs. It should be noted that the elastic properties in the developed model, are expressed in GPa so the stresses and strength values are expressed in GPa for consistency reasons.

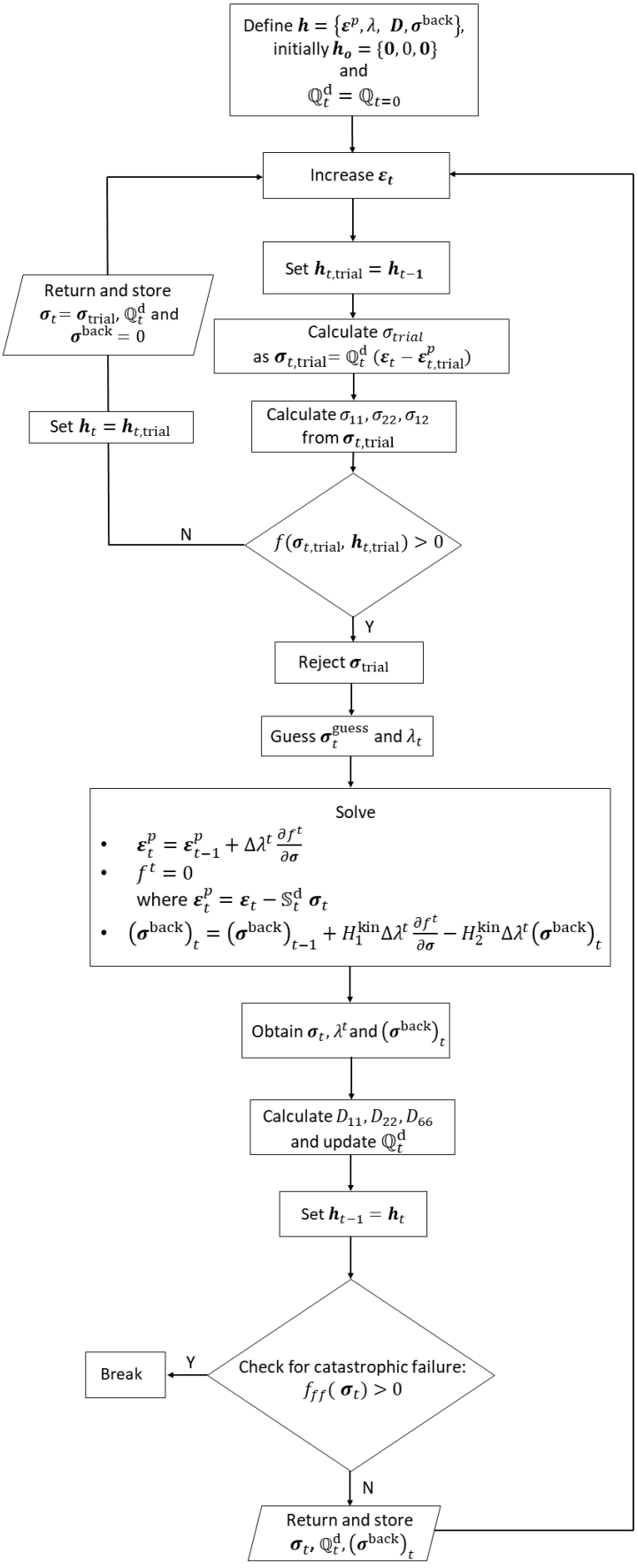

Figure 3.5: Flow chart of the algorithm for the calculation of $\boldsymbol{\sigma} = f(\boldsymbol{\varepsilon})$ curve.

4

Material testing

Understanding the in-plane mechanical behavior and the damage characteristics of 2/2 twill weave C/C-SiC is one of the objectives of this work. Mechanical tests are important not only to characterize the behavior of the material, which is not extensively studied in the literature but also to obtain the necessary data to be used in the material model. On the other hand, optical characterization is important to study the microstructure and validate that the infiltration of silicon was successful and resulted in the desired microstructural characteristics. Moreover, the fractured surfaces of the tested samples are studied to identify the failure mechanisms of C/C-SiC.

4.1. Specimens preparation

A number of specimens were produced and tested under in-plane monotonic and cyclic tension and compression loading, in order to study the mechanical behavior and damage evolution law of C/C-SiC. The angle θ, between fibers and loading direction, are $0^o, 30^o$ and 45^o in tension and in compression.

For specimen preparation, six C/C-SiC plates were manufactured from which the specimens were cut via waterjet-cutting. The manufacturing route is the same as the one described in Section 2.3.1. Specifically, two CFRP plates were manufactured via the autoclave technique and four via the warm-press technique. The pyrolysis and siliconization stages were followed and finally, the six CMC plates were produced. X-ray images of the plates were taken after the LSI process to validate that the silicon infiltration was uniform across the plates. Finally, the test specimens were cut from the plates via water-jet cutting. A schematic of the manufacturing timeline is presented in Figure 4.1. Pictures of the manufactured plates are presented in Appendix B.

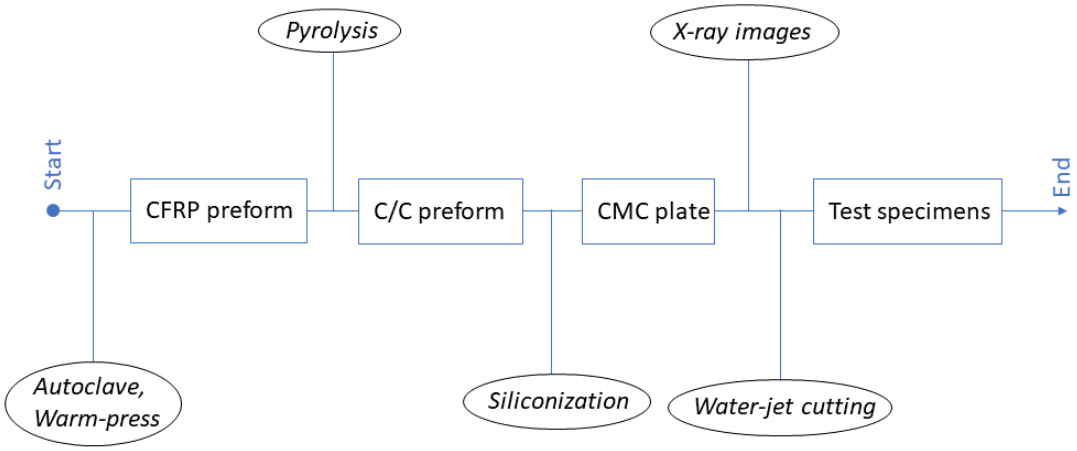

Figure 4.1: Timeline of the preparation of the specimens.

The dimensions of the tensile and compression test specimens are presented in Figure 4.2. These dimensions follow the DIN EN 658-1 and DIN EN 658-2 standards, respectively. Non-straight-sided test specimen geometry is chosen for the tensile tests over the straight-sided specimen geometry because it is more appropriate for determining the strength of the material, according to DIN EN 658-1.

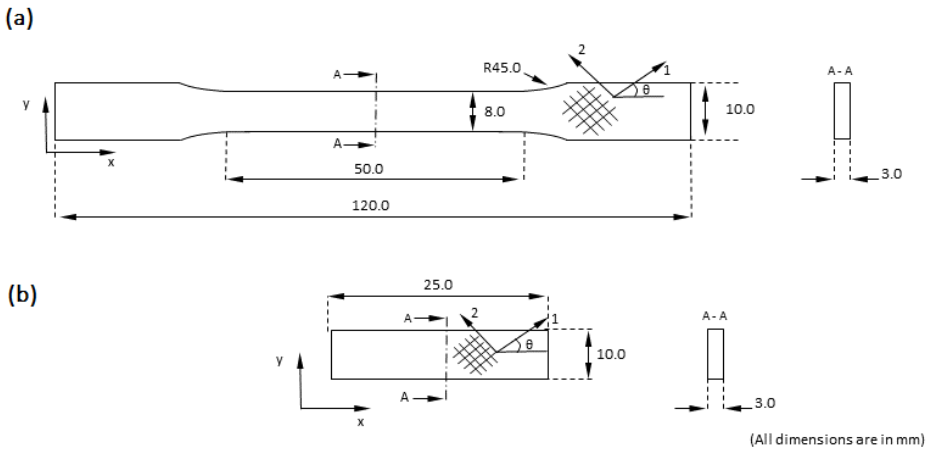

Figure 4.2: (a) Schematic of the tension specimens and (b) schematic of the compression specimens.

A unique name is given to every test specimen. The letters M and C refer to monotonic or cyclic loading, the letters T and C refer to tensile or compressive load, and the numbers 0, 30 and 45 refer to the angle θ between the fibers and the loading direction, respectively. For example, the MT3-30 refers to a specimen that is loaded with monotonic tensile load, is the third specimen of the batch and the angle between the loading direction and the fibers is 30^o.

As it is mentioned six CMC plates were manufactured in total. For the two of them, the autoclave technique was used to produce the CFRP preform and for the rest of them the warm-press technique was used. The only difference between the manufactured plates is at the first manufacturing stage. The pyrolysis and siliconization cycle that was used, was the same for all the plates. Therefore, not all the specimens are manufactured from the same plate. Even though two different techniques were used in the first stage of the manufacturing process, the density, porosity and fiber volume fraction is kept within the same range of values.

This is critical to assure that all the different specimens have the same microstructural properties. In Table 4.1 the actual values of the micromechanical parameters and the manufacturing technique that was used for the production of each specimen, are presented.

Micromechanical properties				
Specimen	Process	Density [g/cm^3]	Porosity [%]	V_f [%]
MT#-0, CT#-0	Autoclave	1.86	1.91	53
MT#-30, CT#-0	Warm-press	1.88	2.33	56
MT#-45, CT#-45	Warm-press	1.87	1.98	55
MC#-0, CC#-0	Autoclave	1.85	2.02	56
MC#-30, CC#-30	Warm-press	1.87	1.98	57
MC$-45, CC#-45	Warm-press	1.87	1.81	56

Table 4.1: Density, porosity and fiber volume fraction of the manufactured specimens.

4.2. Scanning electron microscopy

It is important to study the resulting microstructure of the tested material/specimens in order to validate that it is the same as the one presented in the literature. It is also important to check for any differences between the plates manufactured via autoclave and warm-press processes and finally study the fractured surfaces of the tested specimens. SEM is used to obtain magnified pictures of the microstructure and fractured surfaces.

Small pieces of material from every plate are used to prepare SEM samples. For the sample preparation, a conductive resin (Technovit 5000) was used to embed the material. Then the samples were sanded and polished in order to flatten the studied surfaces and remove most of the scratches that were present. Before the samples are placed in the SEM, they need to be cleaned with isopropanol and be out-gassed in the out-gassing chamber. SEM (Jeol JSM IT-100) is used with energy-dispersive X-Ray spectroscopy (EDS).

The microstructure of the specimens manufactured via autoclave and of those manufactured via warm-press are similar. The two microstructures are presented in Figure 4.3. The main characteristics are the C/C areas (black) and the SiC areas (grey). The samples present vertical SiC areas as a result of the infiltrated Si inside the fiber bundle cracks of the C/C preform. Consequently, the fiber bundles are separated in C/C blocks which are surrounded by SiC. Some of these vertical cracks are formed during the manufacturing of the CFRP part and some of them after the pyrolysis step due to the shrinkage of the material. Both microstructures present more vertical SiC areas than the microstructure presented in the literature though (Figure 2.4). The samples produced via warm-press presents also wide SiC areas that are extended horizontally. These SiC isles are mostly located in the area between the fiber bundles. This means that the CFRP part manufactured via the warm-press technique presented gaps in the resin that were filled with Si after siliconization.

A closer examination of the SiC areas shows that Si has only reacted with C close to the filaments while Si further away is unreacted. As a result, a thin layer of SiC is formed next to the C/C areas. This observation is validated by the EDS measurements at three different locations (see Appendix C, Figure C.11). Indeed, the light grey areas are almost entirely Si, the dark grey areas are SiC and the black areas are the carbon reinforcement. Moreover, inside

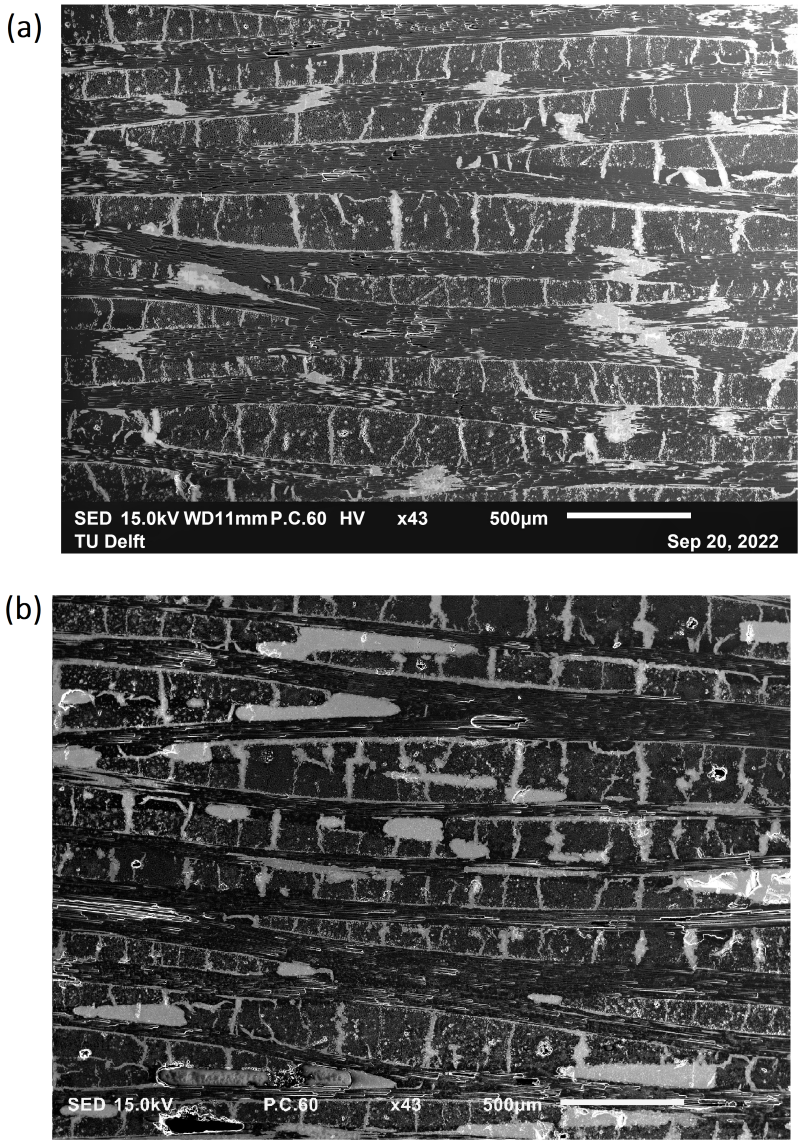

Figure 4.3: SEM pictures of the specimens manufactured via (a) autoclave process and (b) warm-press process

the fiber bundle, the filaments are surrounded by dark C areas as a result of the pyrolysis stage, therefore these areas are referred to as C/C areas (Figure 4.4).

Overall, the microstructure of the tested material is similar to the one presented in the literature. SiC and Si areas are visible in the material and SiC is located close to the C/C areas as it was expected. The fiber bundle is divided into C/C blocks that are surrounded by SiC/Si areas. A larger number of C/C blocks is observed compared to the literature and in some of the specimens, the SiC/Si areas are more extended. Furthermore, the SiC areas in the SiC/Si isles are narrower than the SEM pictures presented in the literature (Section 2.4). This means that Si did not react efficiently with C to convert into SiC.

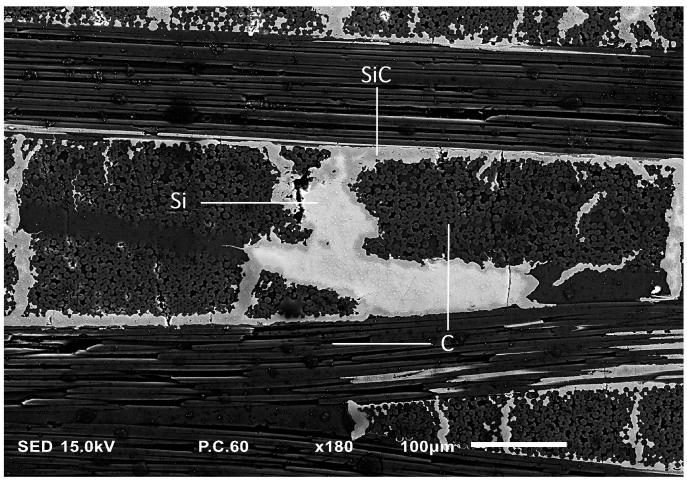

Figure 4.4: SEM picture of the SiC area with higher magnification. The Si (light grey) and SiC (dark grey) area are apparent.

4.3. Mechanical testing

Through mechanical tests, the material response is studied and correlated to the microstructure that was presented in Section 4.2. All four types of mechanical tests (monotonic and cyclic, tensile and compression tests) were conducted on a 10-kN Zwick/Roell Z010 machine at room temperature, pictures of which are presented in Appendix C. A position-controlled testing mode with a deformation rate of 1.0 [mm/min] was used. For the cyclic tensile tests, certain force limits were set in order to obtain the loading and unloading cycles. The lower force limit was always at 0 N and the upper force limit was initialized at 200 N and was increased by 200 N after each cycle. For the cyclic compression tests the lower force limit was 0 N, and the upper limit started at 400 N and was increased by 400 N after every cycle. For the gripping of the specimens, wedged-type grip faces were used for the tensile tests and flat plates for the compression tests. An extensometer was used during the tensile tests to measure the strain while the deformation was measured from the load cell in the compression tests. Due to the lack of available extensometers for the compression tests, the strain had to be calculated from the measured deformation. In order to promote the accuracy of the results, at least five valid measurements were obtained for each case according to the DIN standards.

4.3.1. Tensile tests

The monotonic and cyclic tensile response of the material is presented first. The load and strain data were simultaneously recorded during the tests and the stress was calculated for every measurement by dividing the recorded load, F [N], with the cross-section, A [mm^2], of each specimen, $\sigma = F/A$ [MPa].

When the angle θ between the loading direction and the 1-principal material direction is 0^o the response of the material in the monotonic loading is slightly non-linear (Figure 4.5). A small linearly elastic regime can be identified at small stresses, typically between $0-20$ [MPa] and after that, the response is non-linear. The failure is brittle and abrupt.

For $\theta = 0^o$ the material response in cyclic loading is presented in Figure 4.6. Narrow hysteresis loops are observed in this case which means that a small amount of energy is lost during the cycles in the form of heat. The dissipated energy for each cycle is given by the area between the loading and unloading curves. Moreover, upon reloading the apparent yield

strength is equivalent to the maximum stress seen in the previous loading sequence.

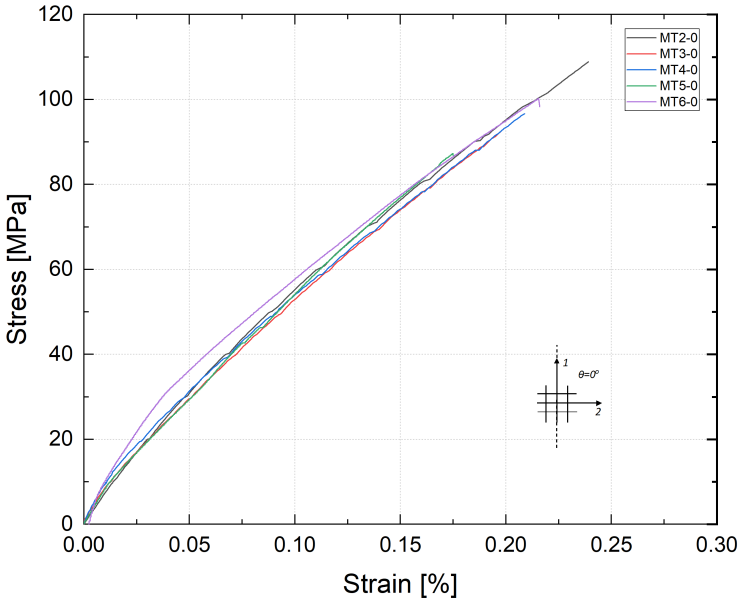

Figure 4.5: Monotonic tensile stress-strain curves of C/C-SiC with $\theta = 0^0$.

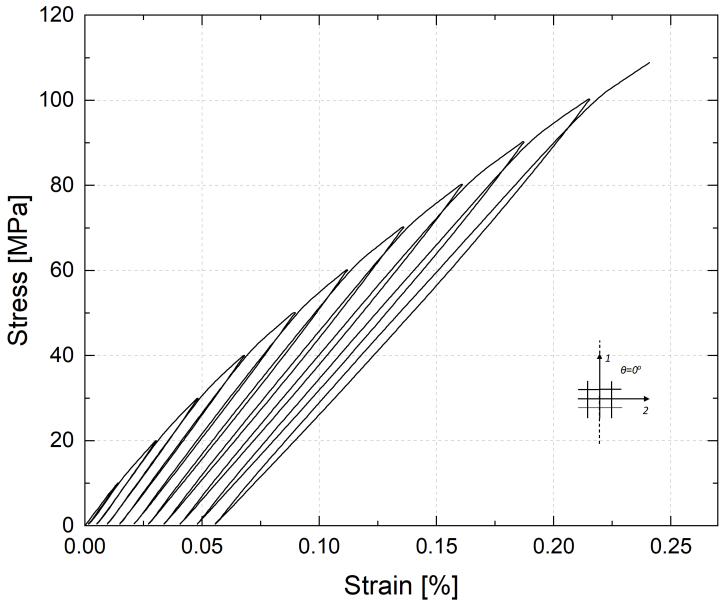

Figure 4.6: A typical cyclic tensile stress-strain curve of C/C-SiC with $\theta = 0^0$.

All tested specimens present relatively flat fracture surfaces (Figure 4.7 (a)). Analysis of the fractured surfaces shows that for specimens with $\theta = 0^o$, the effect of pull-out of the C/C blocks and fibers is dominant (Figure 4.7). These C/C blocks are surrounded by SiC matrix and they are debonded from the interface as the load increases. Finally, they are pulled out resulting in protruding fiber blocks or cavities in the fractured surface. Moreover, cracks are observed in the matrix areas and the surface pattern indicates that a brittle fracture occurred. It should be mentioned that the specimens used in this case ($\theta = 0^o$) were manufactured via the autoclave technique.

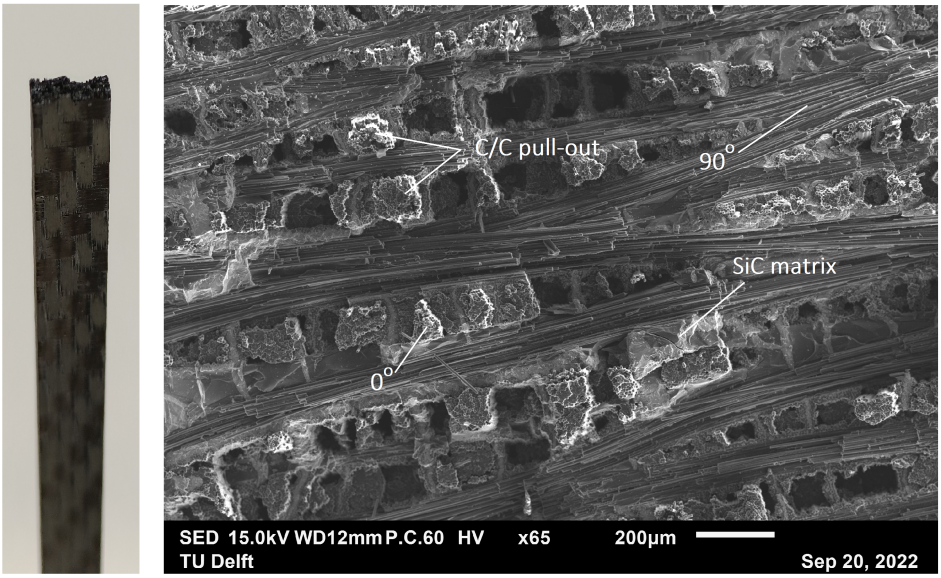

Figure 4.7: (a) Fractured tensile specimen for the case of $\theta = 0^o$ and (b) SEM picture of the fractured surface. The red arrows show the pull-out of C/C blocks and the white arrows the fracture surface of the matrix areas.

In the case of $\theta = 30^o$ the material response is almost completely non-linear (Figure 4.8). A linear elastic regime is difficult to be identified in this case. Furthermore, the hysteresis loops are wider which indicates higher dissipated energy and the resulting plastic strains are larger.

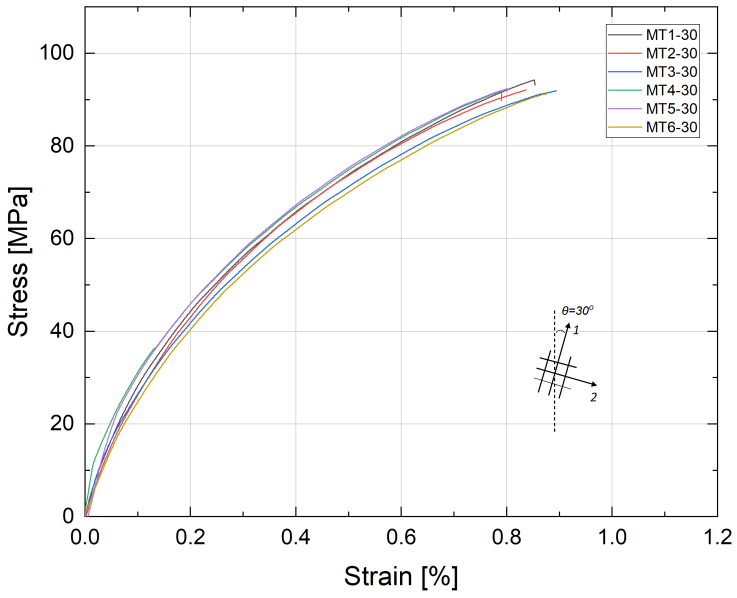

Figure 4.8: Monotonic tensile stress-strain curves of C/C-SiC with $\theta = 30^0$.

Most of the tested specimens present relatively flat fracture surfaces with some protruding fiber bundles (Figure 4.10). Pull-out effect of fibers and fiber bundles is also apparent in this case, especially for bundles along the 30^o angle which are closer to the direction of the applied load. The propagated cracks are deflected slightly by the fibers but no extended 30^o or 60^o fracture planes are observed. Once the cracks reach the C/SiC interface they cause debonding of the interface and shortly after, the rapture of the C/C block occurs.

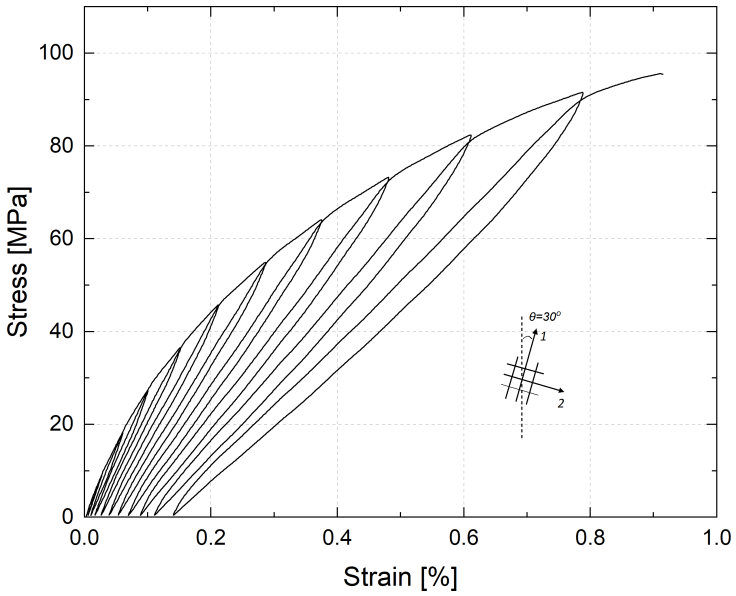

Figure 4.9: A typical cyclic tensile stress-strain curve of C/C-SiC with $\theta = 30^0$.

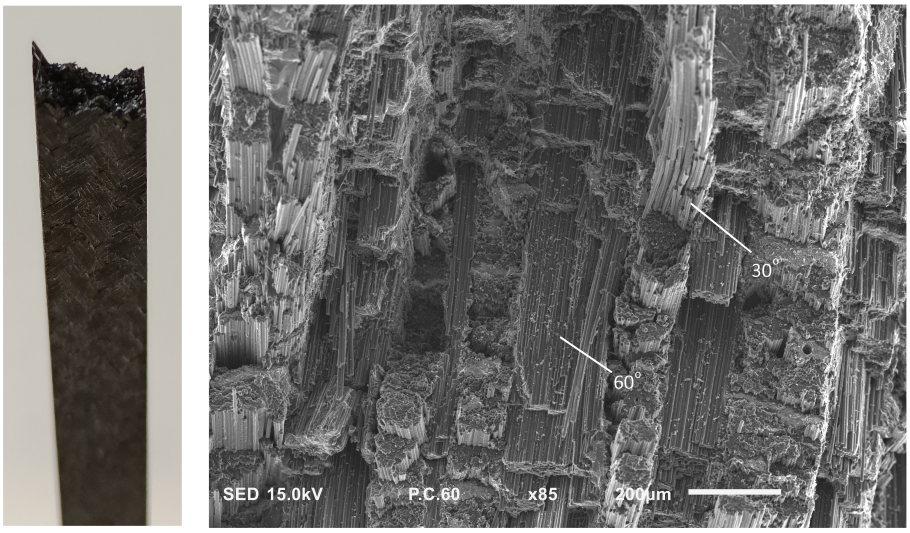

(a) (b)

Figure 4.10: (a) Fractured tensile specimen for the case of $\theta = 30^o$ and (b) SEM picture of the fractured surface.

The final case for the tensile tests is the case of $\theta = 45^o$. A completely non-linear response of the material is observed in this case as well (Figure 4.11). Identifying a linear elastic regime is again difficult since no apparent linearity exists. The hysteresis loops are similar to the ones of case $\theta = 30^o$ but wider than the ones of $\theta = 0^o$.

The tested specimens present a relatively flat fracture surface with a few protruding fibers and fiber bundles in this case too (Figure 4.13). Fiber bundle pull-out is extensively observed in the fractured surface. Ruptured C/C blocks are clearly visible and compared to the case of $\theta = 30^o$, the length of the blocks is almost the same everywhere. The specimens used for tensile with $\theta = 30^o$ and 45^o were manufactured via the warm-press technique.

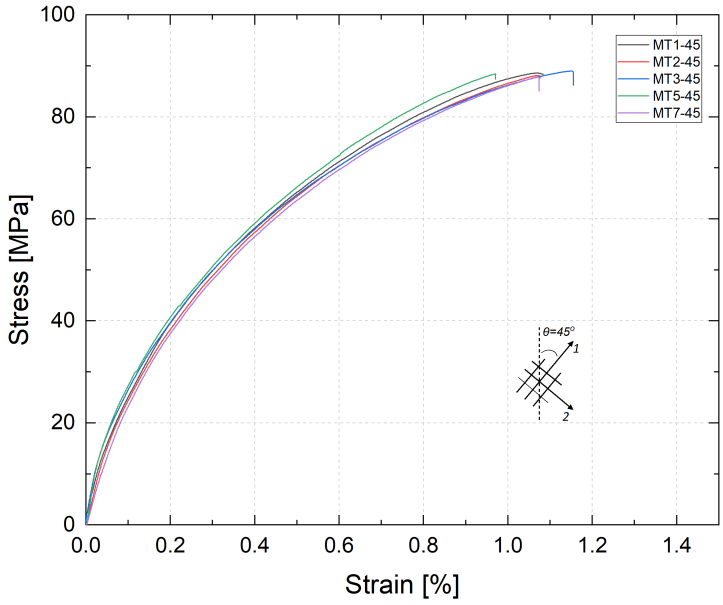

Figure 4.11: Monotonic tensile stress-strain curves of C/C-SiC with $\theta = 45^0$.

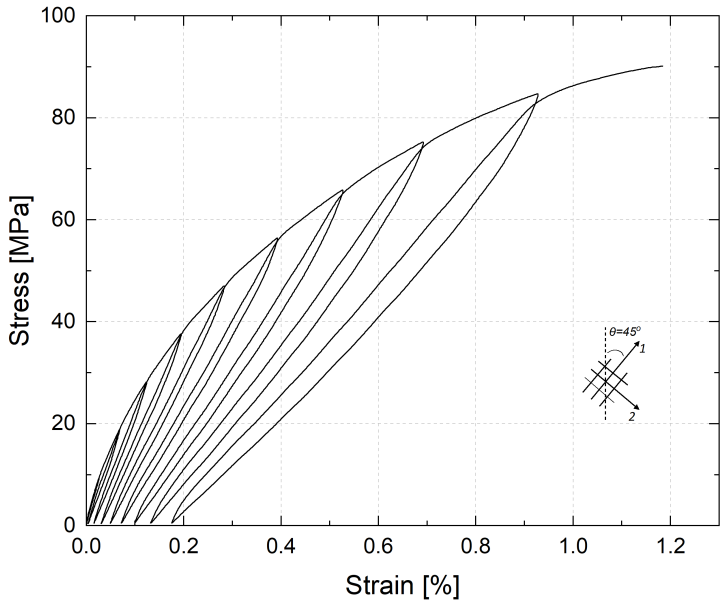

Figure 4.12: A typical cyclic tensile stress-strain curve of C/C-SiC with $\theta = 30^0$.

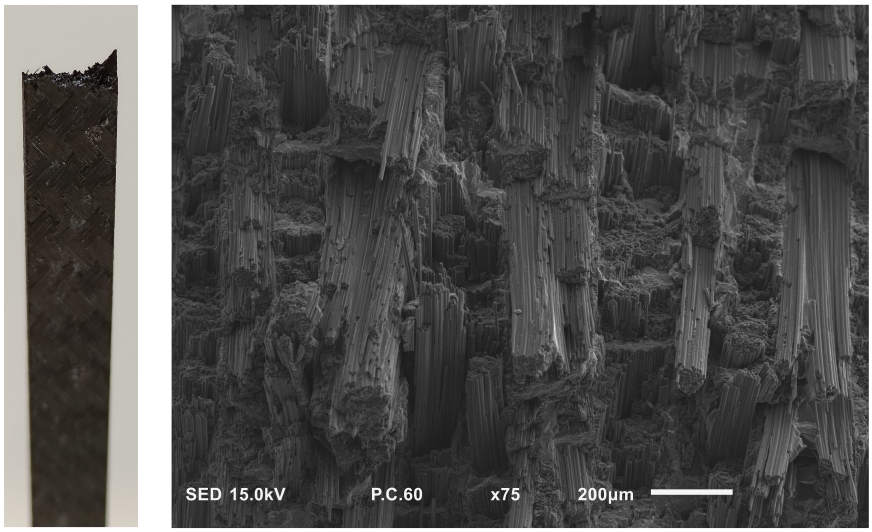

Figure 4.13: (a) Fractured tensile specimen for the case of $\theta = 45^o$ and (b) SEM picture of the fractured surface.

4.3.2. Compression tests

For the compression tests, the deformation was recorded through the cross-head. The measured deformation includes the deformation of various parts of the testing set-up. The set-up can be considered as a springs-in-series system. Therefore, the pure deformation of the material is given by the total deformation (measured), once the deformation of the rest of the system is subtracted. In order to do that, steel coupons, with a known Young's modulus and the exact dimensions as the CMC specimens, were prepared and tested using the same experimental set-up. The Young modulus of the steel coupons is known and equal to 200 [GPa]. Therefore since the coupon's length and cross-section are known, for every force data, the deformation of the steel coupon is calculated. This deformation is subtracted from the measured one and finally, the force-displacement curve of the experimental set-up is obtained (Figure C.6). The curve is mostly linear with a small non-linear regime at small forces. Therefore, from every value of deformation in every data set, the deformation of the machine is subtracted and finally the strain is calculated as $\epsilon\,[\%] = (e/L) \times 100$. The raw experimental data of the compression tests as well as the procedure that was followed for processing them are presented in Appendix C.

Monotonic and cyclic tests were performed in compression for $\theta = 0^o, 30^o$ and 45^o and the results are presented below. When the angle between the fibers and the loading direction is $\theta = 0^o$, the material response in the monotonically increased load is almost completely linear (Figure 4.14). The final failure is brittle and abrupt without apparent material hardening before that. It should be noted that the scatter in the compressive strength between the specimens is caused by internal defects of the material due to the manufacturing process. Specifically, after water-jet cutting, some of the specimens had suffered delamination especially close to the edges. The ones with no apparent delamination were chosen for testing but internal, non-visible delaminations might still exist.

The raw force-deformation curves of the cyclic compression tests are presented in Figure 4.15 as they were obtained from the machine since the stress-strain data after processing

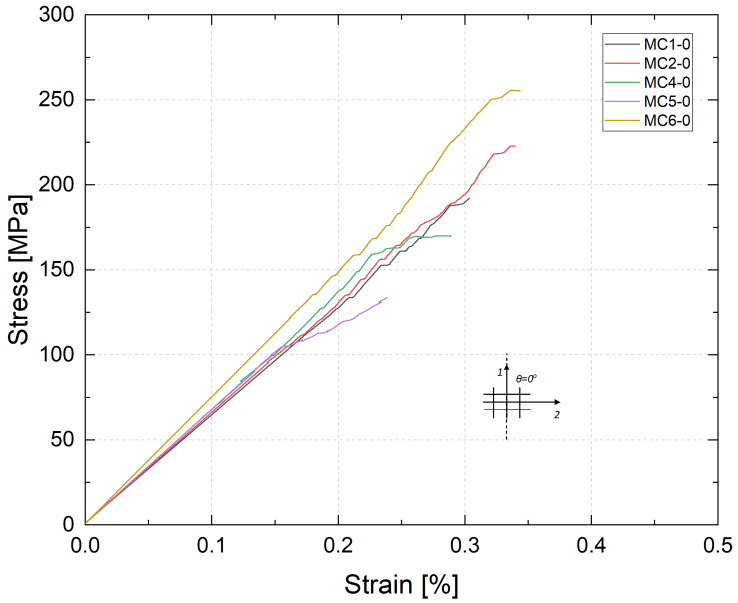

Figure 4.14: Monotonic compressive stress-strain curves of C/C-SiC with $\theta = 0^0$.

could not be corrected entirely (Appendix C). Overall, the hysteresis cycles are narrow and the material behavior is almost entirely linear in this case. Small permanent deformation is observed after a few loading and unloading cycles.

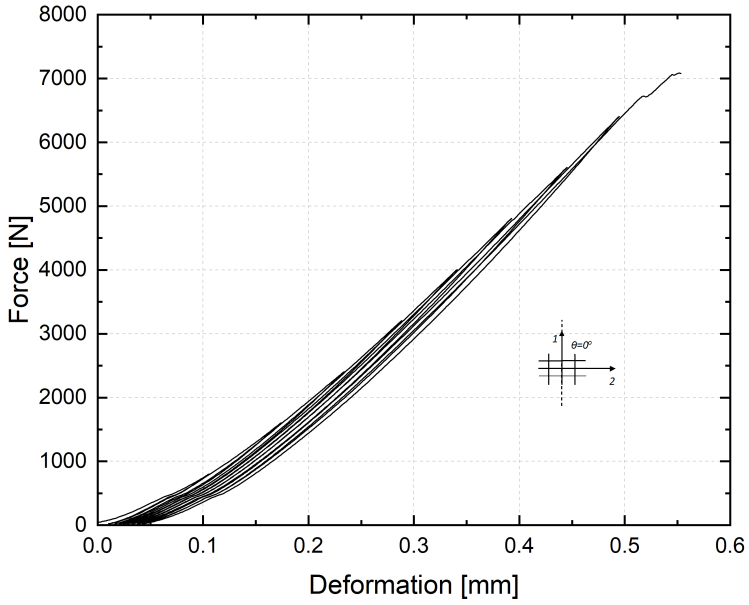

Figure 4.15: Force-displacement curve of a specimen loaded with cyclic compression load and with $\theta = 0^o$.

Regarding the fracture of the test specimens, macroscopically, they exhibit cracks and separation in the thickness direction. This separation is mostly observed in the outer plies and some specimens present fragmentation close to the edges. Microscopically, the SEM pictures show that interlaminar cracks are present close to the fractured area. Translaminar and intra-tow cracks through the fiber bundles are present in the fractured area. Moreover, the crushing of the fibers that are aligned with the direction of the load can be seen. The specimens in this case were manufactured via the autoclave technique.

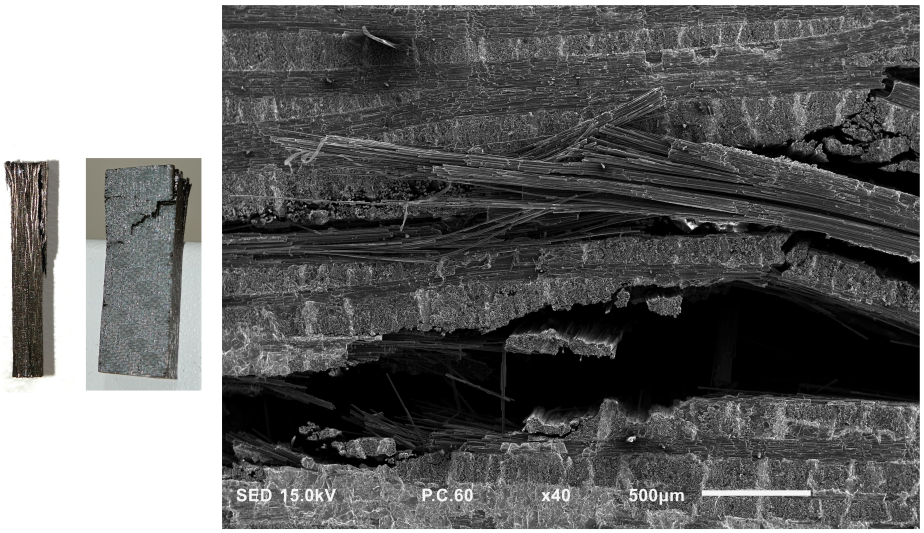

Figure 4.16: (a) Fractured compression specimen for the case of $\theta = 0^o$ and (b) SEM picture of the fractured specimen.

For the case of $\theta = 30^o$, the monotonic response of the material is linear in the biggest part of the stress-strain curve and a narrow hardening regime exists until the ultimate strength of the material is reached (Figure 4.17). After that, a small region where the material softens is present until the final failure point is reached. Failure is not as abrupt as in the previous cases, due to the drop in stress. Wider hysteresis loops are observed compared to the case of $\theta = 0^o$ (Figure 4.18).

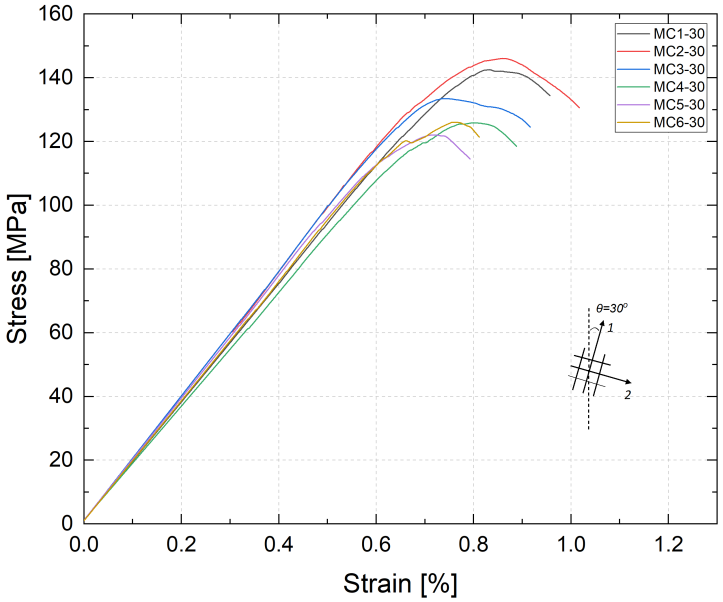

Figure 4.17: Monotonic compressive stress-strain curves of C/C-SiC with $\theta = 30^0$.

Macroscopically the tested specimens present fracture planes and fiber crushing. The fibers oriented at 30^o relative to the loading direction are the ones that have been crushed. Microscopically, a brittle fracture is observed in the structure due to a large number of interlaminar

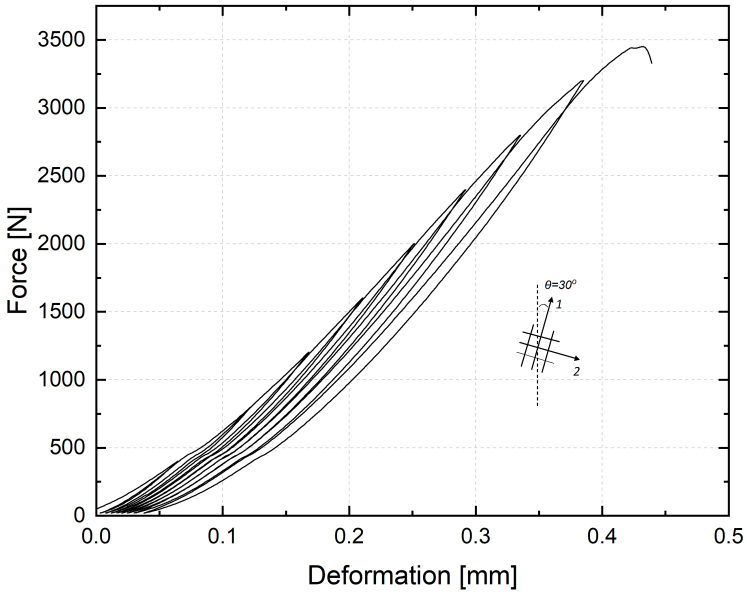

Figure 4.18: Force-displacement curve of a specimen loaded with cyclic compression load and with $\theta = 30^o$.

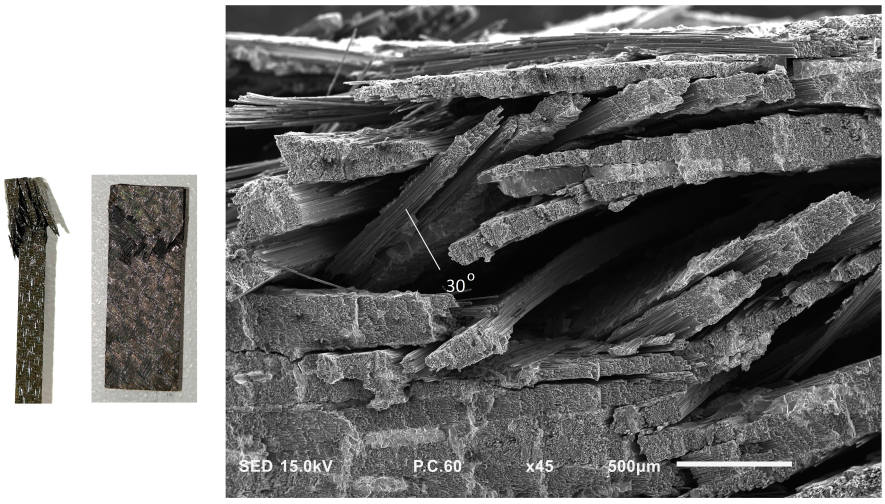

(a) (b)

Figure 4.19: (a) Fractured compression specimen for the case of $\theta = 30^o$ and (b) SEM picture of the fractured specimen.

and translaminar cracks. Moreover, a few intra-tow cracks are also observed. Crushing of the fibers along the 30^o can be seen as well. The fractured area shows a plethora of C/C blocks due to the brittle nature of the material and the crack propagation process.

The last case is the compression test of $\theta = 45^o$. The response of the material in the monotonic load is presented in Figure 4.20. The stress-strain curve is again mostly linear with a hardening regime before the ultimate strength of the material is reached. After that, the material softens until the final failure. The fracture behavior is not as abrupt as in the case of $\theta = 0^o$. Wider hysteresis loops are present in this case, wider than in the previous two cases (Figure 4.21).

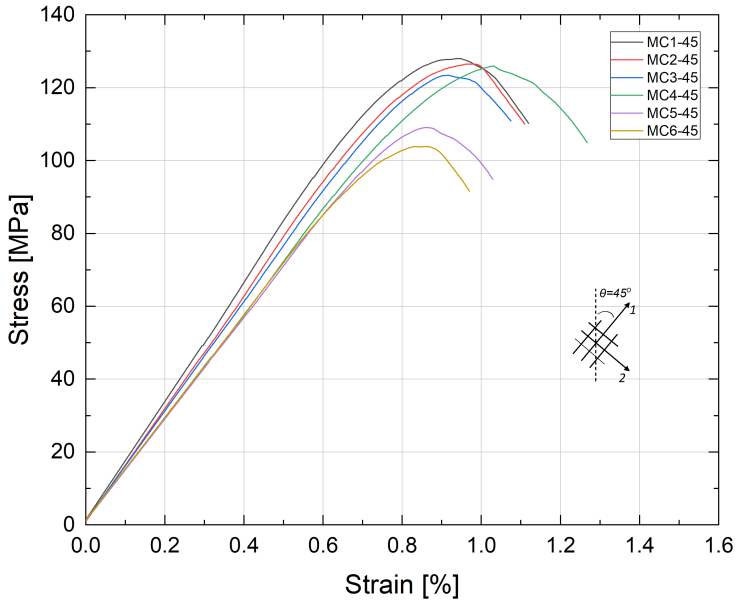

Figure 4.20: Monotonic compressive stress-strain curves of C/C-SiC with $\theta = 45^0$.

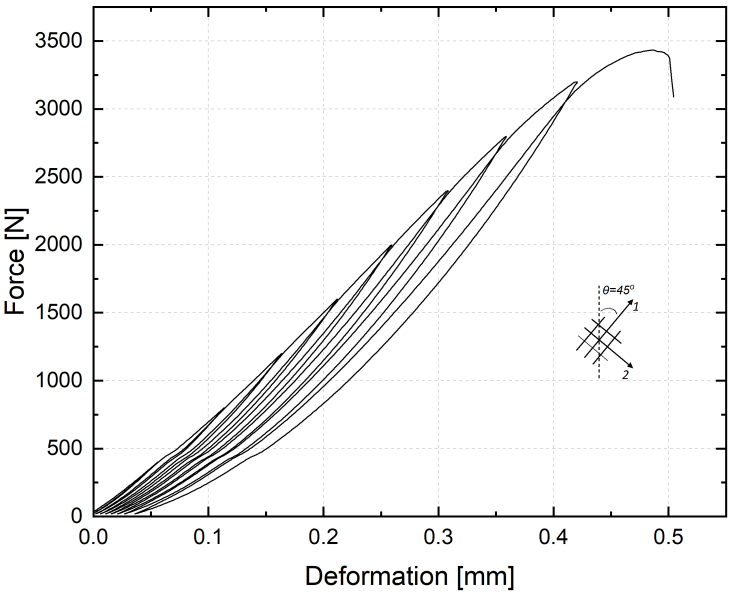

Figure 4.21: Force-displacement curve of a specimen loaded with cyclic compression load and with $\theta = 45^o$.

The tested specimens present fracture planes with 45^o angle and fiber crushing. Overall, the fracture is similar to the case of 30^o with a large number of interlaminar and intra-tow cracks and fiber crushing in the fracture area. The $\theta = 30^o$ and 45^o specimens were manufactured through the warm-press technique. A discussion on the overall material properties obtained from tests is presented in Section 4.4.

4.4. Material characterization

The results from the mechanical tests are further processed and all the available and relative information is presented in this section. Specifically, the elastic and failure properties and the damage evolution laws are obtained from the experimental data.

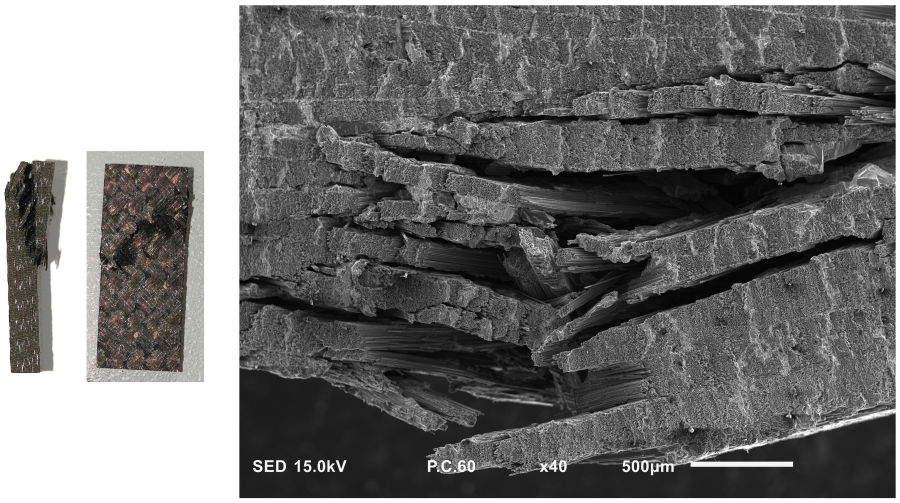

(a) (b)

Figure 4.22: (a) Fractured compression specimen for the case of $\theta = 45^o$ and (b) SEM picture of the fractured specimen.

The elastic modulus of the material is obtained from the linear regime of the stress-strain curves. The tensile curves of $\theta = 30^o$ and 45^o are completely non-linear thus identifying a linear regime is difficult if not impossible. Based on the DIN EN 658-1 and ASTM C 1275 – 00 standards, there are different types of CMC behaviors and approaches that can be followed to obtain Young's modulus. There are three main categories of CMCs based on their mechanical response. In the first category, the linear behavior is located after an initial toe region and before the non-linear part (hardening) of the stress-strain curve. In the second category, the linear behavior starts at the origin of the curve until the non-linear part of the curve. In the third and final category, the stress-strain curve is completely non-linear. When the linear behavior starts at the origin the elastic modulus is obtained through the linear fit of the elastic region. But for materials with no linear section, the recommended procedure is to fit linearly the region between $0.1\sigma^t_{xx}$ and $0.5\sigma^t_{xx}$, where σ^t_{xx} is the tensile strength. It is mentioned that other limits can also be used depending on the material. If the $0.1\sigma^t_{xx}$ and $0.5\sigma^t_{xx}$ limits are used, the value of the elastic modulus is presented in Table 4.2.

Elastic properties		
Loading angle	$E^t_{xx} = E^t_{yy}$ [GPa]	$E^c_{xx} = E^c_{yy}$ [GPa]
0^o	52.43 ± 2.26	68.57 ± 3.14
30^o	19.71 ± 1.14	19.09 ± 0.65
45^o	16.26 ± 0.41	16.27 ± 0.56

Table 4.2: Elastic properties determined according to the DIN standards.

The elastic modulus obtained within these limits is considered as the apparent Young modulus. These values are underestimating the actual modulus which is higher. As it can be seen in Figures 4.6, 4.9 and 4.12, the plastic strains between $0.1\sigma^t_{xx}$ and $0.5\sigma^t_{xx}$ are significant and the slope of the curve is a lot different than the unloading modulus. Therefore, different limits are more appropriate in this case, since the elastic region is extended up to approximately 20 MPa (within the first couple of cycles). By selecting a section between 5 - 20 MPa for all the

experimental curves, the true elastic modulus is calculated and presented in Table 4.3.

Moreover, the ultimate strength, σ^t_{xx}, and strain at ultimate strength, ϵ^t_{xx}, are determined from the maximum stress value in every experiment and the corresponding strain. For the determination of the proportionality limit, the "*deviation from the linearity method*" is used. With this method, the proportionality limit is selected as the stress value, σ_i, at which there is a 10% deviation from the stress calculated from the elastic relation $\sigma_i = E\epsilon_i$. The equation used is given by

$$\%dev = 100\left[\frac{(E\epsilon_i) - \sigma_i}{\sigma_i}\right] \tag{4.1}$$

where σ_i, ϵ_i and E are the i^{th} stress and strain of the curve and modulus of elasticity, respectively. Therefore, the stress, $\sigma^{t,0}_{xx}$, and strain, $\epsilon^{t,0}_{xx}$, at the proportionality limit are presented in Table 4.3.

Elastic properties				
Loading angle	$E^t_{xx} = E^t_{yy}$ [GPa]		$E^c_{xx} = E^c_{yy}$ [GPa]	
0^o	73.39 ± 1.41		68.57 ± 3.14	
30^o	40.53 ± 5.27		19.09 ± 0.65	
45^o	34.56 ± 4.31		16.27 ± 0.56	
Strength properties				
	Stress [MPa]	Strain [%]	Stress [MPa]	Strain [%]
Tensile - 0^o	$\sigma^t_{xx} = \sigma^t_{yy}$	$\epsilon^t_{xx} = \epsilon^t_{yy}$	$\sigma^{t,0}_{xx} = \sigma^{t,0}_{yy}$	$\epsilon^{t,0}_{xx} = \epsilon^{t,0}_{yy}$
	96.87 ± 7.29	0.21 ± 0.02	14.65 ± 2.75	0.02 ± 0.01
Compression - 0^o	$\sigma^c_{xx} = \sigma^c_{yy}$	$\epsilon^c_{xx} = \epsilon^c_{yy}$	$\sigma^{c,0}_{xx} = \sigma^{c,0}_{yy}$	$\epsilon^{c,0}_{xx} = \epsilon^{c,0}_{yy}$
	192.85 ± 32.49	0.30 ± 0.04	185.86 ± 47.84	0.27 ± 0.06
Tensile - 30^o	$\sigma^t_{xx} = \sigma^t_{yy}$	$\epsilon^t_{xx} = \epsilon^t_{yy}$	$\sigma^{t,0}_{xx} = \sigma^{t,0}_{yy}$	$\epsilon^{t,0}_{xx} = \epsilon^{t,0}_{yy}$
	92.14 ± 1.80	0.84 ± 0.05	16.86 ± 2.76	0.05 ± 0.02
Compression - 30^o	$\sigma^c_{xx} = \sigma^c_{yy}$	$\epsilon^c_{xx} = \epsilon^c_{yy}$	$\sigma^{c,0}_{xx} = \sigma^{c,0}_{yy}$	$\epsilon^{c,0}_{xx} = \epsilon^{c,0}_{yy}$
	131.43 ± 8.22	0.78 ± 0.05	109.84 ± 10.49	0.58 ± 0.06
Tensile - 45^o	$\sigma^t_{xx} = \sigma^t_{yy}$	$\epsilon^t_{xx} = \epsilon^t_{yy}$	$\sigma^{t,0}_{xx} = \sigma^{t,0}_{yy}$	$\epsilon^{t,0}_{xx} = \epsilon^{t,0}_{yy}$
	88.40 ± 2.28	1.07 ± 0.10	13.56 ± 1.65	0.04 ± 0.01
Compression - 45^o	$\sigma^c_{xx} = \sigma^c_{yy}$	$\epsilon^c_{xx} = \epsilon^c_{yy}$	$\sigma^{c,0}_{xx} = \sigma^{c,0}_{yy}$	$\epsilon^{c,0}_{xx} = \epsilon^{c,0}_{yy}$
	121.04 ± 7.77	0.93 ± 0.06	96.70 ± 3.81	0.65 ± 0.04

Table 4.3: Mechanical properties that are obtained from the tensile and compression tests.

The strength is decreased as the fiber orientation moves from 0^o to 45^o for both tensile and compression cases. On the other hand, the strain is increased as the fiber orientation moves from 0^o to 45^o for both cases again. The strength of the material in compression is more than double for the case of 0^o. This is a direct consequence of the ceramic nature of the material. It is common for ceramics to present higher strength values in compression compared to tension. It should be noted that these values correspond to the ultimate material strength which in most cases is the same as the failure strength. Only for the cases of 30^o and 45^o in compression,

the material does not fail at the ultimate strength. Moreover, for the compression tests of 0^o the stress-strain curve is almost entirely linear and the curves present some small fluctuations. So, determining the proportionality limit, in this case, is not appropriate since it is difficult to determine whether or not the material exhibits a non-linear regime. A representative stress-strain curve for every test is presented in Figure 4.23 where the complete material behavior can be seen.

Information about the damage in the material is obtained from the cyclic tensile curves. The unloading modulus is determined for every loading and unloading cycle and the damage is calculated from (3.27). Also, the evolution of damage for the on- and off-axis tensile tests is presented in Figure 4.24. Damage is evolving faster for the off-axis tests. It should be mentioned that the plot presents the evolution of damage in the global coordinate system. Finally, the degradation of Young's modulus is plotted, since the damaged modulus is calculated from the cyclic loading test curves (Figure 4.25). The degradation of the modulus follows the inverse evolution of damage. From this plot, the true Young modulus is more obvious and agrees with the one presented in Table 4.3.

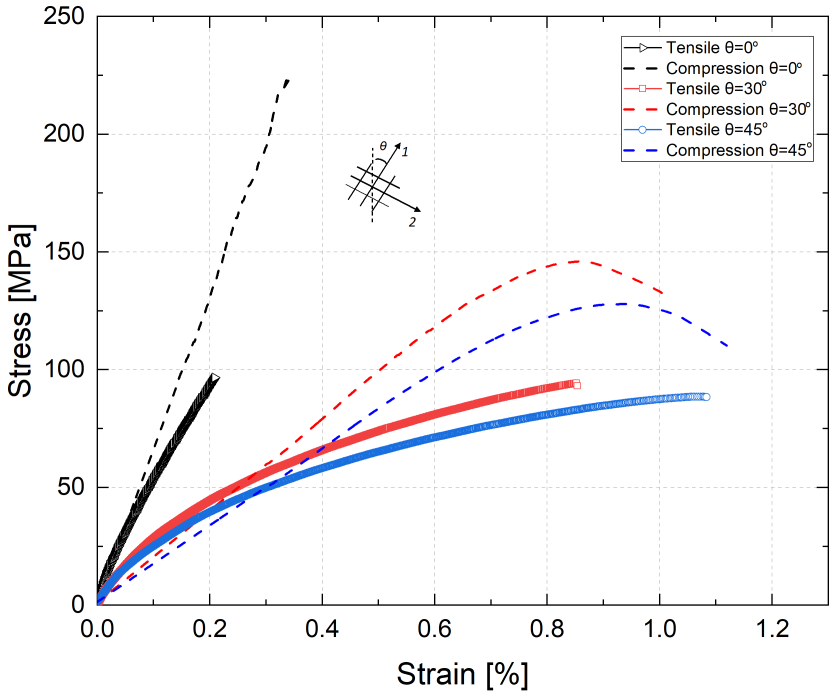

Figure 4.23: Stress-strain curves of C/C-SiC for the on- and off-axis cases in tension and compression.

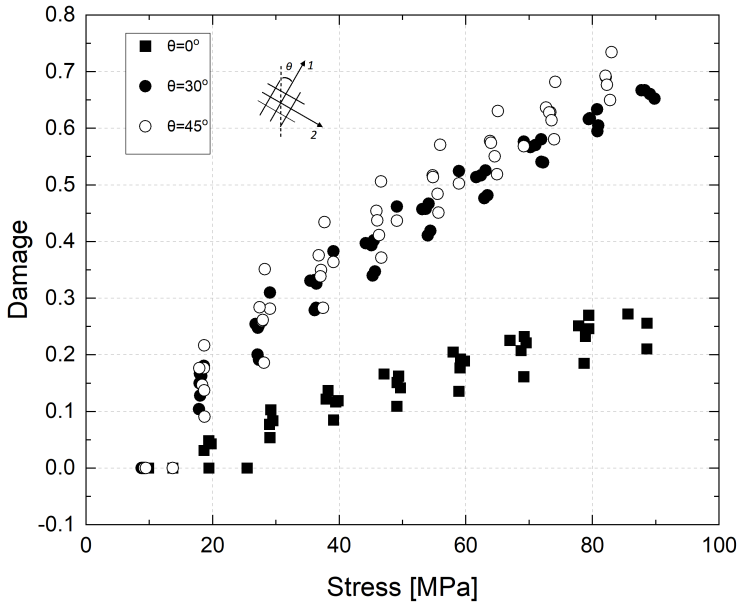

Figure 4.24: Evolution of the damage variables (global coordinate system) in tension for the on- and off-axis tests.

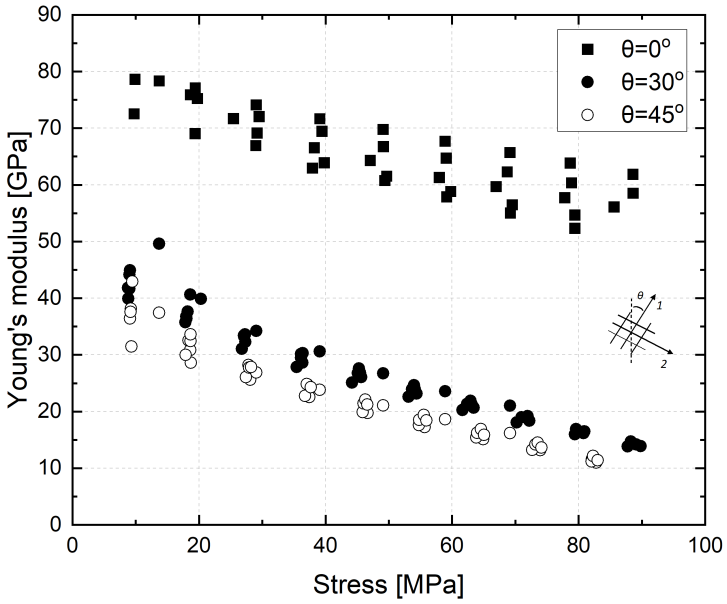

Figure 4.25: Degradation of the Young modulus with stress for the on- and off-axis tensile tests.

5

Identification of parameters and results

In Chapters 3 and 4 the computational model and data from the mechanical tests were presented. In this Chapter, the unknown variables and material parameters of the model are presented. Some of these parameters are directly obtained from the experiments while others need to be obtained indirectly from the experimental data. An optimization procedure, to determine the material parameters and the final results are presented in this chapter. First, the Bayesian optimization algorithm is discussed. Next, all the parameters of the model and the approach to optimize each one of them are presented. Finally, the results are compared to the experimental data and discussed.

5.1. Bayesian optimization

A Bayesian optimization algorithm is used in this study to optimize the various parameters. Bayesian optimization is a powerful and effective approach for optimizing black-box functions that are complex, expensive, or noisy. It is a method for finding the minimum or maximum of a function when only noisy, indirect observations of the function are available. It is based on Bayesian probability theory, which allows for building a probabilistic model of the function that is being optimized. This model is used to sequentially select the next point to evaluate in a way that maximizes the expected improvement in the function value, in order to find the global maximum or minimum of the function. Bayesian optimization can be applied to a wide range of problems, including hyperparameter tuning in machine learning algorithms, global optimization of complex engineering systems, and optimization of complex simulation models. It has several advantages over other optimization methods, such as the ability to handle noisy or expensive functions and to incorporate prior knowledge or constraints into the optimization process.

One of the key challenges in Bayesian optimization is constructing the probabilistic model of the function that is being optimized. This typically involves selecting a suitable family of probability distributions, such as Gaussian processes, and using Bayesian inference to estimate the parameters of the model based on the data that has been collected so far. Gaussian processes are a powerful probabilistic model that is used to estimate the unknown function by using only a few evaluations of the function. The advantage of using Gaussian processes is that they provide a distribution over possible functions, rather than a point estimate. This allows to balance exploration and exploitation when selecting the next point to evaluate, which can improve the convergence rate of the optimization algorithm. The quality of the model is

critical to the success of the optimization, as it determines how well the optimizer can explore the space of possible solutions and identify the global optimum.

One of the main advantages of Bayesian optimization is that it can handle constraints on the input space and noisy, expensive, or multi-objective functions. This makes it a popular choice for optimizing the parameters of material models with a large number of parameters, where the objective function is often expensive to evaluate and the search space is typically large and complex.

A Python library for Bayesian optimization is the scikit-optimize, or skopt. The library uses Gaussian processes to model the unknown function. To use skopt, first an objective function, which needs to be to be minimized (or maximized), should be defined together with the bounds on the input search space. One of the optimization algorithms provided by skopt to find the minimum (or maximum) of the function needs to be selected. Skopt also provides tools for visualizing the optimization process and evaluating the performance of different optimization algorithms. It also provides utilities for searching the space of possible parameters in a parallel and efficient way, as well as tools for measuring and improving the performance of the optimization algorithms.

Since the developed model is a function of strains and predicts the corresponding stresses ($\boldsymbol{\sigma} = f(\boldsymbol{\epsilon})$), the objective function needs to be a function of the predicted stresses. Therefore, the objective function in this work is selected as

$$f = \sum_{i=1}^{i=n} |\sigma_i^{mono} - \sigma_{i,exp}^{mono}|^2 + \lambda \sum_{j=1}^{j=m} |\sigma_j^{cycl} - \sigma_{j,exp}^{cycl}|^2 \quad \text{with} \quad \lambda > 0 \tag{5.1}$$

where λ is a constant that is chosen accordingly so that the two loss terms are equal[1], $loss_1 = loss_2$, n and m are the numbers of experimental data for monotonic and cyclic tests, respectively. Moreover, $\sigma_{i,exp}^{mono}, \sigma_{j,exp}^{cycl}$ are the stress values obtained from the experiments and $\sigma_i^{mono}, \sigma_j^{cycl}$ are the stress values obtained from the model. This function is selected to include the data of both loading conditions, monotonic and cyclic. This way the optimized material parameters result in a model that predicts the material response for both these types of loading.

5.2. Identification of material parameters

There is a large number of parameters that affect the model and need to be identified. In particular, there are 28 parameters for the most general case of an orthotropic lamina. The complete set of parameters is given through the parameter vector ϕ,

$$\begin{aligned}\phi = [&E_{11}, E_{22}, v_{12}, G_{12}, A, n, H_1, H_2, F_{1t}^o, F_{1t}, F_{1c}^o, F_{1c}, F_6^o, F_6, \\ &F_{2t}^o, F_{2t}, F_{2c}^o, F_{2c}, A_{1t}, m_{1t}, A_{1c}, m_{1c}, A_{2t}, m_{2t}, A_{2c}, m_{2c}, \alpha_{66}, \beta_{66}]\end{aligned} \tag{5.2}$$

These parameters can be reduced to 19 since the investigated composite is produced with 2/2 twill weave fabric therefore the elastic, strength and damage properties, in the two principal material directions, are assumed to be the same. The ϕ vector becomes,

[1] The two loss terms should have the same order of magnitude so that the weights of both these terms are similar.

$$\phi = [E_{11}, v_{12}, G_{12}, A, n, H_1, H_2, F_{1t}^o, F_{1t}, F_{1c}^o, F_{1c}, F_6^o, F_6, A_{1t}, m_{1t}, A_{1c}, m_{1c}, \alpha_{66}, \beta_{66}] \quad (5.3)$$

Some of the remaining parameters are obtained directly from the experimental results, such as the proportionality limits and the ultimate strength values in tension and compression. The shear strength value is taken directly from the literature to be equal to $F_6 = 71.7$ [MPa] [55]. The shear strength can not be obtained from the current experimental data and the model's dependence on it is small to be included in the optimization procedure. Furthermore, the damage evolution parameters, A_{1t} and m_{1t}, are obtained directly from fitting the damage evolution curve to the experimental data. Some further assumptions are made, since the damage evolution parameters for compression (A_{1c}, m_{1c}) could not be obtained from the current cyclic compression data. Therefore, the A_{1c}, m_{1c} are assumed to be the same for compression as in tension ($A_{1t} = A_{1c}$ and $m_{1t} = m_{1c}$). Moreover, the elastic properties are obtained from a separate optimization procedure with the use of the rotation matrix (given in (3.13)) and the linear regime of the experimental curves. In the end, the number of parameters left is reduced to seven,

$$\phi = [A, n, H_1, H_2, F_6^o, \alpha_{66}, \beta_{66}] \quad (5.4)$$

These parameters are obtained from an optimization procedure based on (5.1) with the use of the experimental data and the stress prediction from the model. A Bayesian optimization algorithm is used to determine the parameters of (5.4). All the data from the tensile monotonic and cyclic tests are used. The reason that the data from the monotonic compression tests are not used is that the stress-stain curves present a smaller slope (elastic modulus) compared to the equivalent case in tension (see Table 4.3). This difference is a result of the testing approach and processing of the data and would cause a wrong estimation of the parameters. Therefore, the compression test data are used only to validate the model after the optimization procedure.

5.2.1. Optimization of elastic properties

The Bayesian optimization algorithm is firstly used to optimize the elastic properties and the stiffness matrix in the local coordinate system. The elastic modulus (E_{xx}) in the global coordinate system for the three test cases, is known. Therefore, the unknown parameters are the elastic properties (E_{11}, ν_{12}, G_{12}) in the local coordinate system. The stiffness matrix for the three tests ($\theta = 0^o, 30^o$ and 45^o) is calculated by rotating the stiffness matrix of the local coordinate system through (3.13). Given the strains as inputs, the stresses are predicted through the linear elastic constitutive equation, $\boldsymbol{\sigma} = \mathbb{Q}\ \boldsymbol{\epsilon}$. Therefore, the objective function used in this optimization algorithm is given by the first term of (5.1). Only the data from the tensile tests are used since the compression stress-strain curves present a smaller Young's modulus due to the way that the experiments were conducted. Furthermore, only the data that correspond to the linear regime of the monotonic stress-strain curves are used in this optimization procedure.

For the implementation of the Bayesian optimization algorithm in Python, the scikit-optimize library is used. Expected improvement (EI) is used as the acquisition function, 200 evaluations of the objective function and six random initialization points are used. The bounds of the uniform priors and the optimized elastic properties are presented in Table 5.1.

Elastic properties	Units	Min.	Max.	Opt.
$E_{11} = E_{22}$	[GPa]	40.0	80.0	64.121
v_{12}	[-]	0.01	0.02	0.0159
G_{12}	[GPa]	1.0	12.0	2.207

Table 5.1: Bounds and optimized values of the elastic properties obtained from the optimization procedure.

Moreover, the elastic properties as a function of the angle θ are presented in polar plots in Figure 5.1. The plots present the resulting curves from the different iterations and optimum values. The experimentally obtained Young modulus for the various loading directions is displayed in Figure 5.1 (a).

Overall, the optimized values predict the tensile Young modulus well but overpredict the compression modulus. If the compression data were to be used in the optimization scheme, the converged solution would underpredict the tensile and overpredict the compression modulus and the optimized values would not have any physical meaning (*e.g.*, $G_{12} \approx \nu_{12} \approx 0$).

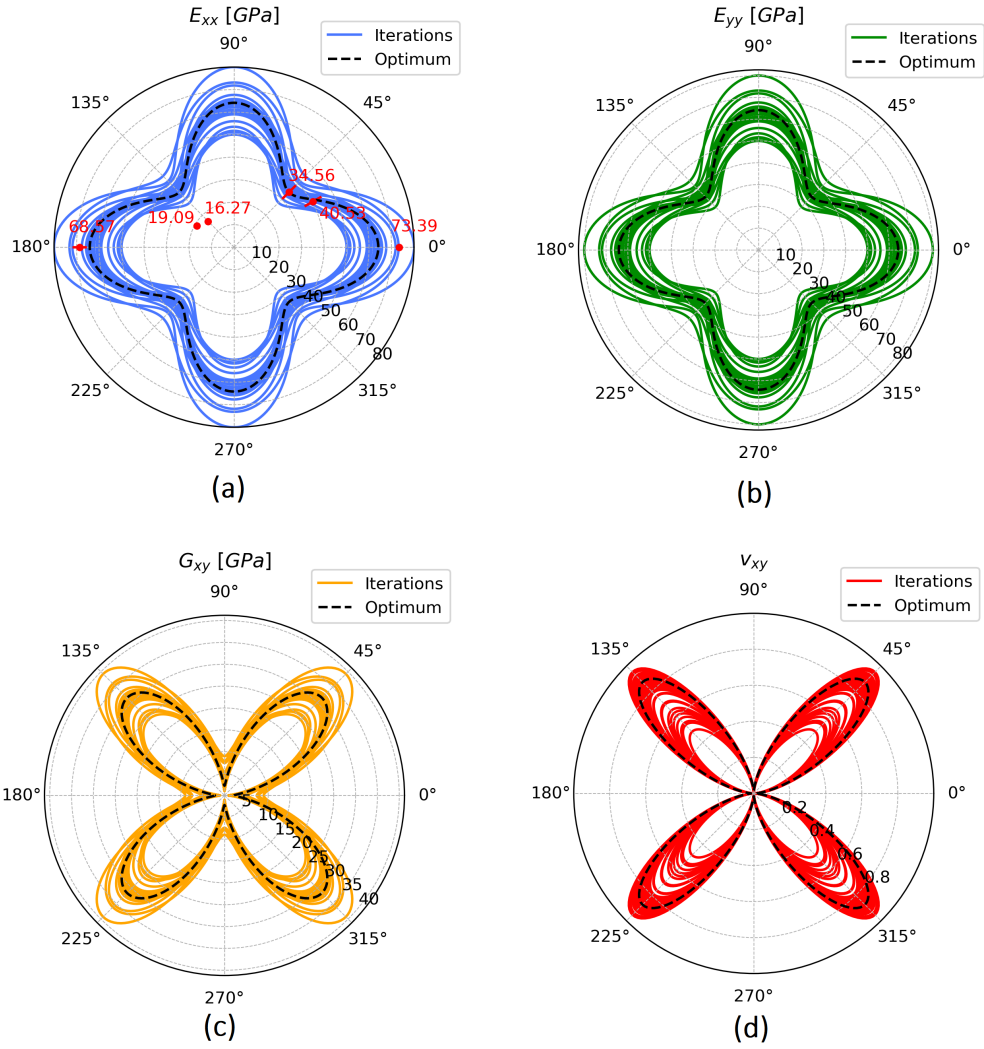

Figure 5.1: Elastic properties as a function of fiber orientation θ^o and the experimentally determined values of the E_{xx} modulus for $0^o, 30^o$ and 45^o. The curves corresponding to the different iterations (solid lines) are plotted together with those corresponding to the optimized properties (black dashed lines).

5.2.2. Damage parameters

The damage parameters, A_{1t} and m_{1t}, are determined through the fitting of the experimental data. Specifically, these two parameters refer to the damage along the 1-principal direction which is studied in Figure 4.24. Therefore, by fitting (3.24) in the experimental data the damage parameters are obtained. Only the data from the tensile tests of $\theta = 0^o$ can be used to obtain these damage parameters. The data of $\theta = 30^o$ and $\theta = 45^o$ correspond to the degradation of the stiffness matrix which is not aligned with the principal directions. Finally, the values of the damage variables obtained from fitting are $A_{1t} = 0.6747$ and $m_{1t} = 0.6514$.

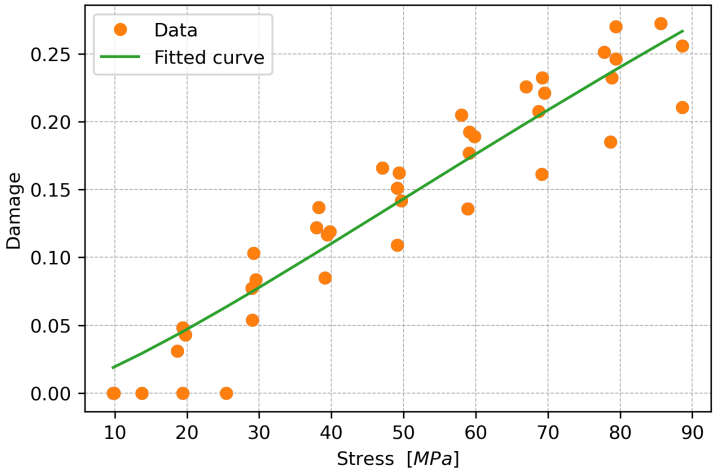

Figure 5.2: Damage evolution in the 1-principal direction and the fitted curve. The experimental data correspond to the tensile tests of $\theta = 0^o$.

5.2.3. Parameter optimization

The last part of the procedure for identifying the material parameters is the optimization of the remaining seven parameters (5.4). For that, Bayesian inference is applied and a seven-dimensional search space[2] is defined. A flow chart of the optimization algorithm is shown in Figure 5.3. The algorithm starts with defining the search space and its bounds. Uniform priors are assumed for every parameter and the bounds of these priors are shown in Table 5.2. Expected improvement (EI) is used as the acquisition function, 500 evaluations of the objective function and 15 random initialization points are used. The *gp_minimize()* function of scikit-optimize is called and predicts a set of values for every entry of the search space. These values are separated into six different parameters. Next, the dataset is loaded and the monotonic and cyclic strain and stress values are separated and organized in four different arrays, each for the strains and stresses of monotonic and cyclic tests. Next, the two loss terms of f are calculated separately and the overall value of f is calculated after λ is multiplied with the second term. For the determination of λ, the order of magnitude of the two loss terms is checked and eventually, $\lambda = 5 \times 10^{-1}$ is selected (see Appendix D). The constitutive model described in Chapter 3 (Section 3.3) is used as a function here to predict the stress values from the input strains but the failure criterion for checking if the final failure occurred, is deactivated. Equation (5.1) is used as the objective function, f, so both data from monotonic and cyclic loading tests are used. Finally, the value of the objective function is returned and the procedure is repeated with a different set of predictions until the maximum number of evaluations is reached. It should be noted once again that the optimization of these material parameters is performed on the data of tensile tests for the reasons mentioned before. Moreover, in the

[2]The domain of the function to be optimized.

optimization algorithm, the stresses and elastic properties are given in GPa so all the other parameters are expressed in the appropriate units for consistency. The optimized values for the material parameters are presented in Table 5.2.

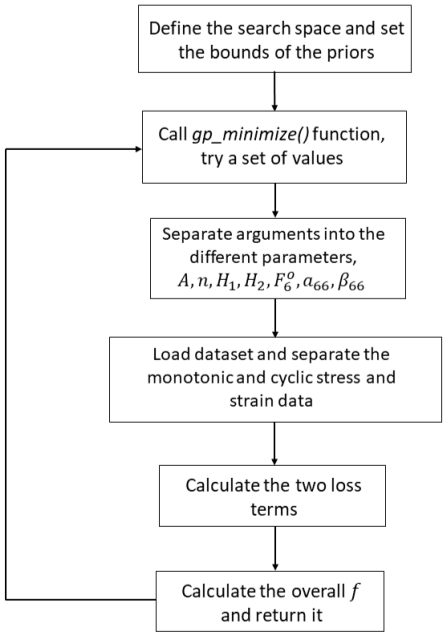

Figure 5.3: Flow chart of the algorithm in Python used for the optimization of the material parameters.

Parameter	Units	Min.	Max.	Opt.
A	[MPa^{-n}]	10^{-10}	10^{-7}	4.2808×10^{-8}
n	[-]	0.001	1.0	0.5217
H_1	[GPa]	0.001	1.0	0.3271
H_2	[-]	10^3	10^8	59403.7563
F_6^o	[GPa]	1.0	40.0	6.5785
α_{66}	[-]	0.1	1.0	0.74259
β_{66}	[-]	0.1	1.0	0.49651

Table 5.2: Bounds of the uniform priors used in the optimization and the optimized values of the material parameters.

Initial validation of the units and the magnitude of values mentioned in Table 5.2 is performed by checking the magnitude of key parameters such as plastic strain, back stress and stresses in the principal material directions. The case of the monotonic tensile test with $\theta = 45^o$ is selected as an example. In this case, the plastic strain predicted at the point of ultimate strength by this set of values is in the order of 10^{-1} [%], the σ_{11} in the local coordinate system is ≈ 80 [MPa] and the $\sigma_{11}^{back} \approx 0.60$ [MPa]. Further verification of the optimized values is presented in Section 5.3 where experimental plots are directly compared to the predictions of the model.

5.3. Results and discussion

To validate the results and the optimization procedure, the predictions from the computational model are directly compared to the experimental results. First, the tensile and compression stress-strain curves are presented in Figures 5.4 and 5.5. For the construction of the predicted curves, the experimental strains are used as inputs and the stresses are predicted from the model. The predicted and the corresponding experimental curves are presented together. Moreover, the final failure criterion is deactivated in this case. The predicted tensile stress-strain curves are close to the experimental ones. A minor deviation is observed for the case of $\theta = 45^o$ where the shear stresses are maximum.

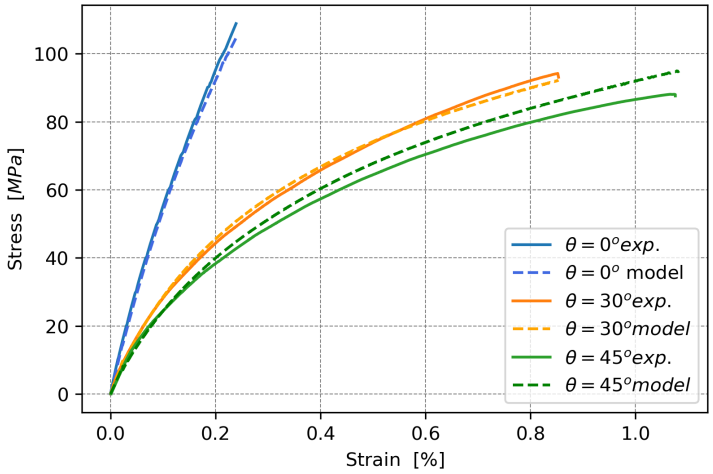

Figure 5.4: Comparison of the theoretically predicted and experimentally observed tensile stress–strain curves of C/C-SiC. The optimized values of Table 5.2 were used to predict the theoretical curves.

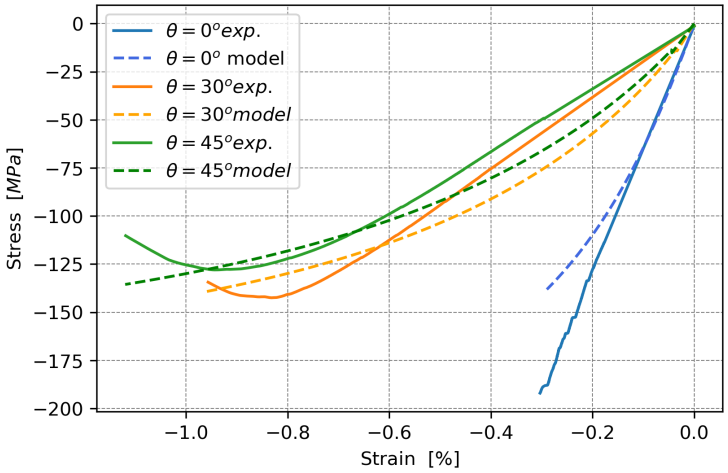

Figure 5.5: Comparison of the theoretically predicted and experimentally observed compression stress–strain curves of C/C-SiC. The optimized values of Table 5.2 were used to predict the theoretical curves.

On the other hand, the compression test data are used for further validation of the model. These data are not used in the optimization procedure to tune the parameters due to the difference in Young modulus between the model and experiment. To obtain the curves presented in Figure 5.5 the proportionality limit in compression is assumed to be the same as in tension, $F^o_{1c} = F^o_{1t}$. This assumption is made since the compression curve for $\theta = 0^o$ is linear

and the proportionality limit can not be predicted correctly. Moreover, the cyclic compression test curves show that plastic deformation is present at small force values. If a proportionality limit close to the ultimate strength were to be used, then due to the extended area of the yield function in the third quadrant (Tsai-Wu criterion), the material would yield at large stress values.

Except in the case of $\theta = 0^o$, the model gives reasonably close results in compression as well. For $\theta = 0^o$ the assumption leads to a difference in the predicted stress close to the ultimate strength point. For the other two cases, differences in the initial slope are observed since the Young modulus in the model is different than the experimental one. Moreover, the model does not include a softening detection and prediction feature so a deviation from the experiment is observed in the softening regime.

To compare the damage evolution prediction of the model, a direct comparison between the experimentally and theoretically obtained damaged Young modulus is presented in Figure 5.6. The evolution of damage in the model follows closely the experimental values in all three cases. The deviation observed in the case of $\theta = 0^o$ is due to the difference in the initial (undamaged) Young modulus ($E_{11}^{opt} = 64.12$ [GPa] compared to $E_{11}^{exp} = 73.39$ [GPa]). It is also confirmed that the damage coupling functions lead to a good prediction of the damage evolution in the cases of $\theta = 30^o$ and $\theta = 45^o$ where the shear stresses are higher.

Another feature of the model is that it predicts the material response under cyclic loading. This feature is compared to the experimentally obtained curves in Figure 5.7. The results are reasonably close but there are some areas with some deviation. The unloading modulus (unloading slope) is slightly smaller than the experimental one, especially in the case of $\theta = 0^o$. This is caused by the deviation of the initial Young modulus from the experimental ($E_{11}^{opt} < E_{11}^{exp}$), which is apparent in Figure 5.6. Also, the stress at the lowest point of the cycle is different from the experiment. This is affected by the hardening parameters and their values. In addition, under reloading, the point where the material enters again the hardening regime is approximated well and so is the envelope stress-strain curve.

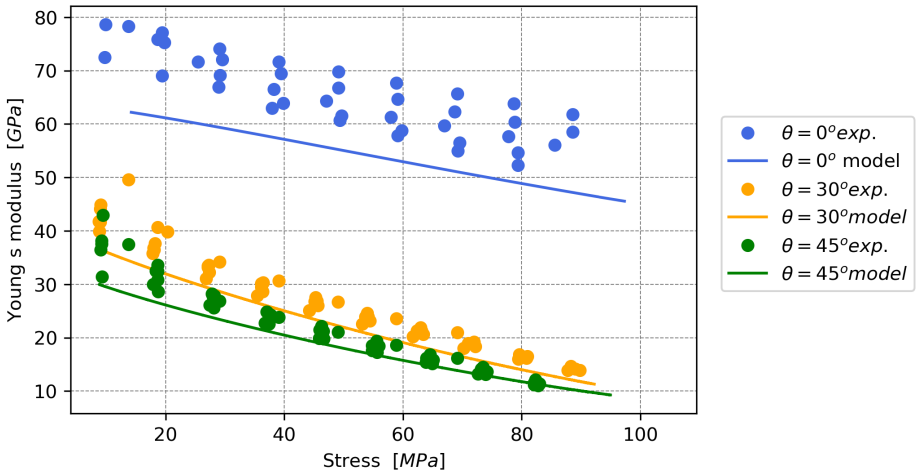

Figure 5.6: Degradation of Young modulus with stress in the three different tensile cases. The solid lines are the prediction of the model and the dots are the experimental observations.

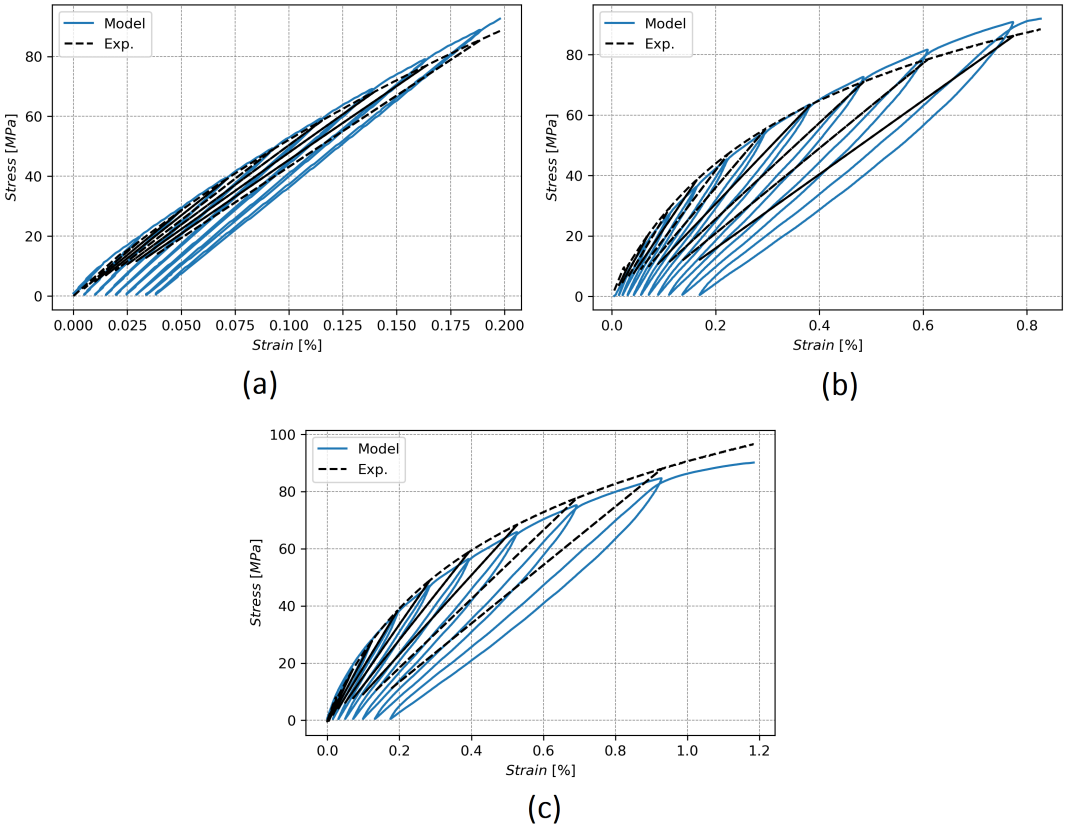

Figure 5.7: Predicted and experimental stress-strain curves under cyclic tensile loading.

Finally, the ability of the model to predict the final material failure is studied. A comparison between the theoretical predictions and experimental results for the tensile and compression cases of $\theta = 0^o, 30^o$ and 45^o is presented in Figures 5.8 and 5.9.

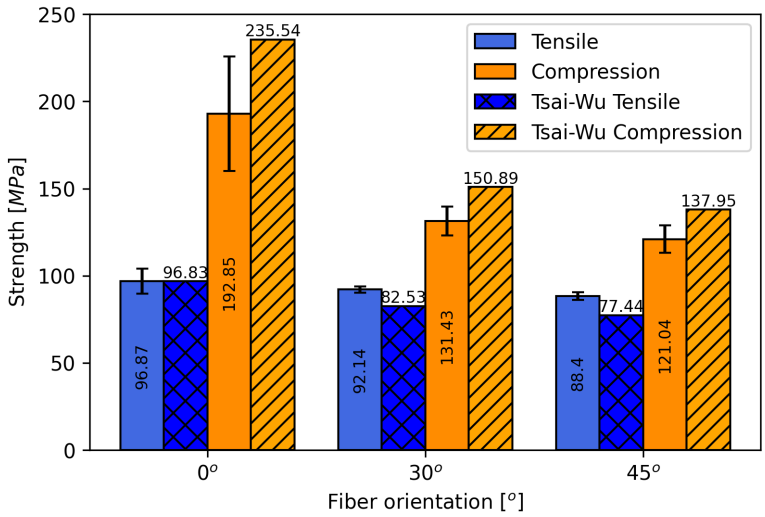

Figure 5.8: Comparison of the experimentally obtained and theoretically predicted tensile and compression strength values for the different fiber orientations.

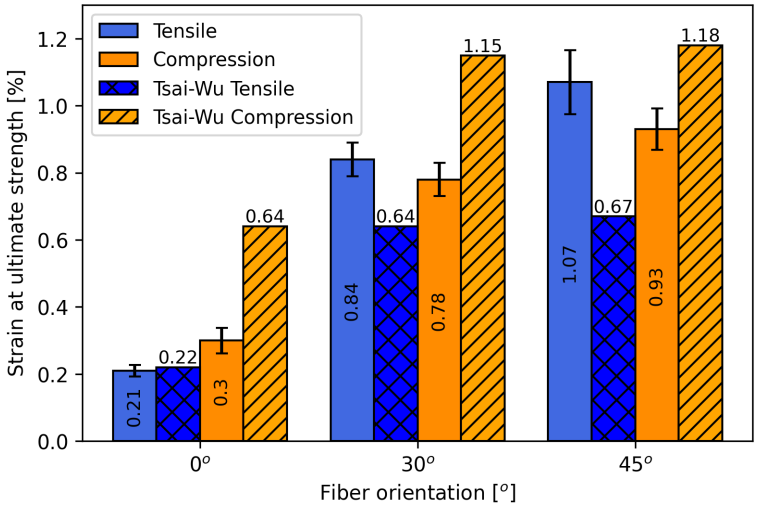

Figure 5.9: Comparison of the experimentally obtained and theoretically predicted tensile and compression strain at the strength for the different fiber orientations.

As most reports in the literature suggest, the Tsai-Wu criterion in combination with damage evolution can predict accurately the ultimate tensile strength of CMCs and therefore of C/C-SiC. The tensile strength when fibers are oriented at 30^o and 45^o is underpredicted slightly but it is reasonably close to the experimental strength. Some deviation is observed for the predicted strain at the ultimate tensile strength when the fibers are oriented at $\theta = 30^o$ and 45^o. On the other hand, the prediction for compressive strength and strain is not included in the literature. The Tsai-Wu criterion presents deviations in the predicted strength and strain in this case. Specifically, the predicted strength in compression is higher than the experimental in all three cases, especially for $\theta = 0^o$. The same phenomenon is observed for the predicted strain, the criterion overestimates the strain for all three cases. This happens due to the fact that the failure envelope is extended more in the third quadrant ($\sigma_{11} - \sigma_{22}$ plot). The anisotropy of the criterion is proven to be advantageous, compared to other criteria, for predicting the strength when shear stresses are developed, but overestimates the compression strength and strain.

6

Conclusions and recommendations

A 2-D elastoplastic constitutive model for the C/C-SiC CMC was presented and validated in this study. The damage-induced plasticity was modeled with a combination of plasticity and damage models. An elastic predictor-plastic corrector return mapping algorithm was used to calculate the evolution of plastic strains. Moreover, a series of mechanical tests that help in understanding the mechanical behavior of the material were presented. The different material parameters were addressed and identified based on the experimental data through the implementation of a Bayesian optimization algorithm. Finally, the predictions from the model and certain features of it were compared to experimental data and they were discussed.

6.1. Conclusions

The main conclusions of this study are as follows:

1. The constitutive model presented in this thesis successfully predicts the mechanical behavior of the 2/2 twill weave C/C-SiC under in-plane on- and off-axis loading. Both monotonic and cyclic loading conditions are predicted.

2. The combination of the Tsai-Wu criterion with the damage model can predict the tensile failure stress of C/C-SiC with reasonable accuracy while overpredicting the compression failure strength. Regarding the strain at the point of failure strength, the criterion underpredicts the strain in tension and overpredicts the strain in compression.

3. The overall tensile and compressive behavior of C/C-SiC is reported. Cyclic tensile and compression tests in different loading directions, relative to the fibers, are reported for the first time in literature.

4. The failure mechanisms of the material in the different loading directions are studied through SEM. Fiber bundle pull-out is mostly observed in the tensile specimens, while interlaminar and translaminar cracks are observed in the compression specimens.

5. Through the cyclic tensile tests, the damage evolution of the material in different directions is presented. The dissipated energy is larger for the case of $\theta = 30^o$ and $\theta = 45^o$ in both tension and compression.

6.2. Recommendations

As in every scientific research, there are certain limitations and restrictions that the current study presents. These limitations offer opportunities for further improving the current work. In

addition, there are certain ideas and directions that were developed during the course of this thesis and they are presented below.

Regarding the mechanical tests and the experimental data, there is a need to perform the compression tests with the use of strain gauges as a measuring device. An alternative could be to perform the tests and record the deformation using the crosshead but with the lower force limit over the non-linearity of the machine (instead of zero). This way the non-linearity, that could not be corrected in the current data, can be avoided. Then, the damage evolution parameters in compression can be corrected and a parameter optimization with all the test data can be performed again.

One thing that can improve further the accuracy of the current model is to perform the optimization based on more test data. By performing more tests under different loading directions, the optimization of the material parameters can be more accurate. Furthermore, the model can be extended to include more material parameters such as V_f, the content of the matrix constituents *etc.*. For example, the dependence of the elastic and failure properties from V_f can be studied by manufacturing and testing different specimens with different values of V_f.

Given the current computational framework, the model can be extended and adjusted to model other CMCs. Different plasticity and damage models can be included and a certain number of mechanical tests are required to make this possible. Furthermore, by making some assumptions the number of necessary tests can be reduced. For example, another woven CMC system can be modeled by selecting the appropriate hardening and damage models, conducting cyclic tensile and compression tests at $\theta = 0^o$ and $\theta = 45^o$ and with the use of Bayesian optimization, optimize the rest of the material parameters.

Finally, the model can be extended to account for the 3-D elastoplastic material response. A similar approach followed by Gupta et al. [21] can be followed in this case. In particular, the stiffness matrix can be extended to its 3-D form (see (3.15)) and three more damage parameters (D_{33}, D_{44} and D_{55}) need to be introduced together with their evolution law. The potential function needs to be adjusted accordingly.

The model can be translated to be used in a numerical scheme such as in finite element analysis (*e.g.*, Abaqus) as a user-defined subroutine (VUMAT). It can be further validated by comparing the results from simulations and real-life experiments on more complex structures.

A

Constitutive model

Additional information about the constitutive model are provided in this chapter.

A.1. Classical laminate theory

In this section, the Classical laminate theory is explained. The CLT is used to predict the behavior of the whole laminate. The following assumptions are made [14], which are based on the Kirchhoff hypothesis:

1. Each ply is orthotropic and quasi-homogeneous
2. The thickness of the plies is small and the other two dimensions are much larger than the thickness and the plies are loaded in plane stress condition.
3. The theory is valid for continuous through the thickness displacements that are small compared to the thickness of the laminate.
4. The in-plane axial and lateral displacements are a linear function of z to the thickness direction.
5. Plane sections that are initially normal to the mid-plane remain normal to the mid-plane after deformation.
6. The stress-strain relations vary linearly.
7. Transverse normal to the mid-plane is not extensible, therefore $\epsilon_z = 0$.

The stress-strain relation in the local coordinate system (material axes of the k^{th} UD-ply) is given by

$$\begin{bmatrix} \sigma_{11} \\ \sigma_{22} \\ \sigma_{12} \end{bmatrix}_k = \begin{bmatrix} Q_{11} & Q_{12} & 0 \\ Q_{21} & Q_{22} & 0 \\ 0 & 0 & Q_{66} \end{bmatrix}_k \begin{bmatrix} \epsilon_{11} \\ \epsilon_{22} \\ \epsilon_{12} \end{bmatrix}_k \tag{A.1}$$

The stress-strain relation in the global coordinate system of the laminate is

$$\begin{bmatrix} \sigma_{xx} \\ \sigma_{yy} \\ \sigma_{xy} \end{bmatrix}_k = \begin{bmatrix} Q_{xx} & Q_{xy} & Q_{xs} \\ Q_{yx} & Q_{yy} & Q_{xy} \\ Q_{sx} & Q_{sy} & Q_{ss} \end{bmatrix}_k \begin{bmatrix} \epsilon_{xx} \\ \epsilon_{yy} \\ \epsilon_{xy} \end{bmatrix}_k \tag{A.2}$$

where Q_{ij} is the reduced stiffness components that are given by

$$Q_{ij} = C_{ij} - \frac{C_{i3}C_{j3}}{C_{33}} \quad (i,j = 1,2,6) \tag{A.3}$$

due to the plane-stress assumption ($\sigma_{33} = \sigma_{23} = \sigma_{13} = 0$ therefore $\epsilon_{23} = \epsilon_{31} = 0$) in the orthotropic stress-strain relations.

From the definition of strains through the Classical Plate Theory the stresses in the global system for each ply are written as

$$\boldsymbol{\sigma}^k = \bar{\mathbb{Q}}^{(k)}\boldsymbol{\epsilon}^0 + \bar{\mathbb{Q}}^{(k)} z\boldsymbol{\kappa}^0 \tag{A.4}$$

where $\bar{Q}_{ij}^{(k)}$ is the reduced transformed stiffness matrix of the k^{th} ply and is given by

$$\bar{\mathbb{Q}}^{(k)} = \left(\boldsymbol{T}^{(k)}\right)^T \cdot \mathbb{Q}^{(k)} \cdot \boldsymbol{L} \cdot \boldsymbol{T}^{(k)} \cdot \boldsymbol{L}^T \tag{A.5}$$

with

$$\mathbb{Q} = \begin{bmatrix} \dfrac{E_1}{1-\nu_{12}\nu_{21}} & \dfrac{\nu_{12}E_2}{1-\nu_{12}\nu_{21}} & 0 \\ \dfrac{\nu_{12}E_2}{1-\nu_{12}\nu_{21}} & \dfrac{E_2}{1-\nu_{12}\nu_{21}} & 0 \\ 0 & 0 & G_{12} \end{bmatrix} \tag{A.6}$$

and $\boldsymbol{T}$ being the transformation and

$$\boldsymbol{L} = \begin{bmatrix} 1 & 0 & 0 \\ 0 & 1 & 0 \\ 0 & 0 & 2 \end{bmatrix} \tag{A.7}$$

The forces per unit length in a single ply are

$$\boldsymbol{N} = \begin{bmatrix} N_{xx} \\ N_{yy} \\ N_{xy} \end{bmatrix} = \begin{bmatrix} \int_{-z_{k-1}}^{z_k} \sigma_{xx}\, dz \\ \int_{-z_{k-1}}^{z_k} \sigma_{yy}\, dz \\ \int_{-z_{k-1}}^{z_k} \sigma_{xy}\, dz \end{bmatrix} \tag{A.8}$$

The bending moments per unit length in a single ply are

$$\boldsymbol{M} = \begin{bmatrix} M_{xx} \\ M_{yy} \\ M_{xy} \end{bmatrix} = \begin{bmatrix} \int_{-z_{k-1}}^{z_k} \sigma_{xx} z\, dz \\ \int_{-z_{k-1}}^{z_k} \sigma_{yy} z\, dz \\ \int_{-z_{k-1}}^{z_k} \sigma_{xy} z\, dz \end{bmatrix} \tag{A.9}$$

where z_{k-1} and z_k are the coordinates of the upper and lower surface of the k^{th} ply. From (A.4) the forces become

$$\boldsymbol{N} = \int_{-z_{k-1}}^{z_k} \left(\bar{\mathbb{Q}}^{(k)}\boldsymbol{\epsilon}^0 + \bar{\mathbb{Q}}^{(k)} z\boldsymbol{\kappa}^0\right) dz \tag{A.10}$$

In a similar way, the moments become

$$\boldsymbol{M} = \int_{-z_{k-1}}^{z_k} \left(\bar{\mathbb{Q}}^{(k)}\boldsymbol{\epsilon}^0 + \bar{\mathbb{Q}}^{(k)} z\boldsymbol{\kappa}^0\right) z\, dz \tag{A.11}$$

For the whole laminate structure, the forces and moments are the summations of the forces in every layer so

$$\begin{aligned} \boldsymbol{N} &= \sum_{k=1}^{N_{plies}} \int_{-z_{k-1}}^{z_k} \left(\bar{\mathbb{Q}}^{(k)} \boldsymbol{\epsilon}^0 + [\bar{\mathbb{Q}}]^{(k)} z \boldsymbol{\kappa}^0 \right) dz \\ &= \sum_{k=1}^{N_{plies}} \left(\bar{\mathbb{Q}}^{(k)} (z_k - z_{k-1}) \boldsymbol{\epsilon}^0 + \bar{\mathbb{Q}}^{(k)} \left(\frac{z_k^2 - z_{k-1}^2}{2} \right) \boldsymbol{\kappa}^0 \right) \end{aligned} \tag{A.12}$$

$$\boldsymbol{N} = \boldsymbol{A} \cdot \boldsymbol{\epsilon}^0 + \boldsymbol{B} \cdot \boldsymbol{\kappa}^0 \tag{A.13}$$

$$\begin{aligned} \boldsymbol{M} &= \sum_{k=1}^{N_{plies}} \int_{-z_{k-1}}^{z_k} \left(\bar{\mathbb{Q}}^{(k)} \boldsymbol{\epsilon}^0 + \bar{\mathbb{Q}}^{(k)} z \boldsymbol{\kappa}^0 \right) z \, dz \\ &= \sum_{k=1}^{N_{plies}} \left(\bar{\mathbb{Q}}^{(k)} \left(\frac{z_k^2 - z_{k-1}^2}{2} \right) \boldsymbol{\epsilon}^0 + \bar{\mathbb{Q}}^{(k)} \left(\frac{z_k^3 - z_{k-1}^3}{3} \right) \boldsymbol{\kappa}^0 \right) \end{aligned} \tag{A.14}$$

$$\boldsymbol{M} = \boldsymbol{B} \cdot \boldsymbol{\epsilon}^0 + \boldsymbol{D} \cdot \boldsymbol{\kappa}^0 \tag{A.15}$$

Therefore, from equations (A.13) and (A.15) the constitutive equation for the laminate is

$$\begin{bmatrix} N \\ M \end{bmatrix} = \begin{bmatrix} A & B \\ B & D \end{bmatrix} \begin{bmatrix} \varepsilon^0 \\ \kappa^0 \end{bmatrix} \tag{A.16}$$

So the ABD matrix is

$$\textbf{ABD} = \left[\begin{array}{ccc:ccc} A_{11} & A_{12} & A_{16} & B_{11} & B_{12} & B_{16} \\ A_{12} & A_{22} & A_{26} & B_{12} & B_{22} & B_{26} \\ A_{16} & A_{26} & A_{66} & B_{16} & B_{26} & B_{66} \\ \hdashline B_{11} & B_{12} & B_{16} & D_{11} & D_{12} & D_{16} \\ B_{12} & B_{22} & B_{26} & D_{12} & D_{22} & D_{26} \\ B_{16} & B_{26} & B_{66} & D_{16} & D_{26} & D_{66} \end{array}\right] \tag{A.17}$$

where

$$\begin{aligned} A_{ij} &= \sum_{k=1}^{N_{\text{plies}}} \left(\bar{Q}_{ij}^{(k)} \left(z_k - z_{k-1} \right) \right) \\ B_{ij} &= \sum_{k=1}^{N_{\text{plies}}} \frac{1}{2} \left(\bar{Q}_{ij}^{(k)} \left(z_k^2 - z_{k-1}^2 \right) \right) \\ D_{ij} &= \sum_{k=1}^{N_{\text{plies}}} \frac{1}{3} \left(\bar{Q}_{ij}^{(k)} \left(z_k^3 - z_{k-1}^3 \right) \right) \end{aligned} \tag{A.18}$$

A.2. Plasticity model

Analytical expressions about the quadratic and Tsai-Wu potential functions are presented here.

A.2.1. Quadratic potential function

The incremental plastic work per unit volume is given as

$$\dot{W}^p = \boldsymbol{\sigma}\, \dot{\boldsymbol{\epsilon}}^p \tag{A.19}$$

and by substituting equations (3.31) and (3.32) to (A.19)

$$\dot{W}^p = \sigma_{e11}\dot{\epsilon}^p_{11} + \sigma_{e22}\dot{\epsilon}^p_{22} + \sigma_{e12}\dot{\gamma}^p_{12} = 2g\dot{\lambda} \tag{A.20}$$

Let the equivalent stress be defined as

$$\overline{\sigma} = \sqrt{3g}. \tag{A.21}$$

The equivalent plastic strain can be defined as

$$\dot{W}^p = \boldsymbol{\sigma}\, \dot{\boldsymbol{\epsilon}}^p = \overline{\sigma}\, \dot{\overline{\epsilon}}^p \tag{A.22}$$

and from (A.20) and (A.21)

$$\dot{\overline{\epsilon}}^p = \frac{2}{3}\overline{\sigma}\dot{\lambda} \tag{A.23}$$

and

$$\dot{\lambda} = \frac{3}{2}\left(\frac{\dot{\overline{\epsilon}}^p}{\overline{\sigma}}\right)\left(\frac{\dot{\overline{\sigma}}}{\overline{\sigma}}\right) \tag{A.24}$$

From equations (3.31) and (3.32) the incremental plastic strains can be written as

$$\begin{bmatrix} \dot{\epsilon}^p_{11} \\ \dot{\epsilon}^p_{22} \\ \dot{\gamma}^p_{12} \end{bmatrix} = \begin{bmatrix} \alpha_{11} & \alpha_{12} & 0 \\ \alpha_{12} & \alpha_{22} & 0 \\ 0 & 0 & 2\alpha_{66} \end{bmatrix} \begin{bmatrix} \sigma_{e11} \\ \sigma_{e22} \\ \sigma_{e12} \end{bmatrix} \dot{\lambda} \tag{A.25}$$

Therefore, the $\alpha_{11}, \alpha_{22}, \alpha_{12}, \alpha_{66}$ and $\dot{\lambda}$ parameters need to determine in order for the plastic flow to be defined. For off-axis uniaxial tensile tests, the stresses in the principal material axes (local coordinate system) are given by (3.11) and (2.25). Substitution of (3.11) into (3.29) and (A.21) gives

$$\overline{\sigma} = h(\theta)\sigma_{xx} \tag{A.26}$$

where

$$h(\theta) = \sqrt{\frac{3}{2}(\alpha_{11}\cos^4\theta + \alpha_{22}\sin^4\theta + 2(\alpha_{12}+\alpha_{66})\sin^2\theta\cos^2\theta)} \tag{A.27}$$

For the strain transformation, (3.11) is used, therefore

$$\dot{\epsilon}^p_{xx} = \dot{\epsilon}^p_{11}\cos^2\theta + \dot{\epsilon}^p_{22}\sin^2_\theta - \dot{\gamma}^p_{12}\cos\theta\sin\theta \tag{A.28}$$

By substituting (A.25) and (3.11) into (A.28) the

$$\dot{\epsilon}^p_{xx} = \frac{2}{3}h^2(\theta)\sigma_{xx}\dot{\lambda} \tag{A.29}$$

is obtained. Or equivalently from (A.26)

$$\dot{\epsilon}^p_{xx} = \frac{2}{3}h^2(\theta)\overline{\sigma}\dot{\lambda} \tag{A.30}$$

By equating (A.23) and (A.30), the incremental equivalent strain is given by

$$\dot{\bar{\epsilon}}^p = \frac{\dot{\epsilon}^p_{xx}}{h(\theta)} \tag{A.31}$$

and if the loading is monotonic the above equation becomes

$$\bar{\epsilon}^p = \frac{\epsilon^p_{xx}}{h(\theta)} \tag{A.32}$$

This means that from the experimental σ_{xx} and ϵ^p_{xx}, the relation between $\bar{\sigma}$ and $\bar{\epsilon}^p$ can be obtained as well. Equations (A.26) and (A.32) give

$$\frac{\dot{\bar{\sigma}}}{\dot{\bar{\epsilon}}^p} = h^2(\theta)\frac{\dot{\sigma}_{xx}}{\dot{\epsilon}^p_{xx}} \tag{A.33}$$

and from (A.24)

$$\dot{\lambda} = \frac{3}{2}\frac{1}{h^2(\theta)}\left(\frac{\dot{\epsilon}_{xx}}{\dot{\sigma}_{xx}}\right)\left(\frac{\dot{\sigma}_{xx}}{\sigma_{xx}}\right) \tag{A.34}$$

For the case of 2/2 twill weave fabric

$$2g(\boldsymbol{\sigma}) = \alpha_{11}\sigma^2_{e11} + \alpha_{11}\sigma^2_{e22} + 2\alpha_{12}\sigma_{e11}\sigma_{e22} + 2\alpha_{66}\sigma^2_{12} \tag{A.35}$$

and

$$h(\theta) = \sqrt{\frac{3}{2}(\alpha_{11}\cos^4\theta + \alpha_{11}\sin^4\theta + 2(\alpha_{12}+\alpha_{66})\sin^2\theta\cos^2\theta)}. \tag{A.36}$$

A.2.2. Tsai-Wu potential function

For the Tsai-Wu-inspired potential function, some further equations are presented here. The derivatives of the yield function are given by

$$\begin{aligned}\frac{\partial f}{\partial \sigma_{e11}} &= f_1 + 2f_{11}\sigma_{e11} + 2f_{12}\sigma_{22}\\ \frac{\partial f}{\partial \sigma_{22}} &= f_2 + 2f_{22}\sigma_{e22} + 2f_{12}\sigma_{e11}\\ \frac{\partial f}{\partial \sigma_{e12}} &= 2f_{66}\sigma_{e12}\end{aligned} \tag{A.37}$$

Let the equivalent stress be defined as

$$\bar{\sigma} = g \tag{A.38}$$

and in the same manner, the equivalent plastic strain, in this case, is defined as

$$\dot{\bar{\epsilon}}^p = \dot{\lambda}\frac{(2g - \sigma_{e11}f_1 - \sigma_{e22}f_2)}{g} \tag{A.39}$$

B

Specimen preparation

In this section, all the extra information about specimen preparation is presented. In Figures, B.1 and B.2 pictures of the CFRP plate inside the mold that was used in the warm-press technique and the final CMC plate, are presented, respectively.

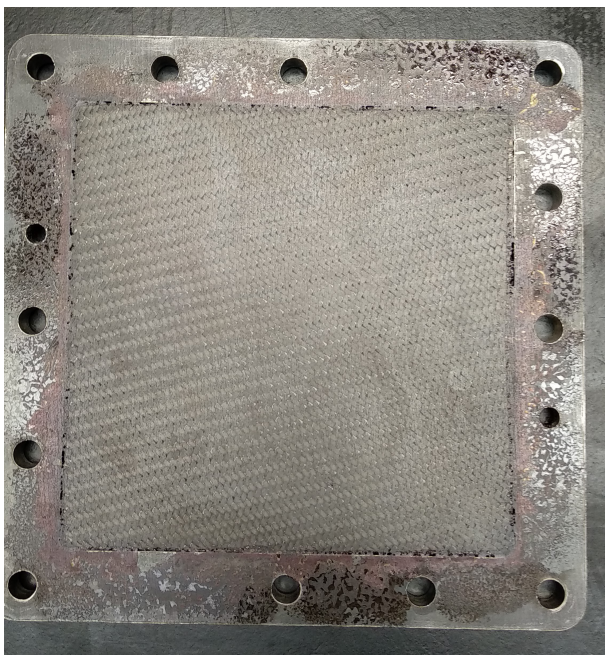

Figure B.1: CFRP plate inside the mold that was used in the warm-press process.

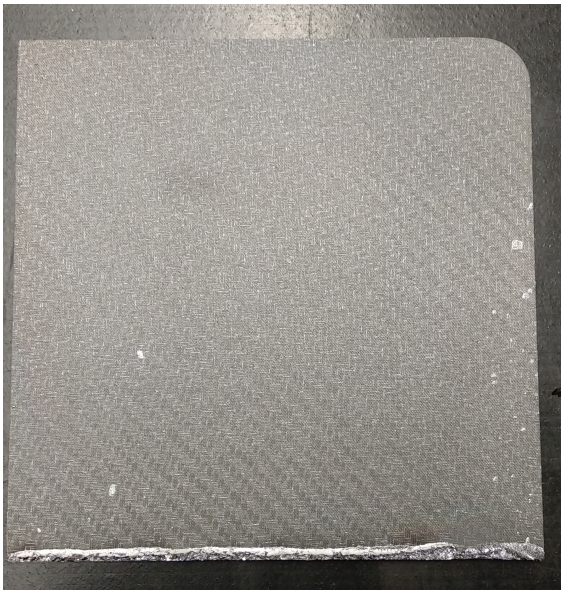

Figure B.2: One of the CMC plates that were used to prepare the test specimens.

Pictures of the final specimens before testing are presented in Figures B.3, B.4.

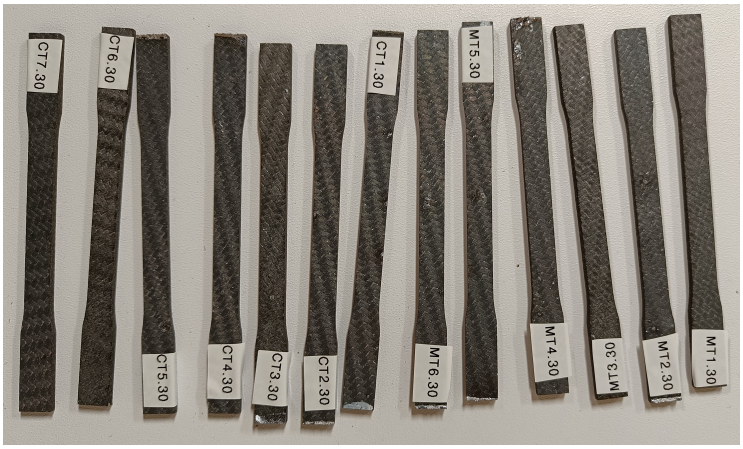

Figure B.3: Monotonic and cyclic tensile specimens with $\theta = 30^o$ before testing.

Tables B.1-B.11 present the dimensions of each specimen. Multiple measurements were taken to assure the minimization of error and to check compliance with the standards. The average values of the dimensions of each specimen are presented below.

Specimen	Average length (mm)	Average width (mm)	Average thickness (mm)	Cross-section (mm^2)
MT1-0	120.03	8.10	2.47	20.05
MT2-0	120.04	8.05	2.53	20.36
MT3-0	120.03	8.09	2.48	20.05
MT4-0	120.05	8.07	2.51	20.27
MT5-0	120.02	8.07	2.47	19.92
MT6-0	119.99	8.06	2.46	19.85

Table B.1: MT#-0 specimen dimensions.

Figure B.4: Tensile and compression specimens of 30^o before testing.

Specimen	Average length (mm)	Average width (mm)	Average thickness (mm)	Cross-section (mm^2)
MT1-30	120.11	8.24	2.69	22.14
MT2-30	120.02	8.06	2.73	22.02
MT3-30	120.07	8.04	2.74	22.00
MT4-30	120.05	8.14	2.71	22.06
MT5-30	120.03	8.10	2.73	22.10
MT6-30	120.02	8.09	2.73	22.05

Table B.2: MT#-30 specimen dimensions.

Specimen	Average length (mm)	Average width (mm)	Average thickness (mm)	Cross-section (mm^2)
MT1-45	119.96	8.04	2.69	21.60
MT2-45	119.96	8.00	2.71	21.65
MT3-45	119.91	8.00	2.70	21.57
MT4-45	119.97	8.05	2.70	21.73
MT5-45	120.04	8.07	2.69	21.69
MT6-45	120.02	8.10	2.72	22.01
MT7-45	119.99	8.04	2.66	21.40

Table B.3: MT#-45 specimen dimensions.

Specimen	Average length (mm)	Average width (mm)	Average thickness (mm)	Cross-section (mm^2)
CT1-0	120.04	8.08	2.50	20.22
CT2-0	120.00	8.11	2.46	19.92
CT3-0	120.00	7.98	2.56	20.42
CT4-0	120.04	8.13	2.46	19.97
CT5-0	120.03	8.05	2.48	19.98
CT6-0	120.03	8.11	2.47	20.00

Table B.4: CT#-0 specimen dimensions.

Specimen	Average length (mm)	Average width (mm)	Average thickness (mm)	Cross-section (mm^2)
CT1-30	120.04	8.08	2.74	22.15
CT2-30	120.01	8.11	2.72	22.02
CT3-30	120.08	8.10	2.72	22.03
CT4-30	120.05	8.08	2.73	22.03
CT5-30	120.00	8.05	2.71	21.84
CT6-30	120.00	8.05	2.72	21.87
CT7-30	120.06	8.10	2.65	21.45

Table B.5: CT#-30 specimen dimensions.

Specimen	Average length (mm)	Average width (mm)	Average thickness (mm)	Cross-section (mm^2)
CT1-45	119.97	8.04	2.65	21.26
CT2-45	120.02	8.03	2.66	21.39
CT3-45	119.91	8.03	2.68	21.53
CT4-45	120.02	8.04	2.66	21.38
CT5-45	119.98	8.03	2.65	21.30
CT6-45	119.94	8.03	2.64	21.17
CT7-45	119.99	8.04	2.66	21.40

Table B.6: CT#-45 specimen dimensions.

Specimen	Average length (mm)	Average width (mm)	Average thickness (mm)	Cross-section (mm^2)
MC1-0	25.03	10.06	3.29	33.07
MC2-0	25.02	10.05	3.31	33.27
MC3-0	25.06	10.04	3.27	32.87
MC4-0	25.06	10.05	3.24	32.50
MC5-0	25.07	10.02	3.28	32.88
MC6-0	25.02	10.07	3.25	32.71

Table B.7: MC#-0 specimen dimensions.

Specimen	Average length (mm)	Average width (mm)	Average thickness (mm)	Cross-section (mm^2)
MC1-30	25.06	10.06	2.78	28.00
MC2-30	25.05	10.10	2.74	27.64
MC3-30	25.08	10.10	2.78	28.04
MC4-30	25.08	10.04	2.81	28.18
MC5-30	25.04	10.10	2.75	27.77
MC6-30	25.07	10.09	2.76	27.87

Table B.8: MC#-30 specimen dimensions.

Specimen	Average length (mm)	Average width (mm)	Average thickness (mm)	Cross-section (mm^2)
MC1-45	25.00	10.04	2.78	27.89
MC2-45	25.01	10.07	2.77	27.86
MC3-45	25.00	10.08	2.73	27.48
MC4-45	25.03	10.03	2.74	27.51
MC5-45	25.00	10.20	2.72	27.76
MC6-45	24.96	10.00	2.74	27.35

Table B.9: MC#-45 specimen dimensions.

Specimen	Average length (mm)	Average width (mm)	Average thickness (mm)	Cross-section (mm^2)
CC1-0	25.08	10.06	3.24	32.62
CC2-0	25.06	10.04	3.27	32.78
CC3-0	25.02	10.03	3.21	32.21
CC4-0	25.06	10.09	3.25	32.73
CC5-0	25.09	10.03	3.27	32.83
CC6-0	25.05	10.01	3.21	32.12

Table B.10: CC#-0 specimen dimensions.

Specimen	Average length (mm)	Average width (mm)	Average thickness (mm)	Cross-section (mm^2)
CC1-30	25.10	10.03	2.81	28.21
CC2-30	25.09	10.09	2.77	27.93
CC3-30	25.06	10.05	2.79	28.04
CC4-30	25.05	10.07	2.76	27.73
CC5-30	25.06	10.13	2.73	27.67
CC6-30	25.06	10.12	2.77	28.00

Table B.11: CC#-30 specimen dimensions.

Specimen	Average length (mm)	Average width (mm)	Average thickness (mm)	Cross-section (mm^2)
CC1-45	25.02	10.07	2.71	27.27
CC2-45	25.00	10.04	2.75	27.56
CC3-45	25.01	10.07	2.70	27.18
CC4-45	25.04	10.04	2.76	27.74
CC5-45	25.03	10.07	2.77	27.91
CC6-45	25.03	10.01	2.74	27.42

Table B.12: CC#-45 specimen dimensions.

Finally, all the tested specimens are presented in Figure B.5.

Figure B.5: All the specimens after the tests.

C

Material characterization

C.1. Experimental set-up

Extra information regarding the mechanical tests is presented in this section. The Zwick machine with the wedged-type grips and the extensometer can be seen in Figure C.1. The compression set-up with a specimen placed inside the compression plates can be seen in Figure C.2.

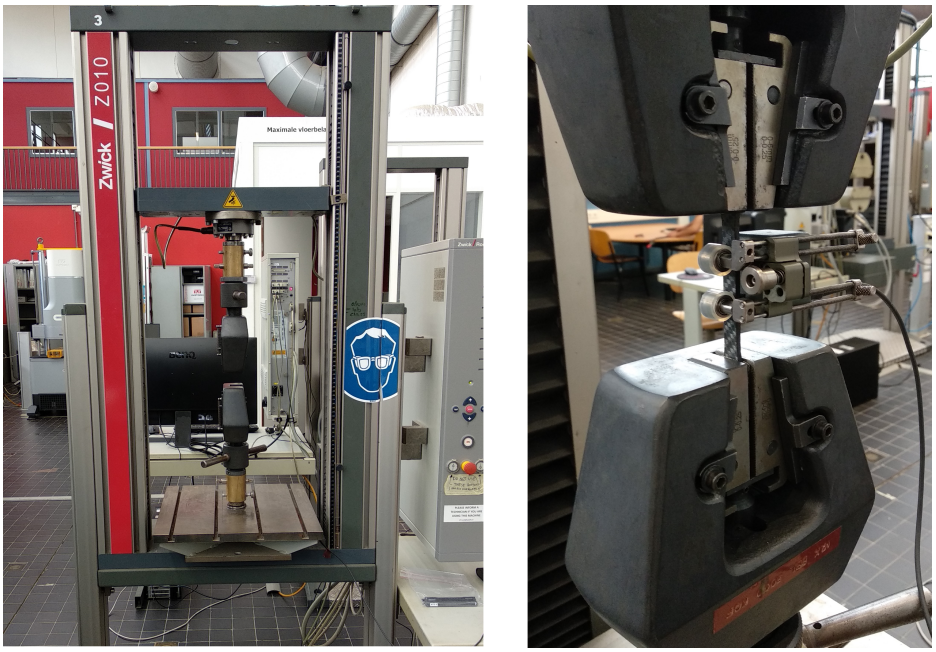

Figure C.1: Zwick/Roell Z010 machine and tensile set-up.

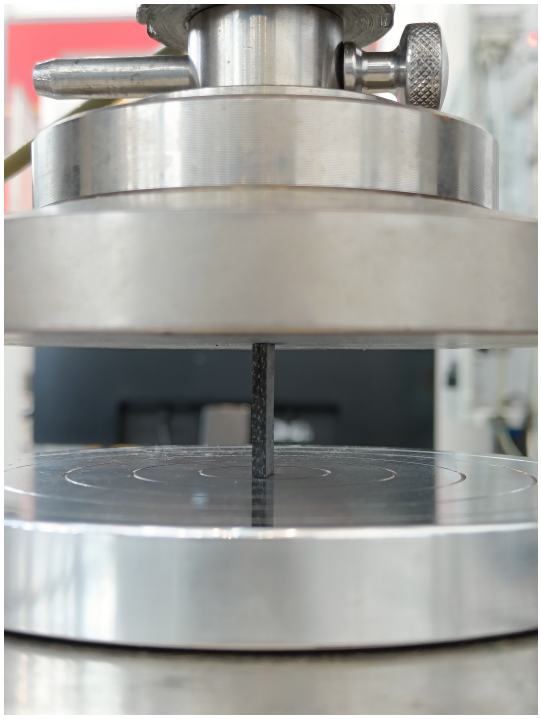

Figure C.2: Compression set-up.

Finally, pictures from a tensile and a compression specimen after testing are presented in Figures C.3 and C.4. In Figure C.3 the location of fracture is shown and it is located within the gauge length, which means that the test was accurate.

Figure C.3: Fractured tensile specimen after testing.

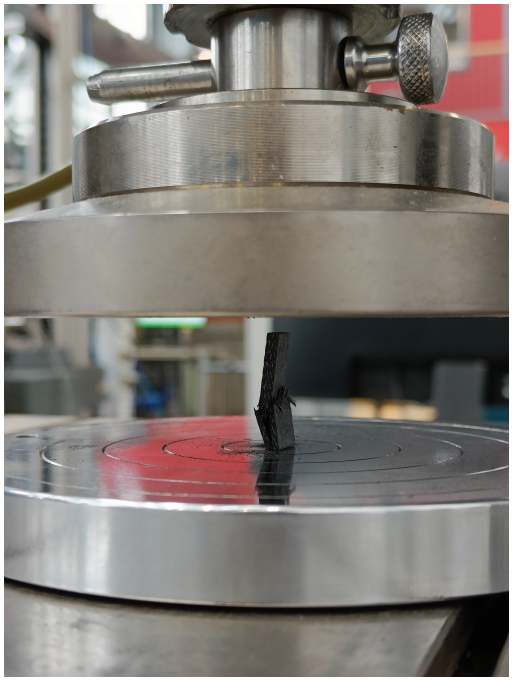

Figure C.4: Fractured compression specimen after testing.

The experimental set-up used for the compression test of the steel coupons is presented in Figure C.5. The set-up is exactly the same as the one used for the compression tests of the C/C-SiC specimens.

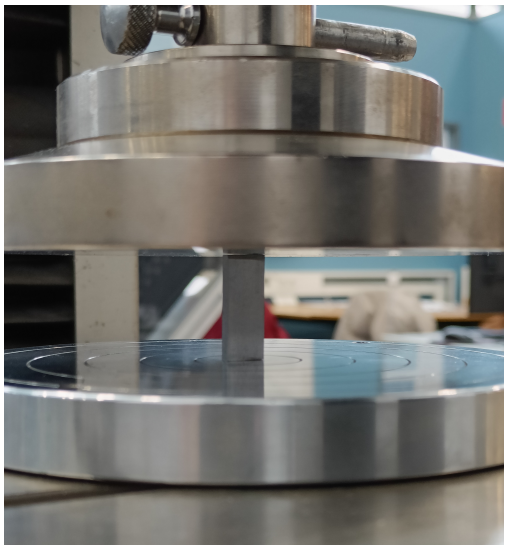

Figure C.5: Compression of steel coupon.

The calculated force-displacement curve of the experimental set-up is presented in Figure C.6.

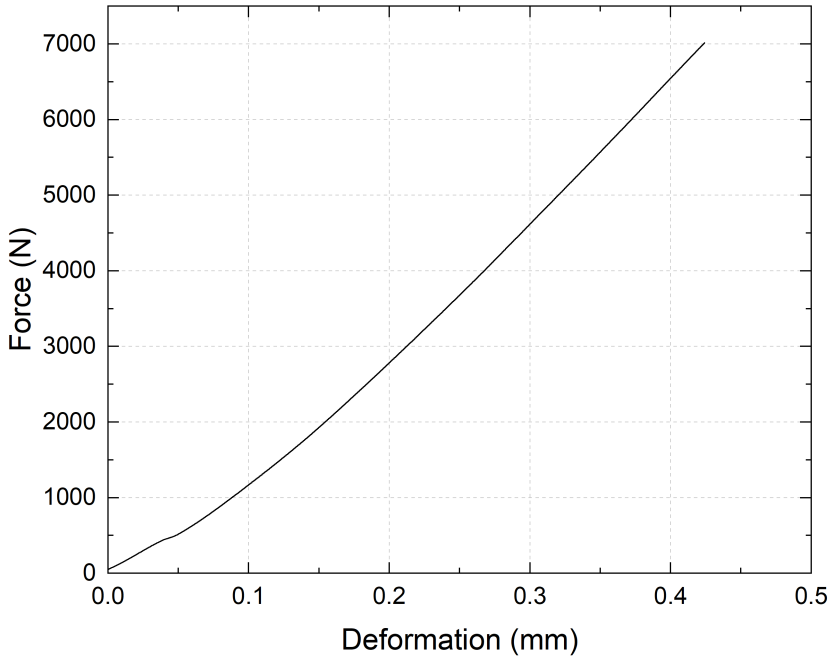

Figure C.6: Force-displacement curve of the testing machine.

C.2. Data processing

Regarding the processing of the data to obtain the material deformation, two procedures can be followed. The first one is to determine the slope of the linear part of the force and displacement curve shown in Figure C.6. Since the slope is known at this point, for each measurement of force in the raw data[1], the deformation of the experimental set-up can be calculated. This deformation needs to be subtracted from the corresponding total deformation. This way the force-displacement curve of the material is determined. The stress-strain curve can be calculated with the use of $\sigma = F/A$ and $\epsilon = e/L$. In case a small ”toe” regime is still present at small stresses, the linear regime of the plot can be extrapolated to correct the data according to the DIN and ASTM standards. This toe may be an artifact of the test specimen or test conditions and may not represent a property of the material. The curve can be corrected for this toe by extending the linear region of the curve to the zero stress point on the strain axis.

The second approach concerns the subtraction of the whole force-displacement curve of the testing set-up (Figure C.6) from the raw data of the specimens. The force and deformation values of the experimental set-up and the specimens were loaded in separate columns. The VLOOKUP() function was used to find the force value from the set-up’s data, which is closer to the one from the specimen’s data. Then the deformation of the set-up was subtracted from the equivalent deformation of the specimen’s data. The allowed difference between the force values was set to 1 N. The stress-strain curve was calculated similarly to the previous case. This procedure is the only way possible to process the data from the cyclic compression tests, especially at small force values (less than 1 kN).

C.3. Experimental results

In this Section, some of the experimental curves that were not presented in the main text, are presented here. Firstly, the cyclic tensile curves are presented in Figure C.7.

[1]Force-deformation data of each specimen measured via the cross-head of the machine

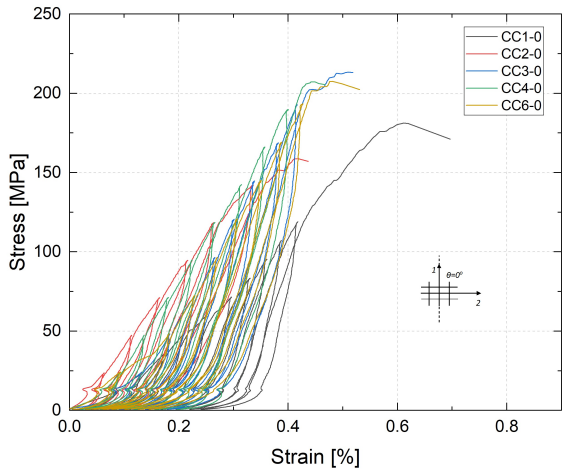

(a)

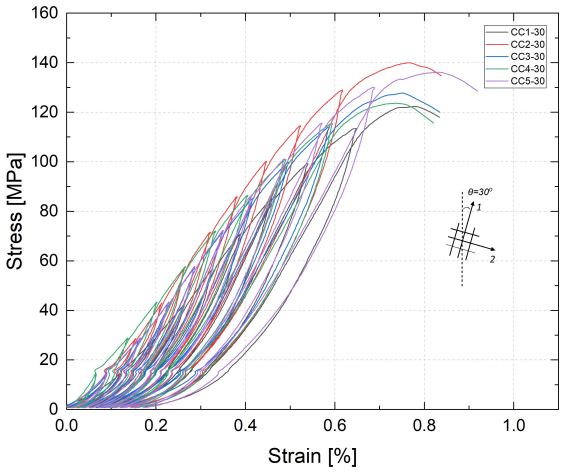

(b)

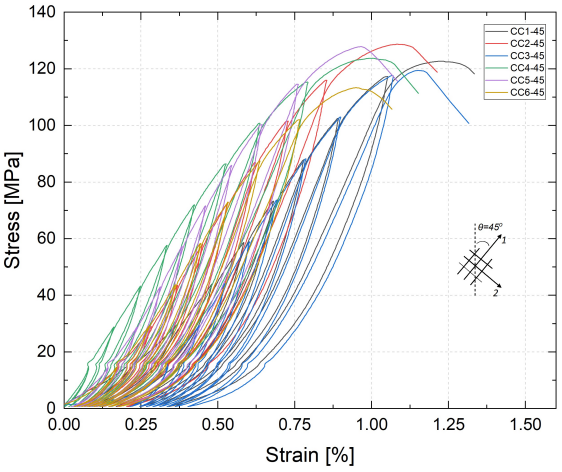

(c)

Figure C.7: Cyclic tensile stress-strain curves of C/C-SiC for (a) $\theta = 0^o$, (b) $\theta = 30^o$ and (c) $\theta = 45^o$.

The raw force-displacement curves of the specimens loaded with a monotonic compression load, the raw load-displacement and processed stress-strain curves of the cyclic com-

pression tests are presented in Figures C.8 and.

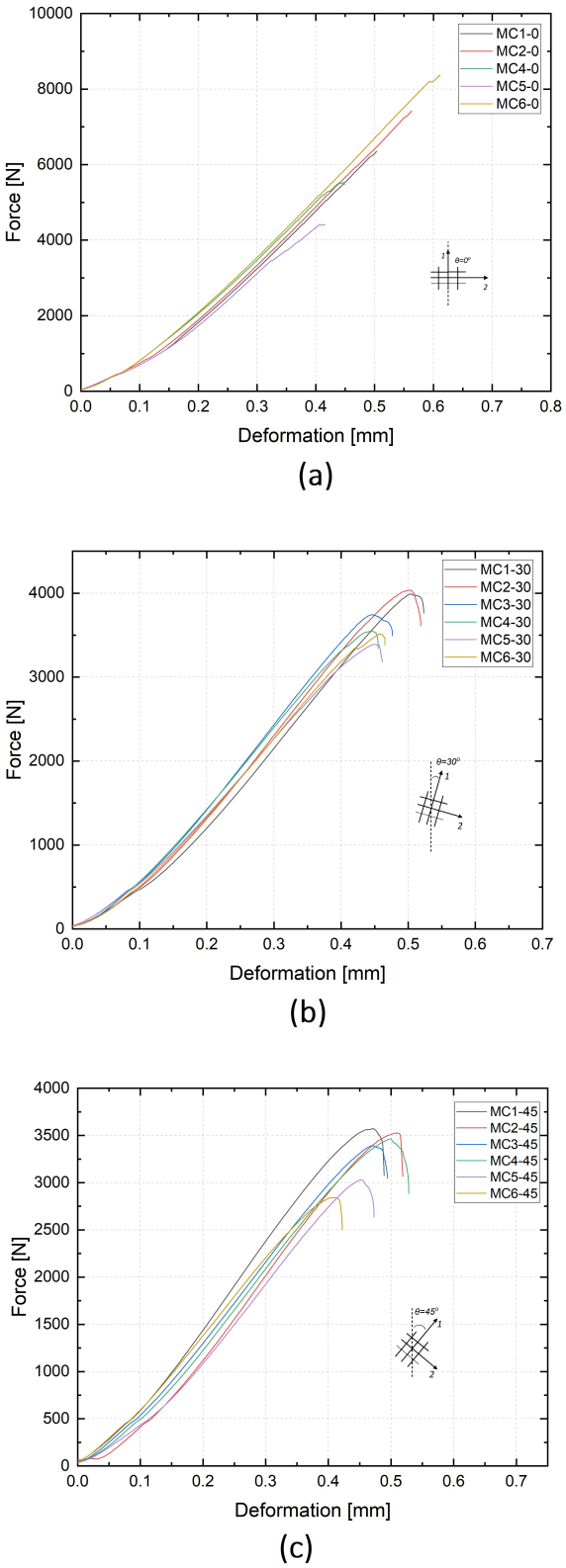

Figure C.8: Force-displacement curves of C/C-SiC loaded with monotonic compression load for (a) $\theta = 0^o$, (b) $\theta = 30^o$ and (c) $\theta = 45^o$.

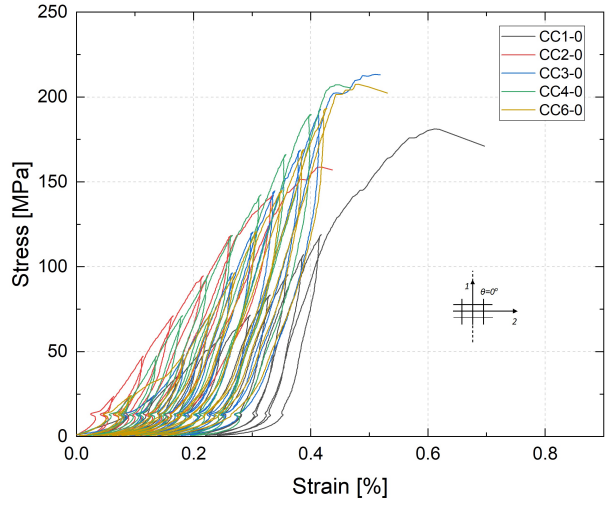

(a)

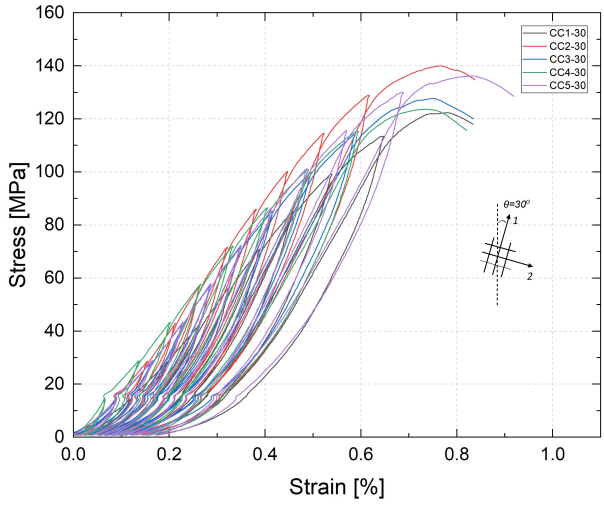

(b)

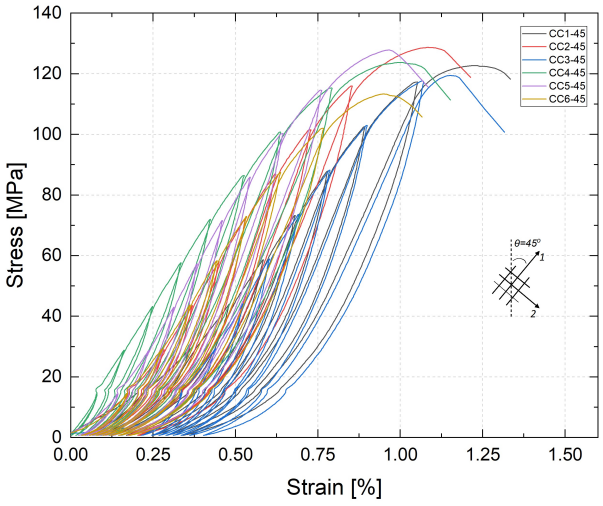

(c)

Figure C.9: Stress-strain curves of C/C-SiC loaded with cyclic compression load for (a) $\theta = 0^o$, (b) $\theta = 30^o$ and (c) $\theta = 45^o$.

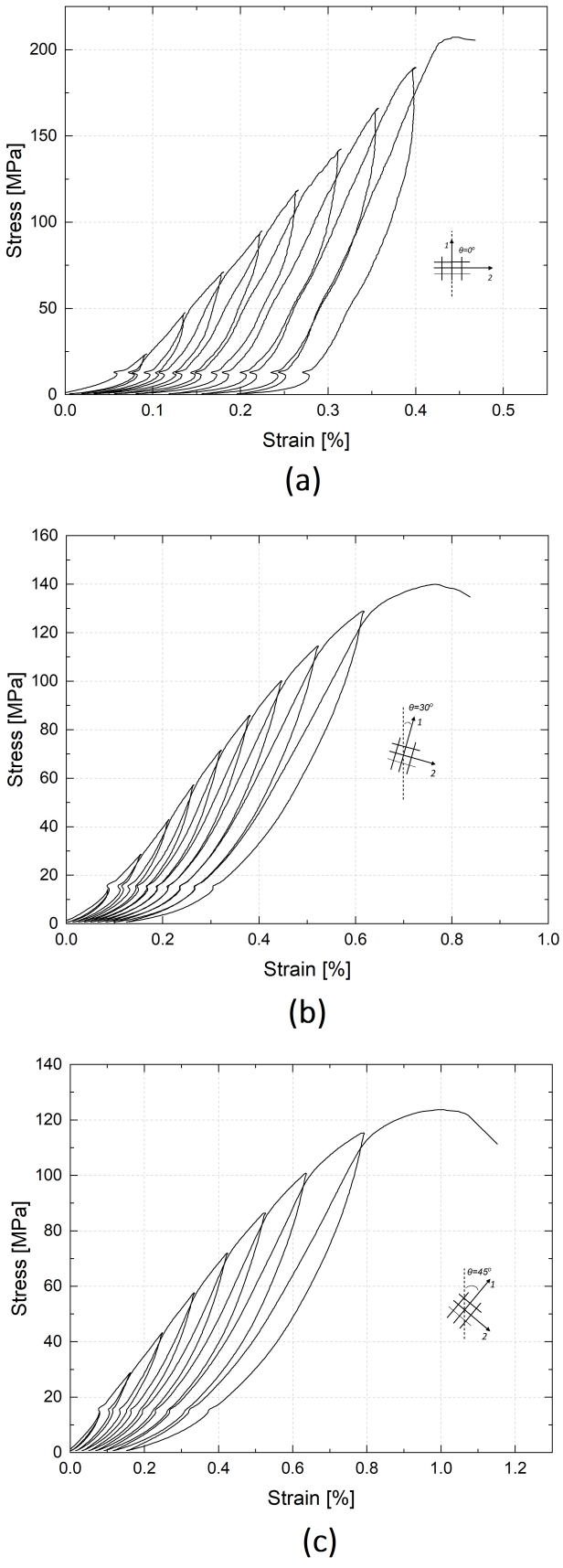

Figure C.10: A typical stress-strain curve of C/C-SiC loaded with cyclic compression load for (a) $\theta = 0^o$, (b) $\theta = 30^o$ and (c) $\theta = 45^o$.

C.4. EDS

The energy-dispersive X-Ray spectroscopy (EDS) measurements of the material are presented below. Three different measurements in the areas of interest were conducted. The results are presented in the Figure below.

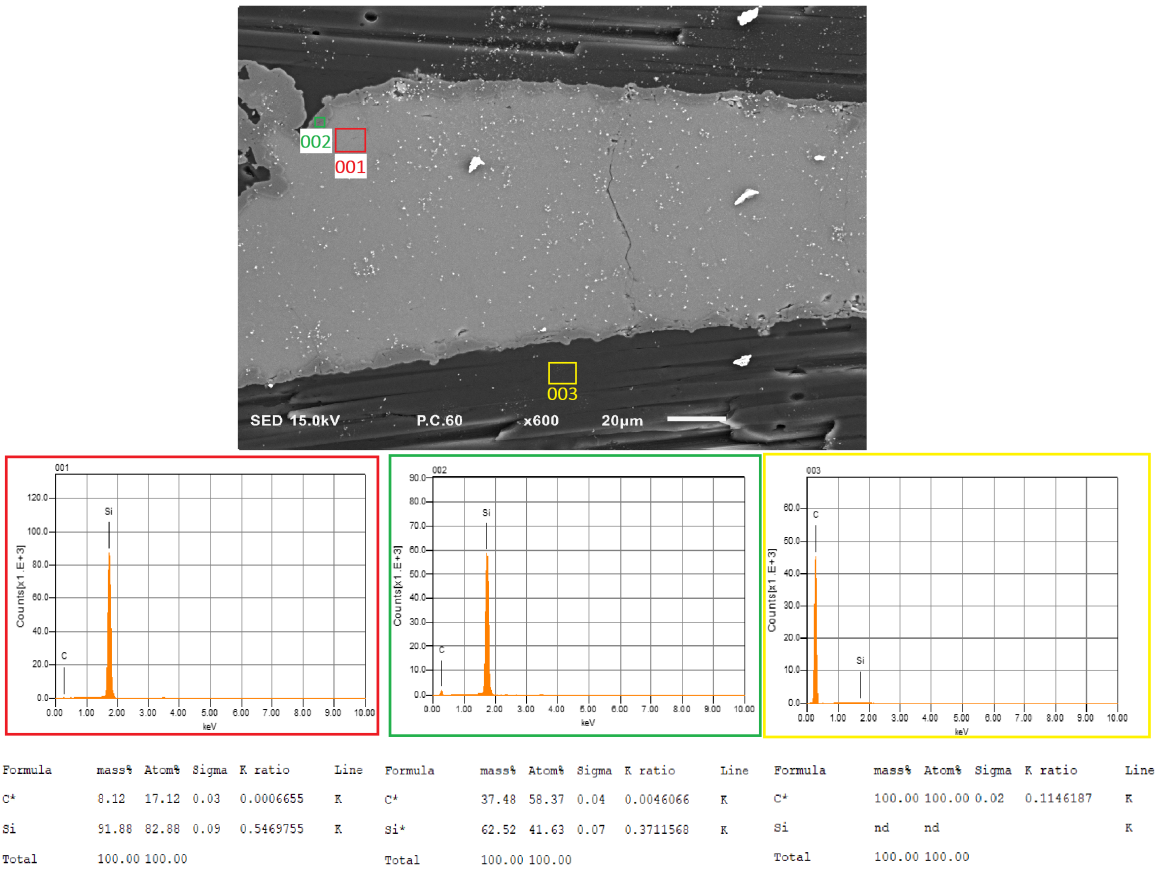

Formula	mass%	Atom%	Sigma	K ratio	Line
C*	8.12	17.12	0.03	0.0006655	K
Si	91.88	82.88	0.09	0.5469755	K
Total	100.00	100.00			

Formula	mass%	Atom%	Sigma	K ratio	Line
C*	37.48	58.37	0.04	0.0046066	K
Si*	62.52	41.63	0.07	0.3711568	K
Total	100.00	100.00			

Formula	mass%	Atom%	Sigma	K ratio	Line
C*	100.00	100.00	0.02	0.1146187	K
Si	nd	nd			K
Total	100.00	100.00			

Figure C.11: EDS measurement at three different locations.

C.5. Digital image correlation

A trial experiment was performed with the use of the DIC system. Initial skepticism about the ability of the DIC system to capture the small deformation that CMCs exhibit was proven wrong. The DIC system can be used in this type of material.

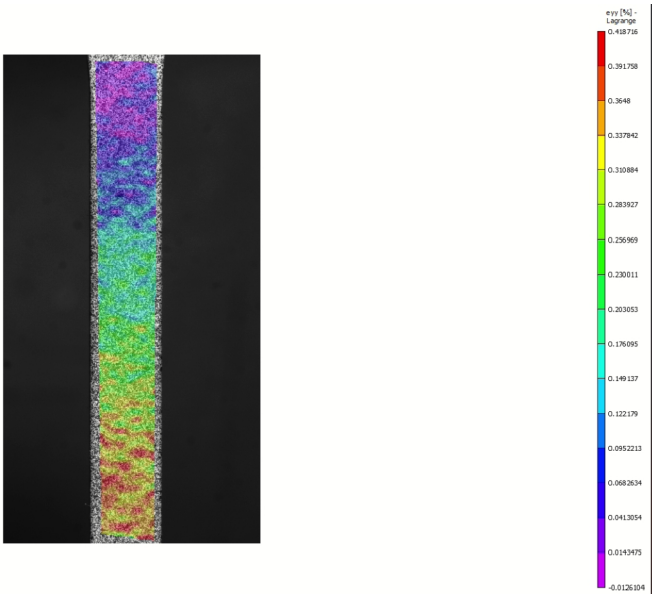

Figure C.12: Strain measurement of a tensile specimen with $\theta = 0^o$ loaded in tension with the use of the DIC technique.

D

Bayesian optimization

Further information about Bayesian optimization and parameter optimization is presented here. Regarding the selection of λ, the two loss terms of the objective function (5.1) are presented in Figures D.1 and D.2.

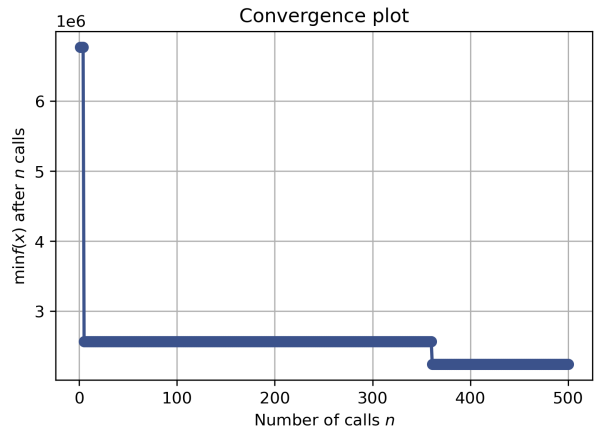

Figure D.1: Convergence plot for the first loss term (monotonic test data).

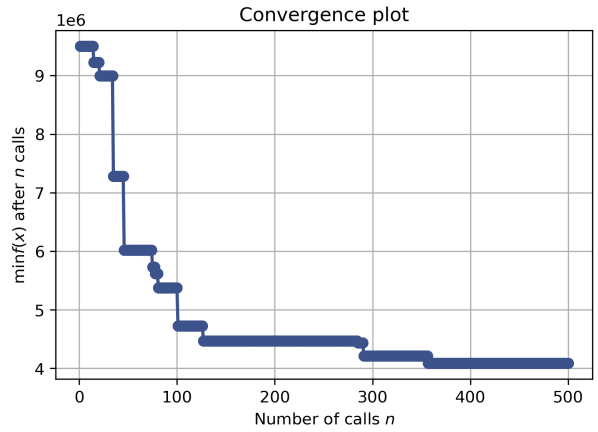

Figure D.2: Convergence plot for the second loss term (cyclic test data).

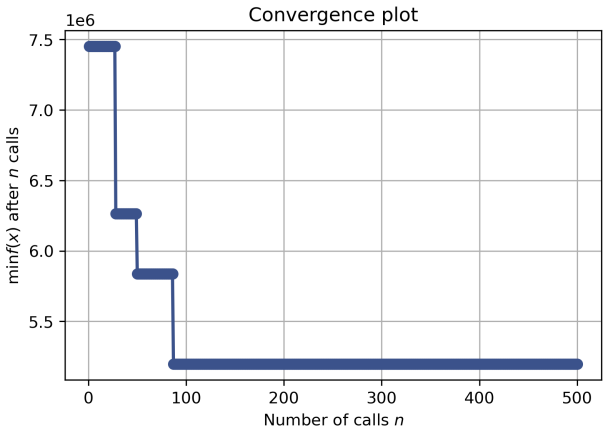

Figure D.3: Convergence plot of the objective function.

Bibliography

[1] P. J. Armstrong, C. Frederick, et al. *A mathematical representation of the multiaxial Bauschinger effect*, volume 731. Berkeley Nuclear Laboratories Berkeley, CA, 1966.

[2] M. Arruda, L. Almeida-Fernandes, L. Castro, and J. Correia. Tsai–wu based orthotropic damage model. *Composites Part C: Open Access*, 4:100122, 2021.

[3] B. Audoin and S. BASTE. On internal variables in anisotropic damage. *European Journal of Mechanics, A/Solids*, 10(6):587–606, 1991.

[4] N. P. Bansal. *Handbook of ceramic composites*, volume 165. Springer, 2005.

[5] R. Böhm, M. Gude, and W. Hufenbach. A phenomenologically based damage model for textile composites with crimped reinforcement. *Composites Science and Technology*, 70 (1):81–87, 2010.

[6] J. Böhler and J. Raclin. Failure criteria for glass-fiber reinforced composites under confining pressure. *Journal of structural mechanics*, 13(3-4):371–393, 1985.

[7] V. Calard and J. Lamon. Failure of fiber bundles. *Composites science and technology*, 64(5):701–710, 2004.

[8] L. A. Carlsson, D. F. Adams, and R. B. Pipes. *Experimental characterization of advanced composite materials*. CRC press, 2014.

[9] A. Chen and F. Matthews. A review of multiaxial/biaxial loading tests for composite materials. *Composites*, 24(5):395–406, 1993.

[10] W.-F. Chen and D.-J. Han. *Plasticity for structural engineers*. J. Ross Publishing, 2007.

[11] X. Chen, X. Sun, P. Chen, B. Wang, J. Gu, W. Wang, Y. Chai, and Y. Zhao. Rationalized improvement of tsai–wu failure criterion considering different failure modes of composite materials. *Composite Structures*, 256:113120, 2021.

[12] R. G. Cuntze. Strength failure conditions of the various structural materials: is there some common basis existing? *Structural Durability & Health Monitoring*, 3(2):87, 2007.

[13] W. Curtin. Multiple matrix cracking in brittle matrix composites. *Acta metallurgica et materialia*, 41(5):1369–1377, 1993.

[14] I. M. Daniel and O. Ishai. *Engineering mechanics of composite materials*, volume 1994. Oxford university press New York, 2006.

[15] S. J. DeTeresa and G. J. Larsen. *Derived interaction parameters for the Tsai-Wu tensor polynomial theory of strength for composite materials*, volume 35777. 2001.

[16] S. J. DeTeresa and G. J. Larsen. Reduction in the number of independent parameters for the tsai—wu tensor polynomial theory of strength for composite materials. *Journal of composite materials*, 37(19):1769–1785, 2003.

[17] P. K. Dileep. Experimental characterization and numerical simulation of c/c-sic grid core sandwich structures. 2017.

[18] M. Flaschel, S. Kumar, and L. De Lorenzis. Discovering plasticity models without stress data. *npj Computational Materials*, 8(1):1–10, 2022.

[19] S. Flauder, I. Bombarda, R. D'Ambrosio, N. Langhof, A. Lazzeri, W. Krenkel, and S. Schafföner. Size effect of carbon fiber-reinforced silicon carbide composites (c/c-sic): Part 2-tensile testing with alignment device. *Journal of the European Ceramic Society*, 42(4):1227–1237, 2022.

[20] I. Gol'denblat and V. Kopnov. Strength of glass-reinforced plastics in the complex stress state. *Polymer Mechanics*, 1(2):54–59, 1965.

[21] M. Gupta, H. Singh, A. N. Khan, P. Mahajan, R. D. Prabhakaran, and R. Alagirusamy. An improved orthotropic elasto-plastic damage model for plain woven composites. *Thin-Walled Structures*, 162:107598, 2021.

[22] L. Hahn, F. Ansorge, and A. Bruckner-Foit. Damage and failure behaviour of a woven c/sic material. *Journal of materials science*, 32(20):5467–5475, 1997.

[23] J. He, D. Abueidda, R. A. Al-Rub, S. Koric, and I. Jasiuk. A deep learning energy-based method for classical elastoplasticity. *arXiv preprint arXiv:2209.06467*, 2022.

[24] M.-Y. He and J. W. Hutchinson. Kinking of a crack out of an interface. 56(2):270–278, 1989.

[25] B. Heidenreich. Melt infiltration process. *Ceramic Matrix Composites*, pages 113–139, 2008.

[26] B. Heidenreich. Processing and properties of advanced ceramics and composites iv. 2012.

[27] S. Hofmann. Effect of interlaminar defects on the mechanical behaviour of carbon fibre reinforced silicon carbide. 2014.

[28] S. Hofmann, B. Öztürk, D. Koch, and H. Voggenreiter. Experimental and numerical evaluation of bending and tensile behaviour of carbon-fibre reinforced sic. *Composites Part A: Applied Science and Manufacturing*, 43(11):1877–1885, 2012.

[29] W. Hufenbach, R. Böhm, A. Langkamp, L. Kroll, and T. Ritschel. Ultrasonic evaluation of anisotropic damage in multiaxially textile-reinforced thermoplastic composites made from hybrid yarns. *Mechanics of Composite Materials*, 42(2):151–162, 2006.

[30] N. Jain and D. Koch. Prediction of failure in ceramic matrix composites using damage-based failure criterion. *Journal of Composites Science*, 4(4):183, 2020.

[31] D. Koch, K. Tushtev, and G. Grathwohl. Ceramic fiber composites: experimental analysis and modeling of mechanical properties. *Composites Science and Technology*, 68(5): 1165–1172, 2008.

[32] W. Krenkel. Cost-effective processing of cmc composites by melt infiltration (lsi-process). *Ceramic Engineering and Science Proceedings*, pages 443–454, 2009.

[33] J. Lamon. Approach to microstructure–behavior relationships for ceramic matrix composites reinforced by continuous fibers. *Ceramic Matrix Composites: Materials, Modeling and Technology*, pages 520–547, 2014.

[34] J. Li, G. Jiao, B. Wang, C. Yang, and G. Wang. Damage characteristics and constitutive modeling of the 2d c/sic composite: Part i–experiment and analysis. *Chinese Journal of Aeronautics*, 27(6):1586–1597, 2014.

[35] J. Li, G. Jiao, B. Wang, L. Li, and C. Yang. Damage characteristics and constitutive modeling of the 2d c/sic composite: Part ii–material model and numerical implementation. *Chinese Journal of Aeronautics*, 28(1):314–326, 2015.

[36] L. Li. Micromechanical modeling of time-dependent crack opening behavior in sic/sic composites. 85970:V001T02A002, 2022.

[37] S. Li, E. Sitnikova, Y. Liang, and A.-S. Kaddour. The tsai-wu failure criterion rationalized in the context of ud composites. *Composites Part A: Applied Science and Manufacturing*, 102:207–217, 2017.

[38] Z. Li, Y. Long, Y. Li, J.-w. Li, X. Xiong, and P. Xiao. Microstructure and properties of needle punching chopped carbon fiber reinforced carbon and silicon carbide dual matrix composite. *Ceramics International*, 42(8):9527–9537, 2016.

[39] N. Lissart and J. Lamon. Damage and failure in ceramic matrix minicomposites: experimental study and model. *Acta Materialia*, 45(3):1025–1044, 1997.

[40] L. Longbiao. Micromechanical modeling for tensile behaviour of carbon fiber- reinforced ceramic- matrix composites. *Applied Composite Materials*, 22(6):773–790, 2015.

[41] A. Matzenmiller, J. Lubliner, and R. L. Taylor. A constitutive model for anisotropic damage in fiber-composites. *Mechanics of materials*, 20(2):125–152, 1995.

[42] G. A. Maugin, R. Drouot, and F. Sidoroff. *Continuum Thermomechanics: The Art and Science of Modelling Material Behaviour*, volume 76. Springer Science & Business Media, 2006.

[43] R. J. Nuismer. Predicting the performance and failure of multidirectional polymeric matrix composite laminates: a combined micro-macro approach. 1980.

[44] S. Ogihara and K. L. Reifsnider. Characterization of nonlinear behavior in woven composite laminates. *Applied composite materials*, 9(4):249–263, 2002.

[45] M. Patel, K. Saurabh, V. B. Prasad, and J. Subrahmanyam. High-temperature c/c–sic composite by liquid silicon infiltration: a literature review. *Bulletin of Materials Science*, 35(1):63–73, 2012.

[46] F. Raischel, F. Kun, and H. J. Herrmann. *Fiber bundle models for composite materials*. 2006.

[47] R. Sandhu. A survey of failure theories of isotropic and anisotropic materials. 1972.

[48] U. Santhosh and J. Ahmad. A model for estimating nonlinear deformation and damage in ceramic matrix composites. *Journal of composite materials*, 47(10):1257–1272, 2013.

[49] U. Santhosh, J. Ahmad, G. Ojard, R. Miller, and Y. Gowayed. Deformation and damage modeling of ceramic matrix composites under multiaxial stresses. *Composites Part B: Engineering*, 90:97–106, 2016.

[50] J. Schulte-Fischedick, A. Zern, J. Mayer, M. Rühle, M. Frieß, W. Krenkel, and R. Kochendörfer. The morphology of silicon carbide in c/c–sic composites. *Materials Science and Engineering: A*, 332(1-2):146–152, 2002.

[51] Y. Shi, N. Jain, R. Jemmali, S. Hofmann, D. Koch, and S. Hackemann. Prediction of elastic properties for a wound oxide ceramic matrix composite material. *International Journal of Applied Ceramic Technology*, 12:E99–E110, 2015.

[52] Y. Shi, N. Jain, and D. Koch. Investigation and modeling of tensile failure properties of wound ceramic matrix composites. *Composites Part A: Applied Science and Manufacturing*, 114:316–326, 2018.

[53] Y. Shi, Y. L. Xiu, and D. Koch. *Investigation of statistical distribution of C/C-SiC composite's mechanical properties*, volume 809. 2019.

[54] Y. Shi, F. Kessel, M. Friess, N. Jain, and K. Tushtev. Characterization and modeling of tensile properties of continuous fiber reinforced c/c-sic composite at high temperatures. *Journal of the European Ceramic Society*, 41(5):3061–3071, 2021.

[55] Y. Shi, S. Li, E. Sitnikova, D. Cepli, and D. Koch. Experimental evaluation and theoretical prediction of elastic properties and failure of c/c-sic composite. *International Journal of Applied Ceramic Technology*, 19(1):7–21, 2022.

[56] J. C. Simo and T. J. Hughes. *Computational inelasticity*, volume 7. Springer Science & Business Media, 2006.

[57] P. Soden, M. Hinton, and A. Kaddour. A comparison of the predictive capabilities of current failure theories for composite laminates. *Composites science and technology*, 58 (7):1225–1254, 1998.

[58] C. Sun. Strength analysis of unidirectional composites and laminates. 2000.

[59] C. Sun and J. Chen. A simple flow rule for characterizing nonlinear behavior of fiber composites. *Journal of Composite materials*, 23(10):1009–1020, 1989.

[60] S. W. Tsai. A survey of macroscopic failure criteria for composite materials. *Journal of Reinforced Plastics and Composites*, 3(1):40–62, 1984.

[61] S. W. Tsai and E. M. Wu. A general theory of strength for anisotropic materials. *Journal of composite materials*, 5(1):58–80, 1971.

[62] K. Tushtev, J. Horvath, D. Koch, and G. Grathwohl. Deformation and failure modeling of fiber reinforced ceramics with porous matrix. *Advanced Engineering Materials*, 6(8): 664–669, 2004.

[63] K. C. Warren, R. A. Lopez-Anido, S. S. Vel, and H. H. Bayraktar. Progressive failure analysis of three-dimensional woven carbon composites in single-bolt, double-shear bearing. *Composites Part B: Engineering*, 84:266–276, 2016.

[64] J. Xie, G. Fang, Z. Chen, and J. Liang. Modeling of nonlinear mechanical behavior for 3d needled c/c-sic composites under tensile load. *Applied Composite Materials*, 23(4): 783–797, 2016.

[65] J. Xie, G. Fang, Z. Chen, and J. Liang. An anisotropic elastoplastic damage constitutive model for 3d needled c/c-sic composites. *Composite Structures*, 176:164–177, 2017.

[66] Z. Zhang, Y. Liu, L. Li, and D. Fang. Modeling tensile damage and fracture behavior of fiber-reinforced ceramic-matrix minicomposites. *Materials*, 13(19):4313, 2020.